CHARACTERISATION OF STEP COVERAGE BY PULSED-PRESSURE METALORGANIC CHEMICAL VAPOUR DEPOSITION: TITANIUM DIOXIDE THIN FILMS ON 3-D MICRO- AND NANO-SCALE STRUCTURES

A thesis submitted in partial fulfilment of the

requirements for the Degree

of

Doctor of Philosophy in Mechanical Engineering

at the

University of Canterbury

Christchurch, New Zealand

by

Vilailuck Siriwongrungson

2010

For my Family

My Inspiration and Dedication

TABLE OF CONTENTS

LIST OF FIGURES

LIST OF TABLES

ACKNOWLEDGEMENTS

It is a great distance for me to come from Bangkok, Thailand to study here at the University of Canterbury, Christchurch, New Zealand. Nevertheless, during my study towards a PhD degree, I have experienced the warm hospitality, invaluable suggestions and joyful activities of many people and hereby express my appreciation to them in this acknowledgement.

Firstly, I would like to thank my supervisor and co-supervisor, Associate Professor Susan P. Krumdieck and Associate Professor Maan M. Alkaisi, for useful discussions, advice, support (both financial and educational) and understanding. Thank you to the University of Canterbury and Advanced Energy and Material Systems Laboratory, New Zealand for financial support during my PhD study. I gratefully acknowledge the assistance of Ron Tinker from the Mechanical Engineering Department, Adrienne Tinker and Colin Krumdieck in ensuring my experiences of New Zealand culture were memorable.

I would like to express my appreciation to the following people for their invaluable discussions, advice, support, encouragement and inspiration:

Dr Khairudin Mohamed from the Electrical and Computer Engineering Department for structured sample preparation and meaningful suggestions; Associate Professor Milo Kral, Paul Southward, Adam Latham, Julian Phillips, Julian Murphy, Kevin Stobbs, Eric Cox, Paul Wells, Scott Amies, Graeme Harris and Mike Flaws, Mechanical Engineering Department technicians, for

their SEM help and technical support; Associate Professor Richard M. Hartshorn, Chemistry Department for suggestions in precursor preparation; Helen Devereux and Gary Turner for AFM support and safety and instruction in the Nanofabrication Laboratory, the Electrical and Computer Engineering Department; Dr Joon (Scott) Choi from the Physics and Astronomy Department for Raman and UV-VIS Spectroscopy analysis and data interpretation; Professor Susan James, visitor to the Mechanical Engineering Department from the School of Biomedical Engineering, Colorado State University, USA for suggestions; Dr Nicholas Long and Martin Ryan, Industrial Research Limited for the XRD analysis; Dr Maxim Lebedev and Asdis Kristinsdottir, former colleagues of the Advanced Energy and Material Systems Laboratory for suggestions and advice.

The following people gave me support and encouragement as well as entertainment. I really appreciate everything they have done.

Advanced Energy and Material Systems Laboratory members: Dr Hadley M. Cave, Dr Shannon Page, Mohammed Sohel, Muaviyath Mohamed, Mik Dale, Samuel Gyamfi, and Stacey Rendall. International friends: Tessie Lambourne, Dr Wei Hau Ho, Stefanie Spiering, Dr Dimitri Hariskos, Dr Katja Wiese, Katja Dansk, Dr Pedro D'Jesus Montilva, Ladawan and Yoshinori Tanaka, and Ye Zhang. Thai friends: Adiphol Dilokphimol, Dr Dichapong Pongpattrachai, Associate Professor Kloyjai Cheuyglintase, Dr Siramas Komonjinda, Sunita Chamyuang, Kochakorn and Jimmy Sears, Kanitta Intaroonwong, Chatchai

Thnarudee, Niphon and Sureeporn Punnopakorn, Siriporn Atireklarp, Sidipa Pongpraewpan, Wijuck Krisnakri and Sukit Kanjina.

Thank you also to the monks, especially Phramaha Manit, Phramaha Sayan, Phramaha Phat, and Phramaha Phan; and Thai seniors at the Thai temple, Wat Buddha Samakkee, Marshland, Christchurch, for giving me a chance to give something back to New Zealand as a volunteer Thai teacher, for being my mental support and teaching me about Buddhist morality, meditation and offering.

Last, but certainly not least, I am truly grateful to my family and cousins – Mom Kanitha, Dad Veerachai, sisters Krisana and Ratree, buddies Tee and Muay and Montira Watcharasukarn for endless love, understanding and encouragement. Discussion from my aunts and uncles, Patarawan Dechaboonako, Pon and Ian Foster, and Susan and Richard Tai are acknowledged.

Because so many people have assisted me along the way, I may have left some names out. If so, I am sorry, but please know that I really do appreciate each one of you.

ABSTRACT

An examination of the possibility of applying pulse pressure metalorganic chemical vapour deposition (PP-MOCVD) to conformal coating and an investigation of PP-MOCVD processing parameters were undertaken using the deposition of thin, conformal titanium dioxide (TiO_2) on 3-D featured and non-featured substrates. The characterisation of the conformality and wettability analysis of thin TiO_2 was carried out using titanium tetraisopropoxide (TTIP) dissolved in toluene as a precursor and featured silicon (Si) and silicon nitride (Si_3N_4) as substrates. The features on the substrates were in micro- and nano-scale with the aspect ratio up to 2:1.

The processing parameters investigated were temperatures between 400 and 600°C, reactor base pressures from 50 to 200 Pa, injection volumes between 50 and 250 µl, precursor concentrations in the range of 0.15 to 0.50 mol% and pulsing times from 10 to 20 sec. The surface morphology and thickness were examined using a scanning electron microscope (SEM). The composition of the films was qualitatively identified by energy dispersive X-ray spectroscopy (EDS). X-ray diffraction (XRD) and Raman spectroscopy were used to analyse the phase and grain size. The surface roughness and grain size were evaluated using atomic force microscopy (AFM). The optical properties were characterised using UV-VIS light spectroscopy. The anti-sticking characteristic was examined by wettability analysis, measuring the contact angle of the film with water. The research examined the relationships between processing

parameters and growth rate, conformality, surface roughness, grain size, phase and water contact angle.

A new measurement for thin film conformality was derived based on a statistical analysis of a large number of film thickness measurements on a fracture surface over the lithographed features. The best conformality of 0.95 was obtained for micro-scale features at the lowest temperature in the range of investigation, 400°C, with pulse exposure characterised by a base pressure of 100 Pa, TTIP concentration of 0.50 mol%, injection volume of 50 µl and pulsing time of 10 sec. Conformality for micro-scale features was in the range of 0.82 to 0.97 over a wide range of deposition temperatures. Conformality was as low as 0.45 over nano-scale structures at the higher exposure rate. The conformality decreased as the temperature and precursor concentration increased. The precursor injection volume was found to have minor influences on conformality.

The growth rate increased as the temperature increased and reached the maximum at the deposition temperature of 450°C with the precursor concentration of 0.50 mol% and injection volume of 100 µl. The base pressure and relaxation time had slight influences on the growth rate over the deposition temperature range of 400 to 500°C. The growth rate was increased as the precursor concentration and precursor injection volume increased.

The deposited TiO_2 films exhibited columnar growth and anatase phase. The base pressure and pulsing time had no obvious effects on grain size and surface

roughness. The grain size decreased as the deposition temperature increased. The surface roughness increased as the deposition temperature increased.

Contact angles of over 100° were found with conformality of over 0.80. The variation in contact angle was related to the surface morphology of the deposited films. The contact angle increased as the grain size decreased. High wettability was found for films in the mid-range of pulse exposure, in this study at pulse exposure of 53, or at high deposition temperature, in this case at 600°C. The as-deposited TiO_2 thin films were hydrophobic depending on the surface morphology, surface roughness and grain size.

GLOSSARY AND ABBREVIATIONS

$\int_0^t n(t)dt$	Number of molecules evacuated at time t from the beginning of the pulse cycle
β	Full width at half maximum value of a peak in a diffraction pattern
Δ	Thickness of the viscous boundary layer
ΔH	Reaction enthalpy at constant pressure
δ	Film thickness
$\bar{\delta}$	Average film thickness
ϕ	Molecular flux of vapour to the substrate surface
γ_{FS}	Free energy between deposited film and substrate
γ_{FV}	Free energy between deposited film and vapour interface
γ_{SV}	Free energy between substrate and vapour interface
λ	The wavelength of the incident X-ray; the vapour molecular mean free path or mean free path of the gas molecules
μ	Viscosity
θ	Angle between incident beam and the particular crystal planes under consideration; angle of diffraction
ρ	The deposited film density; mass density
τ	Evacuation or pump down time constant
A	A constant in Arrhenius equation; absorbance
AES	Auger Electron Spectroscopy
AFM	Atomic Force Microscopy
ALD	Atomic Layer Deposition
APCVD	Atmospheric Pressure Chemical Vapour Deposition
C	A constant; conformality; conductance
C_{sys}	Conductance of an exhaust system
C_{mo}	Metalorganic precursor concentration in mol%
CaH_2	Calcium hydride
CAS	Chemical Abstracts Service

CCD	Charge-Coupled Device
CCS	Closed-Coupled Showerhead
CHF_3	Trifluoromethane
CVD	Chemical Vapour Deposition
d	Density of precursor or solvent as subscripted in $g \cdot ml^{-1}$; effective molecular diameter
D	Crystallite size
DNQ	Diazonaphthoquinone
DRAM	Dynamic Random Access Memories
DSMC	Direct Simulation Monte Carlo
E_a	Adsorption energy of an isolated adatom on the substrate
$E_{a'}$	Adsorption energy of an adatom on a monolayer of the condensate
EDS	Energy Dispersive X-Ray Spectroscopy
EBL	Electron Beam Lithography
FESEM	Field Emission Scanning Electron Microscopy
FWHM	Full Width at Half Maximum
FM	Frank-van der Merwe
HBTs	Hetero Bipolar Transistors
HMW	High Molecular Weight
HPLC	High Performance Liquid Chromatography
ID	Internal Diameter
InP	Indium phosphide
IPA	Isopropanol or isopropyl alcohol
IR	Infrared
J	Total molecular flux per unit area; adatom arrival rate
J^*	Dimensionless total molecular flux per unit area
J_{max}	Highest total molecular flux or highest adatom arrival rate
K	Equilibrium constant
Kn	Knudsen number
L	Characteristic length such as initial trench mouth width and reactor diameter

LabVIEW	Laboratory Virtual Instrumentation Engineering Workbench
LEDs	Light Emitting Diodes
LMW	Low Molecular Weight
LPCVD	Low Pressure Chemical Vapour Deposition
LPMOCVD	Low Pressure Metalorganic Chemical Vapour Deposition
M	Precursor molecular mass; thickness sampling point used to represent the overall film thickness
M	Metal atom
MAVPE	Metal-Alkyl Vapour Phase Epitaxy
MIBK	Methyl isobutyl ketone
MO	Metalorganic
MOCVD	Metalorganic Chemical Vapour Deposition
MOVPE	Metalorganic Vapour Phase Epitaxy
MSDS	Material Safety Data Sheet
Mw	Molecular weight of precursor or solvent as subscripted in $g \cdot mol^{-1}$
n	Refractive index
n_L	Molecular leak rate
n_i	Number of molecules from the injection tube
n_{min}	Number of molecules at the reactor minimum pressure
$n(t)$	Number of molecules in the reaction chamber at any time
N_A	Avogadro's number
$Ni(CO)_4$	Nickel tetracarbonyl
NiCr	Nichrome
NIL	Nanoimprint lithography
OD	Outside Diameter
OMCVD	Organometallic Chemical Vapour Deposition
OMVPE	Organometallic Vapour Phase Epitaxy
P	Pressure
$P(t)$	Reactor pressure as a function of processing time
P^*	Reactor exposure
P_{max}	Maximum pressure

P_{min}	Minimum pressure
P_S	Supply pressure
P_u	Ultimate pressure or the lowest pressure the reactor system can reach
P_{vap}	Precursor vapour pressure
PDF	Powder Diffraction File
PE	Pulse Exposure
PEEK	Polyetheretherketone or polyketones or polyaryletherketones
PMMA	Polymethylmethacrylate
PP	Polypropylene
PP-CVD	Pulsed Pressure Chemical Vapour Deposition
PP-MOCVD	Pulsed Pressure Metalorganic Chemical Vapour Deposition
PSD	Position Sensitive Detector
PTFE	Polytetrafluoroethylene or polytetrafluoroethene
PVD	Physical Vapour Deposition
PZT	Lead Zirconate Titanate
Q	Throughput of a steady flow rate
R	Ideal gas constant
R_a	Mean roughness
RBS	Rutherford backscattering
RDR	Rotating Disk Reactor
Re	Reynolds number
RF	Radio Frequency
RIE	Reactive Ion Etching
RMS	Root Mean Square
RPCVD	Reduced Pressure Chemical Vapour Deposition
S	Evacuation speed or exhaust speed
S_P	Vacuum pump speed or volumetric pump speed at the nominal operating pressure
SEM	Scanning Electron Microscopy
SF_6	Sulphur hexafluoride
Si	Silicon

SiC	Silicon carbide
SIMS	Secondary Ion Mass Spectrometry
Si_3N_4	Silicon nitride
SK	Stranski-Krastanov
SMA	SubMiniature version A
STI	Shallow Trench Isolation
t	The time in a pulse cycle of PP-MOCVD
t_i	Injection time
t_p	Pulse cycle time
T	Deposition temperature
T_{min}	The lowest substrate temperature
TEM	Transmission Electron Microscopy
TEOS	Tetraethoxysiland or tetraethylorthosilicate
$TiCl_3$	Titanium trichloride
$TiCl_4$	Titanium tetrachloride
TiI_4	Titanium tetraiodide
TiN	Titanium nitride
TiO_2	Titanium dioxide
TTIP	Titanium tetraisopropoxide
u	Fluid flow density
UHVCVD	Ultra High Vacuum Chemical Vapour Deposition
v	Volume of precursor or solvent as subscripted in ml
V_R	Reactor volume
V_S	Injection volume
VW	Volmer-Weber
W	Tungsten
WCl_6	Tungsten chloride
x	The distance from inlet in the flow direction
XPS	X-ray Photoelectron Spectroscopy
XRD	X-Ray Diffractometry
YBCO	Yttrium Barium Copper Oxide
YSZ	Yttrium Stabilised Zirconia

ZDV	Zero Dead Volume
ZrO_2	Zirconium oxide

LIST OF PUBLICATIONS AND PRESENTATIONS

Journal Publications:

Krumdieck, S., Siriwongrungson, V., Reyngoud, B., Barnett, A., Bio-integration Ceramics on 3D Specimens by Pulsed-Pressure Metal-Organic CVD, *Chemical Vapor Deposition*, **16** (2010).

Siriwongrungson, V., Alkaisi, M., Krumdieck, S., Step coverage of thin titania films on patterned silicon substrate by pulsed-pressure MOCVD, *Surface and Coatings Technology,* **201**, 22-23 (2007) 8944-8949.

Conference Papers:

Siriwongrungson, V., Krumdieck, S. P., Alkaisi, M. M., Pulsed-Pressure MOCVD Processing Investigation for TiO_2 Films on Si_3N_4 Substrate from TTIP, *ECS Transaction*, **25**, 8 (2009) 987-990.

Conference Abstracts and Posters:

Siriwongrungson, V., Krumdieck, S., Alkaisi, M., Pulsed-Pressure MOCVD Processing Investigation for TiO_2 Films on Si_3N_4 Substrate from TTIP, Seventeenth European Conference on Chemical Vapor Deposition, EuroCVD-17, 4-10 October 2009, Vienna, Austria.

Siriwongrungson, V., Alkaisi, M., Krumdieck, S., Step coverage of thin titania films on patterned silicon substrate by pulsed-pressure MOCVD, Sixteenth European Conference on Chemical Vapor Deposition, EuroCVD-16, 16-21 September 2007, Den Haag (Scheveningen), the Netherlands.

Siriwongrungson, V., Alkaisi, M., Krumdieck, S., Conformal titania thin films on silicon nitride by pulsed pressure metalorganic chemical vapor deposition using titanium tetrakis-isopropoxide, Third International Conference of Advanced Materials and Nanotechnology (AMN 3), 11-16 February 2007, Wellington, New Zealand.

CHAPTER 1

INTRODUCTION

Conformal step coverage is an important goal in the deposition of thin films for many industrial usages including microelectronics (Barbato et al., 2007), integrated circuit technologies (Yun and Rhee, 1997) and nanoimprint lithography (NIL) (Alkaisi et al., 2001). In most cases, the sizes of the trenches and vias tend to decrease but the aspect ratios tend to increase (IslamRaja et al., 1991). Titania, or titanium dioxide (TiO_2), is known for its very low surface affinity for organic molecules, high refractive index, high thermal stability and chemical inertness. It is now widely used in many applications including solar cells (O'Regan and Grätzel, 1991), gas sensors (Lin et al., 1997), decoration (Diebold, 2003), self-cleaning glass (Ogawa et al., 2008; Stamate and Lazar, 2007), corrosion protective coating (Tuan et al., 2000), thermal barrier (Krumdieck and Raj, 2001a), anti-reflective coating (Dislich and Hinz, 1982), dynamic random access memories (DRAM) (Kaliwoh et al., 2002) and decontamination and purification of environmental pollutants (Bessergenev et al., 2002; Kaliwoh et al., 2002; Tuan et al., 2000). Pulsed-pressure metalorganic chemical vapour deposition (PP-MOCVD) has a pulsing action with the potential to provide good uniformity in films with even step coverage. Previous studies have demonstrated relatively fast growth rates for a low pressure process, and low contamination in the films as the products are actively removed (Krumdieck and Raj, 2001a). PP-MOCVD requires a low substrate temperature to initiate a chemical reaction, and it uses and produces

low toxicity reactants and products. In addition, it produces high quality thick and thin films with good uniformity, good growth rate and high conversion efficiency (Cave et al., 2008).

The aims of this project are to examine the possibility of applying PP-MOCVD to conformal coating and to investigate the influence of PP-MOCVD processing parameters on film characteristics. Film characteristics were investigated as it affects film properties, hence the performance of the film. The film characteristics and properties considered in this study included conformality, growth rate, surface morphology, surface roughness, grain size, phase, energy band gap and contact angle. The processing control variables were substrate temperature, precursor concentration, precursor injection volume (e.g. total flow rate), reactor base pressure and pulsing or relaxation time. Relaxation time refers to additional time over the pulse period in excess of the nominal 10-sec pulse cycle. A non-dimensional parameter called pulse exposure (Krumdieck et al., 2007b) was applied as a processing control variable. Pulse exposure is the molecular arrival rate over the pulse and is a non-dimensional parameter involving precursor concentration, injection volume, reactor base pressure and relaxation time.

An understanding of the effects of varying the processing parameters on the deposited material properties and conformality was gained through systematic investigation varying each parameter individually then looking for general trends. Titanium tetraisopropoxide (TTIP) dissolved in toluene was used as the liquid precursor. Substrates were silicon (Si) and silicon nitride (Si_3N_4) with

3-D micro- and nano-scale features. The results from this study represent a processing map for the deposition of TiO_2 by PP-MOCVD on Si or Si_3N_4 substrates with micro- and nano-scale features.

This thesis is organised into seven chapters as outlined below.

Chapter 1 The introduction chapter gives the motivation for carrying out this research, the research aims and objectives and an outline of the thesis. The introduction includes the applications of the deposited TiO_2 by PP-MOCVD and the characteristics of PP-MOCVD. The processing parameters, film characteristics and properties are stated to give an indication of the way the research objectives are to be reached.

Chapter 2 The background chapter provides an overview of the research into the deposition techniques, the deposition mechanism, the conformality, the chemistry of the precursor and the material science of thin films. A review of conventional deposition techniques is presented. These include chemical vapour deposition (CVD), metalorganic chemical vapour deposition (MOCVD), pulsed-pressure metalorganic chemical vapour deposition (PP-MOCVD), atomic layer deposition (ALD) and physical vapour deposition (PVD). The material science review of thin film focuses on TiO_2, which is the ceramic material in this study. In the conformality review, growth mechanisms in

producing a conformal coating and research into step coverage of substrates with 3-D patterns are provided.

Chapter 3 The methods chapter describes the experimental work, material analysis, calculations of precursor concentration, deposited film properties, growth parameters and experimental design. The experimental work includes the preparation of the substrates and precursor and apparatus. The deposited film properties are growth rate, grain size, conformality, refractive index and band gap. The growth parameters include pulse exposure and total molecular flux.

Chapter 4 The results and discussion chapter includes the results and discussion of deposited TiO_2 thin film growth rate, surface morphology, phase, surface roughness, grain size and conformality as a function of processing parameters and pulse exposure. The measurement accuracy is described in the last section of this chapter.

Chapter 5 The wettability analysis chapter shows the results and discussion of the water contact angle of the featured Si_3N_4 substrates that were coated with TiO_2 by PP-MOCVD.

Chapter 6 The conclusion chapter summarises the thesis and includes the research objective, experiments and the results and discussion of findings.

Chapter 7 The last chapter, future work, describes potential possibilities of future work.

CHAPTER 2

BACKGROUND

This chapter reviews the principles and research related to the investigation of conformality of TiO_2 thin film by PP-MOCVD. A review of conventional deposition techniques and PP-MOCVD are described. The background chapter is outlined as below.

2.1. Deposition Techniques

2.2. Deposition Mechanism, Thermodynamics and Mass Transport of CVD and PP-MOCVD

2.3. Microstructures and Nucleation of Thin Films

2.4. Review and Literature Review of Conformality of Thin Films

2.5. Precursor Chemistry

2.6. Titanium Dioxide Thin Films

2.7. Substrate Materials

2.1. Deposition Techniques

There are a number of deposition methods that can deposit TiO_2 thin film as well as other thin film materials. Each deposition technique has its advantages, disadvantages and produces various film properties and characteristics with a range of growth rates, costs and efficiencies. The characteristics of thin films include surface morphology and conformality. This section describes the overview of deposition techniques related to pulsed-pressure metalorganic chemical vapour deposition (PP-MOCVD). These include chemical vapour

deposition (CVD) and metalorganic chemical vapour deposition (MOCVD). Atomic layer deposition (ALD) will be mentioned because it is a kind of a pulsed process and known for its ability to deposit good step coverage thin film coating on 3-D features. The fundamental vapour deposition process, physical vapour deposition (PVD), is also described in this section.

2.1.1. Review of Chemical Vapour Deposition

Chemical vapour deposition (CVD) is the deposition process in which the chemicals are in a vapour phase and undergo chemical reactions to form solid films on substrates. The CVD process can be categorised based on operating pressure, reaction initiation source and precursor.

Atmospheric pressure CVD (APCVD) operates at atmospheric pressure. An exhaust system for a gas cleanup is required. Reduced pressure CVD (RPCVD) uses the operating pressure in the range of 133 to 1.33×10^4 Pa and low pressure CVD (LPCVD) has the operating pressure between 1.33 and 1.33×10^{-3} Pa. The operating pressure is less than 10^{-5} Pa for ultra high vacuum CVD (UHVCVD) (Duminica et al., 2007; Ohring, 2002).

There are several reaction initiation sources for CVD. If the reactions are started by heat or thermal energy, the process is called thermal CVD. If higher frequency radiation or electrical energy such as UV or plasma is the initiation source, the CVD is called as photo-assisted CVD or plasma-enhanced CVD, respectively. When metalorganic or organometallic compounds are used as the

precursors, the CVD is called metalorganic CVD (MOCVD) (Jones and Hitchman, 2009).

CVD is an established process with a long historical background. The terms CVD and PVD were introduced in 1960 to differentiate chemical from physical arrival processes (Pierson, 2006). A patent by de Lodyguine in 1893 could be one of the early uses of CVD in industry (Choy, 2003). This patent is about the deposition of tungsten (W) onto carbon lamp filaments using the reduction of tungsten chloride (WCl_6) and hydrogen (H_2) as a carrier gas. The study related to W from WCl_6 and H_2 was first investigated by Wölher and Uslar in 1855 (Wöhler and Uslar, 1855). During the following fifty years, several famous processes were developed. These included the carbonyl cycle known as the Mond process for the deposition of pure nickel from nickel tetracarbonyl ($Ni(CO)_4$) and nickel ore refinement, the iodide decomposition or the de Boer–Van Arkel process for multicrystalline semiconductor materials preparation, and the magnesium-reduction reaction or the Kroll process for metallic titanium production (Pierson, 2006). Reviews by Powell, Oxley and Blocher in 1966 covered the published literature to the mid-1960s (Powell et al., 1966; Powell, 1966; Sherwood and Blocher, 1965). A series of handbooks and technical volumes have been published, the most recent being *Chemical Vapour Deposition: Precursors, Processes and Applications* edited by Jones and Hitchman (Jones and Hitchman, 2009).

Generally, there are three subsystems in a CVD system: the precursor supply system; the reactor system; the exhaust system or effluent gas handling (Choy,

2003). Figure 2-1 gives a simple system schematic of a conventional CVD system.

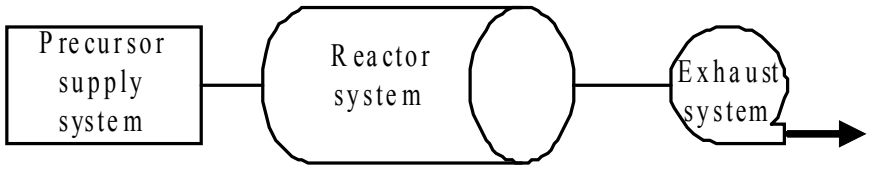

Figure 2-1: An example of the component of a conventional CVD system.

Conventional CVD Precursor Supply System

The precursor supply system generates and delivers a metered quantity of vapour phase reactants to the reactor system. The design of the precursor supply system depends on the phase of the reactants – whether they are solid, liquid or gas. In the case of solid, the rate of sublimation will depend on the surface area and contact time of the precursor and carrier gas. A bubbler is normally required to vaporise the liquid phase reactants. The vaporised liquid precursors are transported into the reactor using a carrier gas. The carrier gas could be a reactive gas such as hydrogen or an inert gas like argon. The delivery of the liquid reactants depends on the liquid precursor temperature, pressure over the liquid precursor and the carrier gas flow rate. When the vapour pressure of the liquid precursors is known, the pressure over the liquid precursor is normally controlled using the volume and flow rate of the carrier gas.

Conventional CVD Reactor System

Following the precursor system is the reactor system or the reaction chamber. The reactor system requires a heating system with a temperature control to raise the temperature of the substrate for the chemical reactions to occur. It is normally equipped with a load lock and a substrate holder. The load lock is used to convey and replace the substrate into the reaction chamber.

CVD reactor systems can be divided into two types depending on the heating zone approach: hot wall and cold wall reactor systems. The temperature in a hot wall reactor system is controlled using at least two separate controllable heating zones. The heater is normally an isothermal furnace. The main drawback of the hot wall reactor is parasitic reactor wall deposition. The reaction occurs not only on the substrate but also on the reactor wall and all other heated surfaces as well. This poses a risk of remaining precursors and by-products being incorporated with the reactor wall or other heated components resulting in cleanliness and maintenance problems and low deposition efficiency (Choy, 2003).

For the cold wall reactor system, only the substrate is heated while the reaction chamber may be cooled by a continuous air flow or cooling water. Therefore, the thermally activated reactions take place on the heated substrate. Comparing the heat transfer of the hot wall and the cold wall reactor, the heat transfer from the heaters to the substrates is mainly by radiation for the hot wall reactor and by conduction for the cold wall reactor (Choy, 2003). Two examples of a hot wall reactor and a cold wall reactor are shown in Figure 2-2.

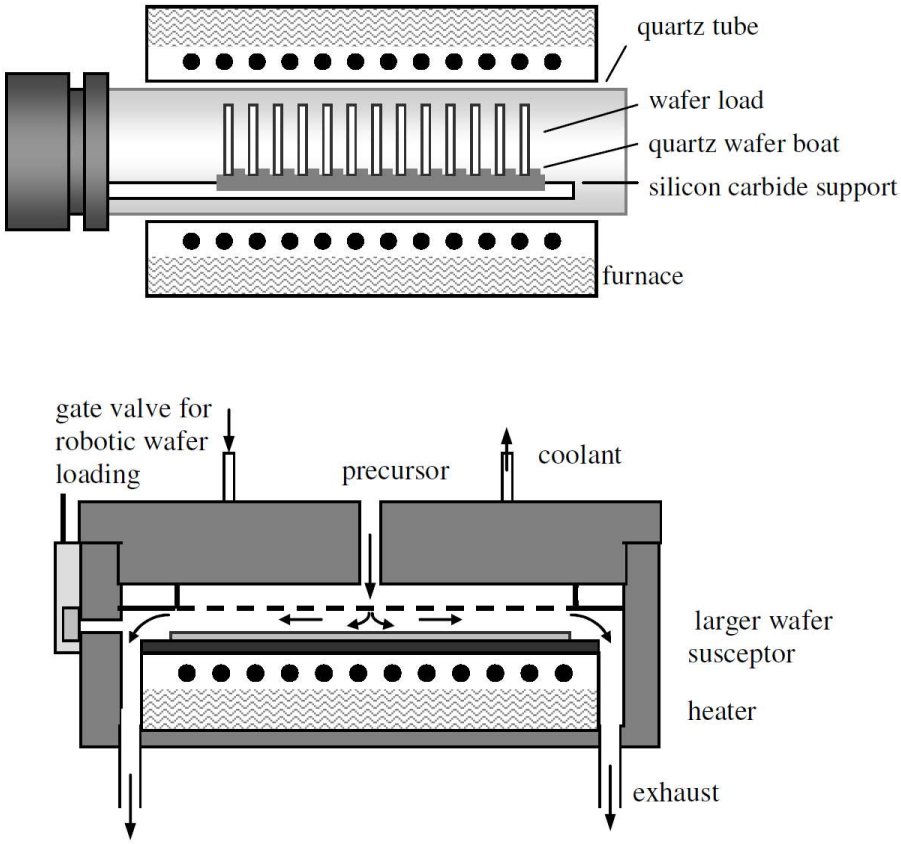

Figure 2-2: A horizontal hot wall reactor (top) and a single wafer cold wall showerhead reactor (bottom) (Jones and Hitchman, 2009). Reproduced by permission of the Royal Society of Chemistry (RSC).

Conventional CVD Exhaust System

The last system in a CVD system is the exhaust system. The exhaust system evacuates the reaction products, by-products, remaining reactants and depleted gas, which are generally reactive and toxic. The design of the exhaust system and the type of vacuum pump depend on the pressure requirement and the properties of the reactants, products and by-products.

Vacuum pumps can be divided into two types according to the means of gas removal. One of them is known as the entrapment or gas trapping pump and the other is called the gas-transfer or positive displacement pump or kinetic

vacuum pump. Generally, when comparing gas-transfer pumps and gas-trapping pumps, the gas-transfer pumps have a higher pump speed while gas-trapping pumps have the ability to produce lower pressure. Each type of pump is suitable for different applications, generally depending on the two pump specifications. One is the ultimate pressure (P_u) and the other is the nominal pumping speed (S_p). The ultimate pressure is the measurement of the pressure between a vacuum gauge and a blanked or dead end fitting at the pump inlet when the pump is well warmed up. The pumping speed from the manufacturer is the highest value measured under ideal conditions (Jones and Hitchman, 2009).

The entrapment pump condenses or chemisorbs the gas molecules from the low pressure and traps the molecules until the end of the deposition process. The entrapment pumps include an adsorption pump, a sputter-ion pump and a cryogenic pump.

The gas-transfer pump physically removes gas molecules from low pressure to ambient after one or more stages of compression. The positive displacement pumps are, for example, the rotary piston pump, the rotary vane pump and the roots pump. The kinetic vacuum pumps include the oil diffusion pump, the turbomolecular pump, the molecular drag pump and the newer turbo-drag hybrid pump.

The rotary piston pump and the rotary vane pump are two basic displacement pumps that are commonly used to obtain reduced pressure. The rotary piston pump has a pump speed of 30 to 1,500 $m^3 \cdot h^{-1}$ or 8.3 to 416 $l \cdot s^{-1}$ while the rotary

pump has a pump speed of 10 to 200 $m^3 \cdot h^{-1}$ or 2.8 to 55 $l \cdot s^{-1}$ (Ohring, 2002). The roots pump is used in sputtering and LPCVD because it can stand continuous large gas volumes along with maintaining the pressure at about one torr. The roots pump has a very high pumping speed but it requires a forepump such as a rotary mechanical pump. Its maximum achievable pressure at pumping speeds of up to several thousand $l \cdot s^{-1}$ is in the range of 0.13 to 2.6×10^3 Pa with the ultimate pressure of 1.3×10^{-3} Pa.

The oil diffusion pump is one of the gas-transfer pumps, but it is categorised as a kinetic vacuum pump instead of a displacement pump. It also requires a forepump to maintain pressure. It is normally used when the fluid is in molecular flow regime with the pressure range of 1.3×10^{-3} to 0.13 Pa and pumping speed between a few $l \cdot s^{-1}$ to over 20,000 $l \cdot s^{-1}$. The principal problem with this kind of pump is the back streaming of oil into the chamber; hence it is normally used in non-electronic application coating where a little contamination is acceptable.

There are several methods to solve the back streaming problem. One example is using a cold trap together with a refrigerated trap and optically dense baffles. An oil free pump such as a turbomolecular pump could be another option as no baffles are required. The drawback to this turbomolecular pump is the cost which is quite high. Nevertheless, it is increasing in use in thin film deposition and it has an ultimate pressure below 1.3×10^{-8} Pa with a pumping speed of 10^3 $l \cdot s^{-1}$.

Further reading can be found, for example, in the vacuum technology chapters of many CVD handbooks and vacuum science handbooks (Jones and Hitchman, 2009; Ohring, 2002; Roth, 1990; Smith, 1995).

The conventional steady flow CVD can deposit film at a cheaper cost compared to PVD when a high growth rate is required. In general, CVD requires a high substrate temperature to initiate chemical reactions. It has low conversion efficiency and low uniformity in certain cases such as high aspect ratio and high sticking coefficient substrates (Krumdieck, 1999). In addition, the reactants used in CVD are toxic. Nevertheless, CVD can be adapted and developed to be used with various deposition processes and less toxic reactants to deposit an adherent high density pure film with good step coverage on 3-D substrates. Those deposition processes include PP-MOCVD that can provide good uniformity films and high conversion efficiency and MOCVD in which the reactants and products are less toxic (Babelon et al., 1998; Krumdieck, 1999; Nami et al., 1997).

CVD has been applied to produce films of ceramic and metallic materials for many applications. These applications include electronics and optoelectronics, semiconductors, conductors, insulators, thermal barriers, diffusion barriers, mechanical cutting tools and inorganic fibres (Choy, 2003).

2.1.2. Review of Conventional Metalorganic Chemical Vapour Deposition

Metalorganic chemical vapour deposition (MOCVD) is the deposition method by which vapour phase metalorganic precursors undergo chemical reaction and form a condensed phase on a substrate. The deposition methods that use metalorganic as precursors include metal-alkyl vapour phase epitaxy (MAVPE), metalorganic vapour phase epitaxy (MOVPE), organometallic chemical vapour deposition (OMCVD) and organometallic vapour phase epitaxy (OMVPE).

MOCVD was patented in 1967 by Ruehwein with Monsanto, USA. The following year, a similar process was published in 1968 for epitaxial growth by Manasevit who is widely acknowledged as the inventor of MOCVD in an open-tube reactor chamber (Manasevit and Simptons, 1969; Manasevit, 1972; Manasevit, 1981). The development of III-V epitaxial films began from the early-1960s to late-1970s. The pace of development occurred in 1978 after the quantum-well semiconductor lasers operating in continuous wave at room temperature were reported by Dupuis and Holonyak (Holonyak Jr. et al., 1978). Until now, the MOCVD is the principal production and research method in compound semiconductor materials and devices.

A metalorganic precursor generally means a compound that is composed of an element, such as metal, and an organic carbon group, such as alkoxide, alkyl, alicyclic, aryl, etc. This kind of precursor is less toxic than the precursor generally used in conventional CVD and highly volatile at moderate to low

temperatures (Tuan et al., 2000; Werbowy et al., 2004). In the production of III-V semiconductors, the mixture of metalorganic group III and hydride group V precursors is normally used together with nitrogen or hydrogen or the mixture of these two as the carrier gas. The purity of precursors and carrier gases needs to be high enough for the production of high-quality materials from MOCVD.

Conventional MOCVD Precursor Supply System

The precursor supply system transports and controls the precursor mole fraction and carrier gases into the reaction system. For MOCVD, the precursor supply system normally consists of 316L stainless steel tubing, manifolds, purifiers, filters, automatic and manual valves, pressure controllers and mass flow controllers (Jones and Hitchman, 2009). The precursor supply system design depends strongly on the phase of the precursors. Most of the metalorganic precursors are in solid or liquid phase and have high vapour pressure near room temperature and atmospheric pressure. The principle of condensed phase vapour pressure equilibrium is applied to transport the metalorganic precursor into the reactor. A gas, such as nitrogen or hydrogen, is introduced into the condensed metalorganic phase to capture the precursor vapour and transport the precursors into the reactor. In the case of the hydride precursors, group V, most of them are gas phase at room temperature, hence liquefied in a high pressurised cylinder. The liquefied hydride precursor is normally transferred directly into the reactor without any additional carrier gas. Generally, the liquefied gas has high purity but it will pass through a pressure

regulator and a purifier for oxygen and water vapour removal before entering the reaction chamber (Jones and Hitchman, 2009).

Conventional MOCVD Reactor System

The MOCVD reactor system comprises a reaction chamber, which is made of quartz or stainless steel, gas flow injector, susceptor and heating device. The susceptor, made from graphite or coated with silicon carbide (SiC), is located in a place where the growth of the films is uniform in the reaction chamber. The susceptor is usually rotatable to assist in thickness and alloy composition uniformity. The heating device in a MOCVD reactor system could use resistive heating, radio frequency (RF) induction heating or infrared (IR) radiation heating. The susceptor should be matched with the heating device, for example, an electrically conducting susceptor for RF induction heating and an optically absorbing susceptor for IR radiation heating. MOCVD has two types of reactor systems based on the primary flow direction of the input gases, which is influenced by the gas flow injector and the exhaust system.

One of the MOCVD reactor systems is the horizontal reactor. In a horizontal reactor, the gas phase precursor flow is parallel to the substrate surface. The susceptor is able to tilt and rotate in order to compensate for the depletion effect of the gas phase precursors. The other MOCVD reactor system is the vertical reactor. The gas phase precursor flow is normal to the substrate surface in a vertical reactor. A rotatable susceptor in a vertical reactor is normally used for multi-wafer deposition purpose.

Commercial MOCVD reactor systems have been designed, improved and optimised for the production of materials with uniformity and efficiency. Those reactor system designs include a closed-coupled showerhead (CCS) reaction chamber from Thomas Swan Scientific Equipment Ltd, a horizontal rotary susceptor system from Taiyo Nippon Sanso, a planetary reactor system by Phillips and Aixtron and a rotating disk reactor (RDR) system known as TurboDisc from Emcore Corporation (Jones and Hitchman, 2009).

Conventional MOCVD Exhaust System

The last component in a conventional MOCVD system is the exhaust system. The principal functions of the exhaust system are to remove the remaining reactants and by-products from the reaction chamber and to maintain the pressure inside the reactor during the deposition process. The selection of a vacuum pump depends on the operating pressure and reactants and by-products as mentioned in section 2.1.1.

MOCVD can deposit films with homogeneity (Leistner et al., 2002) and good conformality (Schumacher et al., 2003). It provides higher throughput with precise stoichiometry and uniformity control and less defect density compared to PVD (Schumacher et al., 2003). In addition, the processing allows uniform growth of high quality films including low deposition temperature, selective-area deposition and controllable film stress and grain size (Nami et al., 1997a). MOCVD is a preferred deposition method for epitaxial growth because it offers high throughput at low cost compared to other deposition methods (Korgel and Hicks, 1995). The metalorganic precursors are more expensive compared to

halides, hydrides and halohydrides. They are very reactive; hence purification is difficult and expensive to achieve (Choy, 2003). The handling of a metalorganic precursor requires an accurate pressure to control the evaporation and delivery of liquid precursors.

MOCVD can produce amorphous, polycrystalline and single crystal and has been applied to deposit films in many applications. The applications of MOCVD include large volume production of semiconductor devices such as hetero bipolar transistors (HBTs) and light emitting diodes (LEDs), high purity epitaxial films of insulators, conductive and resistive layers for solar devices and electronics and optoelectronic devices such as far-IR photodetectors and phodiodes (Krishna, 2002; Nami et al., 1997; Schumacher et al., 2003.

2.1.3. Review of Pulsed-Pressure MOCVD Technology Development

Pulsed-pressure metalorganic chemical vapour deposition (PP-MOCVD) is the deposition method used in this study. The principle of PP-MOCVD is that a metered quantity of liquid metalorganic precursor solution is introduced into a low pressure or vacuum reaction chamber at a discrete timed interval through an ultrasonic atomiser. The pressure inside the reactor is increased after the flash evaporation of the liquid precursors and decreased back to the base pressure before the next injection of the liquid precursors. The pressure inside the PP-MOCVD reactor of each pulse cycle is illustrated in Figure 2-3.

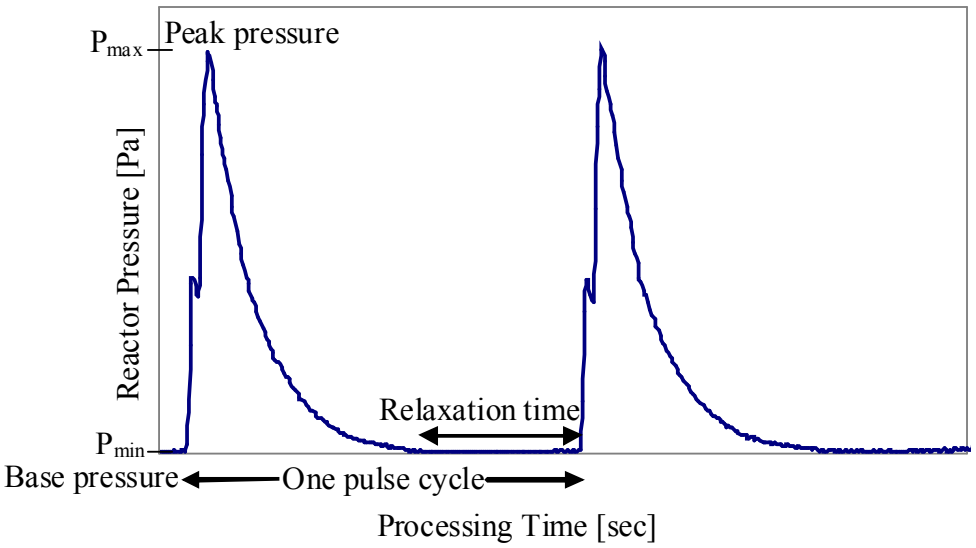

Figure 2-3: The pressure profile inside the PP-MOCVD reactor as a function of processing time.

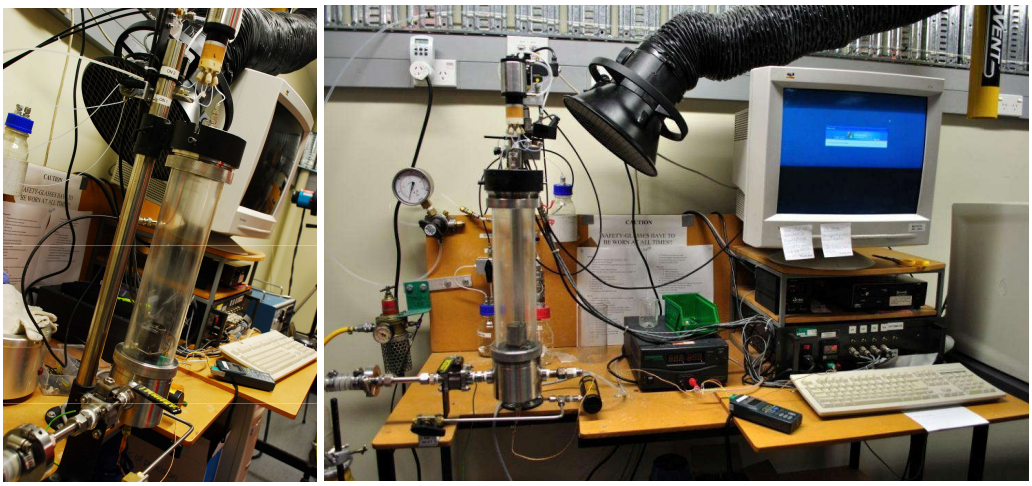

Figure 2-4: PP-MOCVD reactor and its set up at the AEMS Lab, University of Canterbury, New Zealand, which was used in this study.

Pulsed-pressure chemical vapour deposition (PP-CVD) was first developed at Cornell University, Ithaca, New York, USA in 1993 and proposed by Versteeg et al. in 1994. In 2000, Krumdieck built PP-CVD reactors based on the patent at the Advanced Energy and Material System Laboratory (AEMS Lab), University of Canterbury, Christchurch, New Zealand as shown in Figure 2-4.

The patent is currently licensed by Sonotek Coporation in Milton, New York, USA (Versteeg et al., 1995).

Certain investigations relating to PP-MOCVD are from Krumdieck et al. The studies that relate to the deposition of TiO_2 include the conversion efficiency and growth rate of TiO_2 from TTIP over the temperature range of 400 to 700°C (Krumdieck and Raj, 1999), the effect of temperature on growth rate, morphology, coverage and carbon contamination of TiO_2 films (Krumdieck and Raj, 2001b), experimental characterisation and modelling of TiO_2 growth rate (Krumdieck, 2001) and conversion efficiency, crystallographic orientation and microstructure using TTIP as a precursor (Krumdieck and Raj, 2001a). Investigations into yttria stabilised zirconia (YSZ) (Werbowy et al.) include, for example: investigation of rate-controlling mechanisms, conversion efficiency and morphology by unique precursor delivery and control by a low pressure pulsed-CVD process of TiO_2 and YSZ films at temperatures between 400 and 650°C (Krumdieck et al., 2001); deposition of solid zirconium oxide (ZrO_2) and YSZ films from metalorganic precursors (Krumdieck et al., 2002); YSZ layers on solid oxide fuel cell electrodes (Krumdieck et al., 2003). Modelling works of Krumdieck et al. include the PP-CVD model development for high precursor conversion (Cave et al., 2008) and the expansion transport regime of PP-CVD using a gaseous precursor (Krumdieck et al., 2007a). Lastly, there is a study on the deposition of hydroxyapatite coating to stimulate bone growth (Hartshorn et al., 2007).

Nakamura has applied a similar principle of pulsed pressure to fill a void free shallow trench isolation (STI) silicon using tetraethoxysilane (TEOS) oxide from TEOS gas at a temperature of 700°C (Nakamura, 2001). Funakubo et al. compared the crystal structure and electrical properties of tetragonal and rhombohedral lead zirconate titanate ($Pb(Zr,Ti)O_3$ or PZT) films deposited by pulsed-MOCVD at temperatures of 395 to 580°C (Funakubo et al., 2002). The pulsed-MOCVD used by Funnakubo et al. in this study means the pulsing of precursors in 10 sec at 5-sec intervals. This implies that the pressure is constant. This group also studied the deposition of epitaxial-grade polycrystalline PZT films at a temperature of 415°C using pulsed-MOCVD (Aratani et al., 2001).

The PP-MOCVD system comprises a precursor supply system, reactor system, exhaust handling system and control system. Figure 2-5 is the schematic diagram of the liquid injection PP-MOCVD setup.

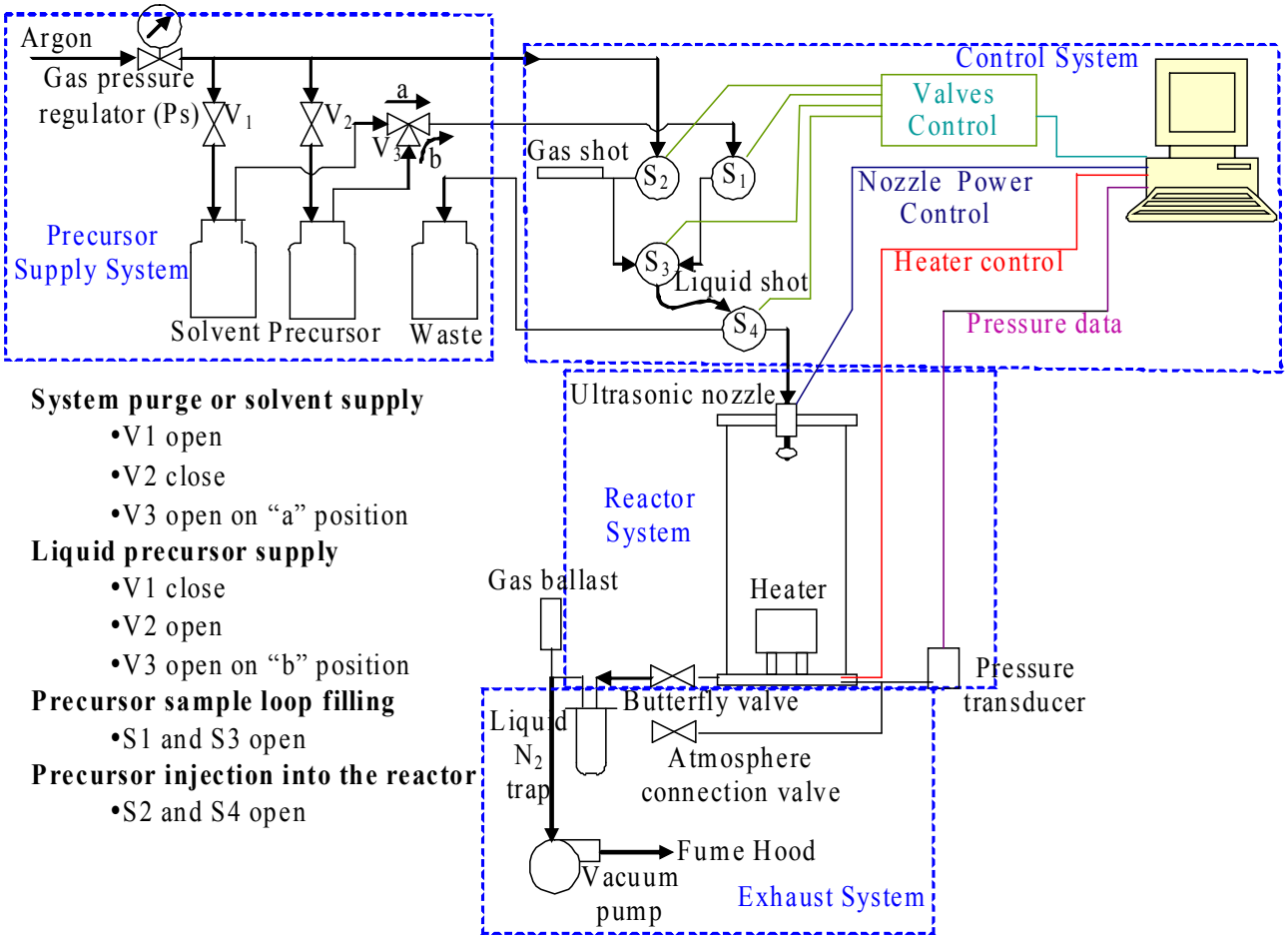

Figure 2-5: Liquid injection PP-MOCVD apparatus setup.

Precursor Supply System of PP-MOCVD

The reactant supply system in PP-MOCVD supplies a metered quantity of liquid precursor into the reaction chamber in the discrete time interval or pulse. The push gas source, in this case argon, is at supply pressure (P_s). P_s is controlled by a gas pressure regulator used to adjust the pressure from a highly pressurised gas source to an acceptable level of pressure for each application. Two two-way valves allow the argon gas to flow into the solvent or precursor pressurised glass bottles. The glass bottle should stand the pressure in the range operated; otherwise a plastic or metal bottle is acceptable. As illustrated in Figure 2-6, the precursor or solvent will flow to the reactor throu gh a three-way valve which controls the precursor and solvent supply to a sample loop. Solenoid valves regulate an air actuator which controls a sample injector. The sample injector is a two-position sample injector used to fill the sample loop and then introduce the precursor into the reactor with an inert push gas shot to clear the lines. The precursor supply system is in the sample loop filling when the sample injector is in position one. It is during the precursor transfer to the reactor when the sample injector is in position two as shown in Figure 2-7. The air actuator is operated using compressed air from an air compressor. For the PP-MOCVD used in this study, a quick connect was installed to help protect the precursor from air exposure when the precursor bottle is installed in the system as the precursor used is sensitive to moisture. A mobile phase filter was connected to the tubing inside the precursor bottle in order to protect the system from particles according to the pore size of the filter.

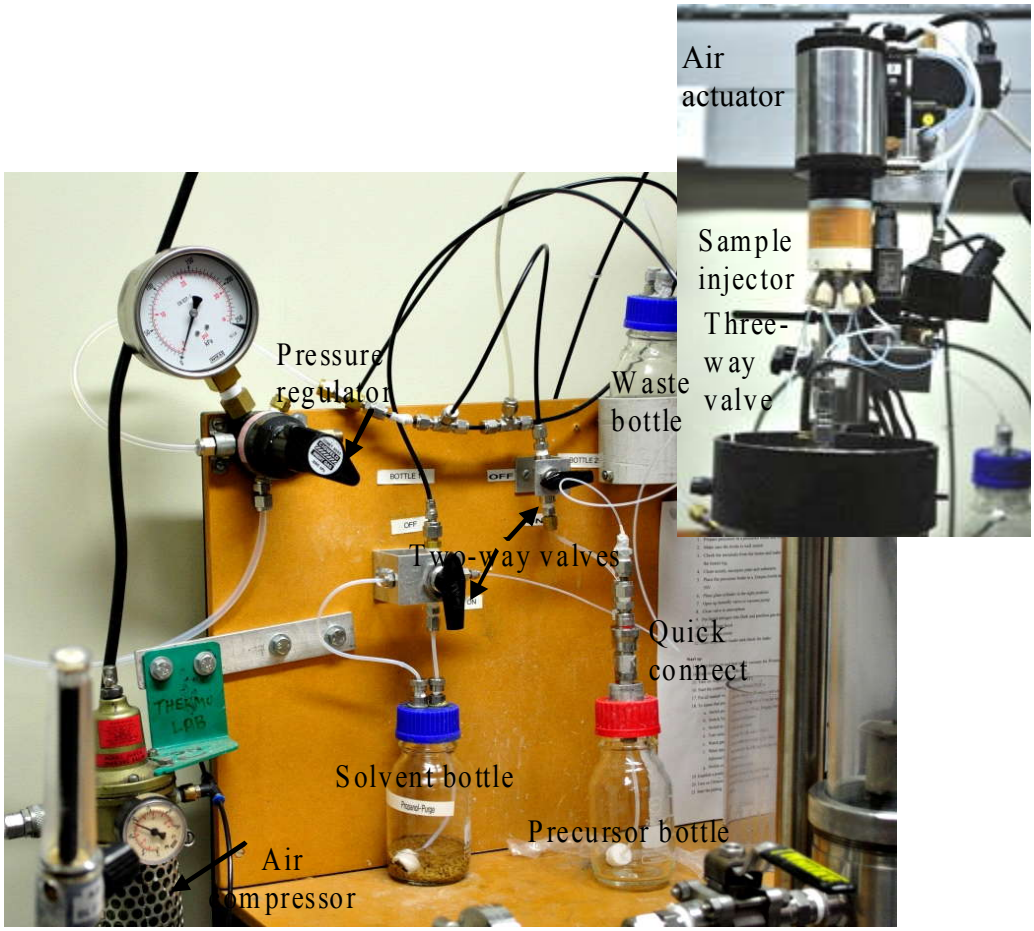

Figure 2-6: The precursor supply system of PP-MOCVD.

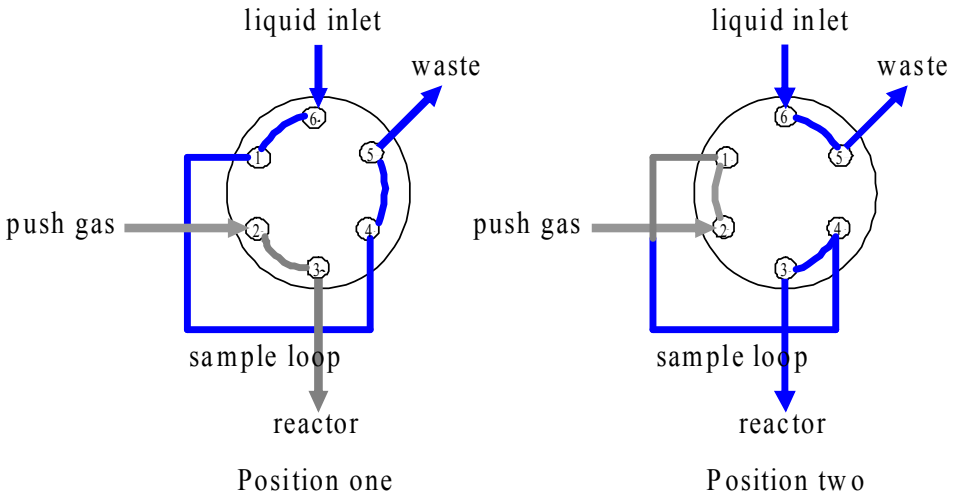

Figure 2-7: Two positions of 6-port external sample loop injector (vici.com).

PP-MOCVD Reactor System

The reactor for PP-MOCVD is a cold wall reactor, which implies that only the substrate is heated. The design of the reactor is determined by the size and geometry of the substrate, application of the deposited film and number of substrates. Figure 2-8 shows the reactor system of the research-scale PP-MOCVD used in this research. The reactor system consists of a reaction chamber made from a glass cylinder. At both ends of the glass tube is an O-ring flange to ensure a vacuum inside the reaction chamber. The top flange is equipped with an ultrasonic nozzle and the precursor metering and injection system. The bottom flange is connected with an exhaust system, thermocouples, heater power supply, pressure gauge and air release valve. Inside the reactor is a susceptor with a heater inside. A molybdenum sheet which acts as a radiation shield was placed around the holder to reduce heat loss to the surroundings. The heater was connected to a power supply using a ceramic connector. Two thermocouples were used to measure the temperature on and inside the susceptor in contact with the heater as illustrated in Figure 2-9.

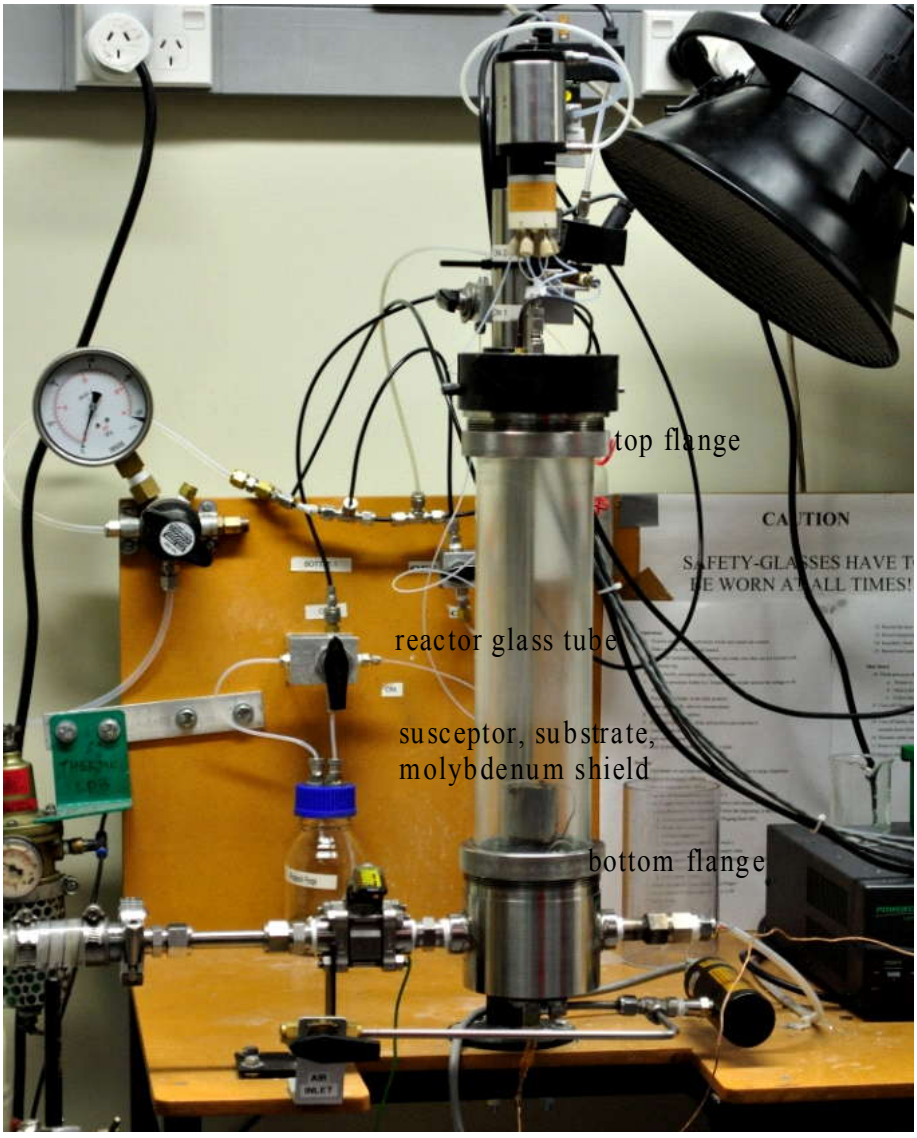

Figure 2-8: The reactor system of PP-MOCVD

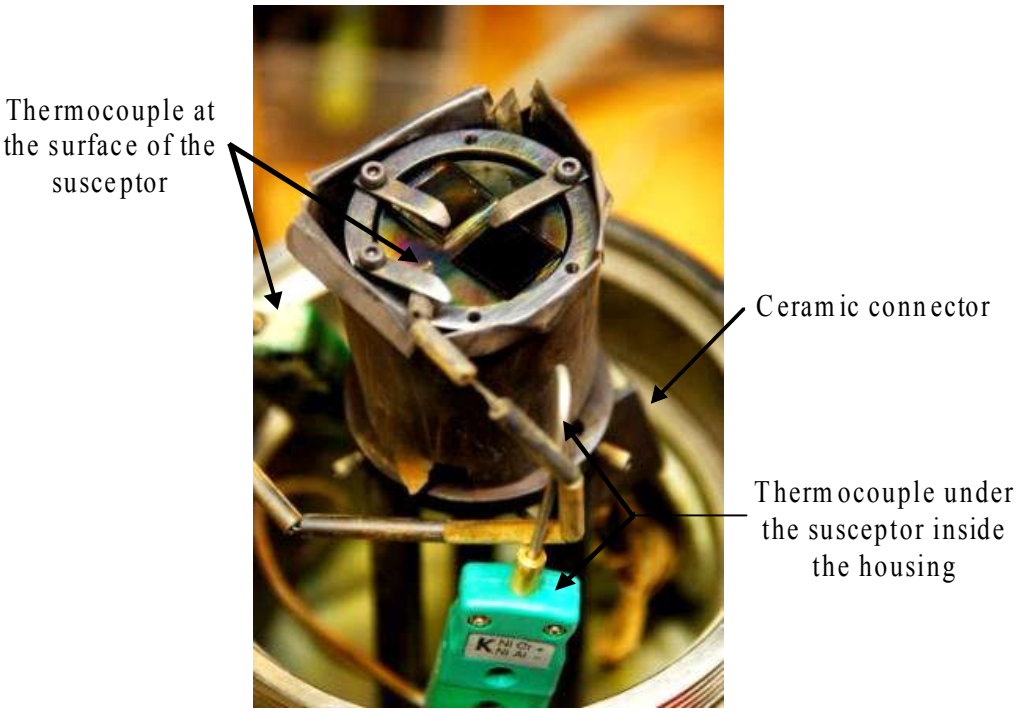

Figure 2-9: The location of two thermocouples and a ceramic connector inside the PP-MOCVD reactor.

PP-MOCVD Ultrasonic Atomiser

One of the principal parts of a PP-MOCVD reactor is the ultrasonic nozzle, which is located at the top flange of the reactor as shown in Figure 2-10. The nozzle generates 18 µm droplets of liquid precursor that cause the precursor to flash evaporate once it enters the low pressure or vacuum reaction chamber. The ultrasonic nozzle uses high frequency sound waves, outside human hearing range, as the input frequency. The 316 stainless steel housing of the nozzle is not ultrasonically active. Figure 2-11 illustrates the components inside and outside the ultrasonic atomiser.

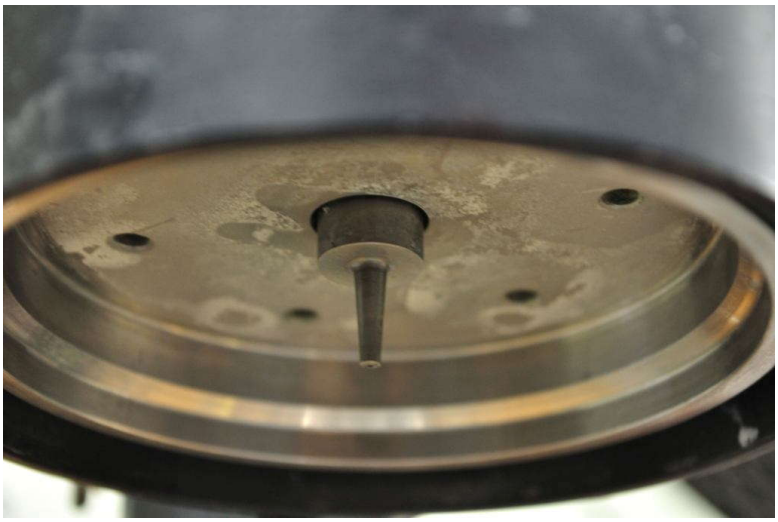

Figure 2-10: The ultrasonic atomiser inside the PP-MOCVD reactor located at the top flange of the reactor.

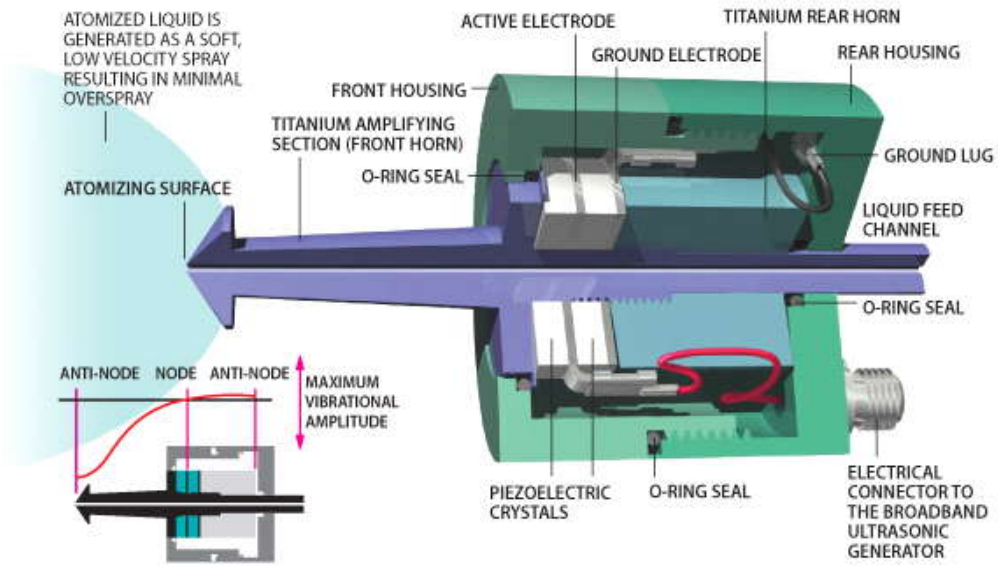

Figure 2-11: The cross-section view of the ultrasonic atomiser. (© Sono-Tek Corporation. All rights reserved)

Many electrically active parts such as piezoelectric transducers, electrodes and electrical connector wires, are assembled inside the ultrasonic atomiser housing. The piezoelectric transducers are made from PZT. The electrical connector is a hermetically sealed subminiature version A (SMA) fabricated from stainless steel. The front and rear horns were made from very high strength titanium alloy (Ti-6Al-4V). Titanium was used because of its good acoustical properties, high tensile strength and very good corrosion resistance.

The length of the ultrasonic nozzle is normally the preliminary specification to control the frequency and vibration amplitude. The length of the nozzle is an integral number of half-wavelengths in order to produce sinusoidal longitudinal waves and keep the antinode at both ends free of the nozzle. The antinodes are where the maximum vibration amplitude is located as shown in Figure 2-11. The frequency of the nozzle is in the range from 25 to 120 kHz depending on the nozzle specification and wavelength. For example, the vibration wavelength is approximately 20.3 cm at 25 kHz while it is 4.1 cm at 120 kHz. The most general frequency used with the nozzle is at 48 kHz, which has a half-wavelength of approximately 5.1 cm. Generally, a high frequency nozzle has a smaller half-wavelength and generates smaller droplets; hence it has a smaller maximum flow capacity than a low frequency nozzle. The power supply for the ultrasonic atomiser is usually up to 15 watts. The droplet size at each nozzle frequency is summarised in Table 2-1.

Table 2-1: The median water droplet size at different nozzle frequencies.

Frequency [kHz]	25	35	48	60	120
Droplet size [μm]	70	49	38	41	18

High frequency sound waves are generated from disc-shaped ceramic piezoelectric transducers which receive electrical energy from a power generator. The transducers convert the electrical energy into mechanical energy in the form of a vibratory motion at the same frequency as the input frequency. The transducers are arranged to have opposite polarity that influences the transducers to expand or contract against each other at an equal force. Because the wavelength is dependent on the frequency, the adjustable power supply controls the frequency and wavelength as well as the nozzle specification, for example, the length of the nozzle. Two titanium cylinders are used to magnify the motion and increase the vibration amplitude at the atomising surface. This vibration amplitude needs to be controlled to avoid non-atomising and cavitation of the precursor droplets. The non-atomising of precursor droplets occurs from lack of energy, which happens when the vibration amplitude is less than a value, which is the so-called critical amplitude. If the vibration amplitude is far more than the critical amplitude, a cavitation will occur.

The nozzle applied throughout this study is operated at the nozzle frequency of 120 kHz. When the metered quantity of liquid precursors is injected into the reaction chamber, the nozzle will generate small droplets of precursors at a droplet size of approximately 15 to 18 μm depending on frequency, density and surface tension. These small droplets evaporate almost immediately when

entering the reaction chamber. With this flash evaporation, the process does not require any carrier gas or a bubbler. The amount of atomised liquid per pulse is controlled by the sample loop in the precursor supply system. The velocity of the precursor molecules depends on the nozzle speed. The velocity of the precursor molecules at the ultrasonic nozzle frequency of 120 kHz is 0.18 to 0.36 $m \cdot s^{-1}$ in general compared to 10.7 to 21.3 $m \cdot s^{-1}$ for a low velocity precursor spray system (Kristinsdottir, 2007).

PP-MOCVD Exhaust System

The exhaust system reduces pressure inside the reactor after flash evaporation to the base level. This system includes vacuum hoses, fittings, valves, a liquid nitrogen trap and a vacuum pump. The liquid nitrogen trap is used to minimise contamination residue from the reaction chamber to the vacuum pump and the back steaming of the residue as well as oil back to the reaction chamber. The exhaust system of PP-MOCVD is illustrated in Figure 2-12.

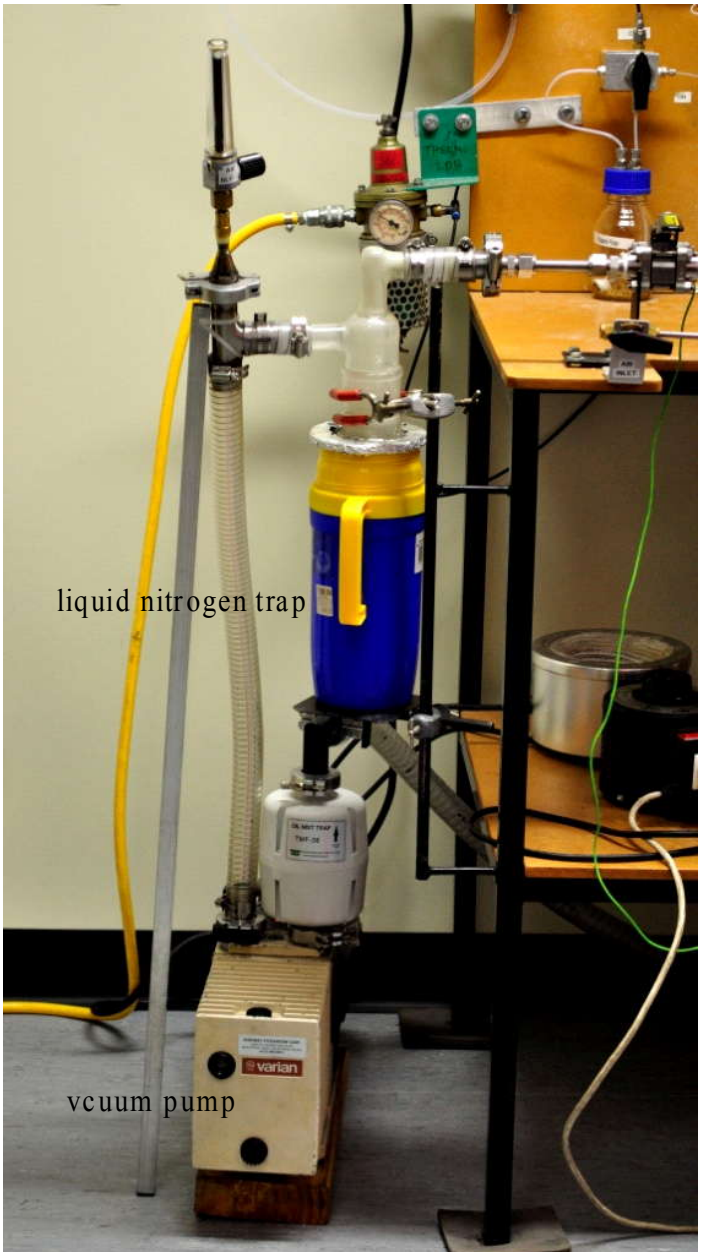

Figure 2-12: The exhaust system of PP-MOCVD.

Figure 2-13: The control system of PP-MOCVD.

PP-MOCVD Control System

The control system controls the electrically actuated equipment including ultrasonic nozzle, temperature, valves, pressure transducer and heater. Software is generally required to control the system, store and interpret the pressure data etc. The control box, as depicted in Figure 2-13, is used to control the solenoid valves and temperature and supply the power to the heater. The power of the nozzle is controlled using a generator that is supplied with the ultrasonic nozzle. The power of the nozzle controls the frequency, hence the droplet size of the precursor. The filling time, injection time, number of pulses and relaxation time are controlled by a National Instruments LabView program. The filling time is the time taken to fill the sample loop with the precursor. The injection time is the time taken to introduce the precursor into the reaction chamber. The filling time should be optimised in order to ensure the sample loop is filled with the precursor and to minimise precursor waste.

PP-MOCVD is a deposition technique that has shown its capability to deposit conformal thin films on featured substrates from liquid metalorganic precursors and has high conversion efficiency from gaseous precursors (Krumdieck et al., 2007a; Krumdieck et al., 2007b; Siriwongrungson et al., 2007). The introduction of liquid precursors into the reaction chamber of PP-MOCVD is similar to ALD in that it allows the precursor to undergo chemical reactions on the substrate surface with uniform flow distribution. The pulsing controls the molecular arrival rate and supplies a rest time for surface diffusion. The pump-down period after each injection removes the reaction products as well as the remaining precursor from the reactor. This helps to minimise carbon

contamination. The high pressure region after the flash evaporation of the liquid precursor assists the growth rate of the film. PP-MOCVD has a reasonably fast growth rate with good step coverage and requires a low deposition temperature. The reactants and products are low in toxicity (Choy, 2003).

PP-MOCVD can deposit films for many applications such as other thin film deposition methods, including thermal and erosion barriers, polymer of thin films for implantable medical devices, sensors, imprint lithography, solar cells, semiconductors, superconductors, photocatalysis and touch screen (Choy, 2003; Leiby, 2006). PP-MOCVD, however, needs more research before it can be scaled up to industrial level.

2.1.4. Review of Atomic Layer Deposition

Atomic layer deposition (ALD) is a sort of a pulsed process. It uses saturated condition in the vapour to grow high quality thin films. There are normally at least two gaseous precursors that are fed into the reactor one at a time on a sequential basis.

ALD was invented, developed and patented in the 1970s by Suntolar and co-workers in Finland (Jones and Hitchman, 2009). Today, ALD can grow high-quality, dense and pinhole-free films on a large surface area with conformality and controllable thickness.

There are many ALD systems as in CVD. Figure 2-14 shows several examples of ALD systems. Figure 2-14 (a) is the single wafer reactor system where the

gases flow at high velocity across the wafer surface because of the relatively small distance between the wafer and the reactor. Figure 2-14 (b) and (c) are also single wafer reactor systems but the gas inlet is at the top with single and multiple holes, respectively. The entire wafer of the top gas inlet reactor system is exposed to the fresh gas. There is a risk of a stagnant gas area owing to the abrupt transitions in the gas channels for this kind of reactor. The stagnant gas causes a longer purge time because the gas will be removed through diffusion instead of convection. The last figure, Figure 2-14 (d), is the batch-type ALD system. The gases are introduced into the chamber at the top and evacuated at the bottom. They convect from the top part down to the bottom part of the reactor and diffuse between the wafers. The number of wafers in a batch is normally between 50 and 150.

In general, an ALD process cycle consists of four steps. The first is the injection of the first precursor, which can be of low vapour pressure, then the first precursor is purged out with an inert gas. After that the second precursor is introduced into the reactor. The purging of the second precursor out of the reactor is the final step of one cycle. The purging step allows the saturated chemisorbed monolayer of the first reactant on the surface to react with following reactants. With these mechanisms, the film is formed by a full or partial monolayer of atoms per cycle. As a result, the thickness can be controlled using the number of cycles (Kim et al., 2003).

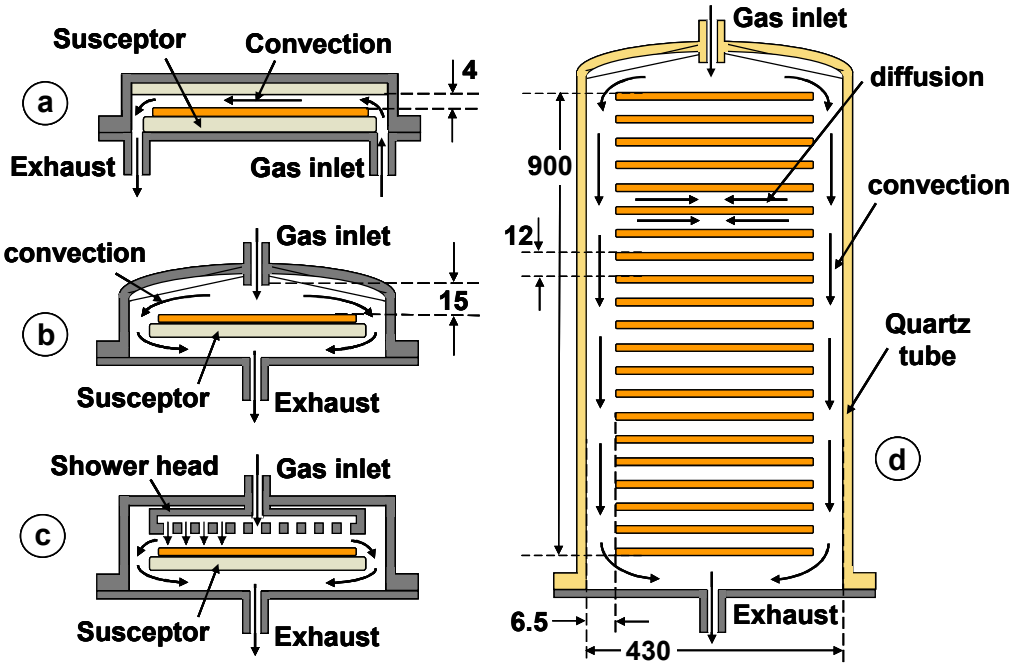

Figure 2-14: Typical ALD reactor systems. (a) cross-flow reactor system (b) top single injector reactor system (c) showerhead reactor system (d) vertical batch reactor system. (Reprinted from Surface & Coating Technology, Grennemaan et al., Batch ALD: Characteristics, comparison with single wafer ALD, and examples, pp 8899–8907, 2007 with permission from Elsevier.)

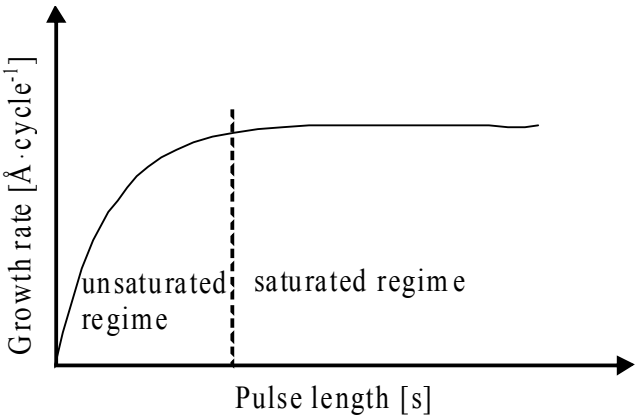

Figure 2-15: The growth rate saturation as a function of the precursor pulse length (Elers et al., 2006).

The growth of the thin films in atomic layer deposition (ALD) is controlled layer by layer at molecular level (Elers et al., 2006). Generally, there are two regimes of growth rate for an ALD cycle as shown in Figure 2-15. The unsaturated growth rate regime occurs after the pulse. The growth rate is self-saturated and reaches the growth rate maximum in the growth rate saturated regime. The pulsing time of the precursor must be long enough for the growth rate to reach the growth rate saturated regime. In the growth rate saturated regime of an ALD, the same number of reactants are going to react on the substrate regardless of the number of molecules (Jones and Hitchman, 2009). ALD is able to deposit films with desirable properties because the process is a self-saturated growth rate mechanism.

ALD is well known for its ability to fabricate excellent uniform and conformal thin films and can produce dense and homogeneous thin films. In addition, ALD provides atomic level composition control. It has good reproducibility and scaling-up ability. However, ALD has a slow growth rate, requires a high vacuum and saturated precursors vapour. The need for a vacuum system and saturated precursors vapour leads to high production costs. There are overlapping of material pulses, non-uniform gas distribution, thermal decomposition of the precursor, impurities and deviation from the ideal ALD growth characteristics in certain types of ALD reactor systems (Elers et al., 2006; Jones and Hitchman, 2009).

ALD has been applied to many applications including the semiconductor industry, production of electronic devices, optics and optoelectronics, anti-reflective coating, carbon nanotube and other fields in nanotechnology.

2.1.5. Review of Physical Vapour Deposition

Physical vapour deposition (PVD) uses the condensation of the vapour phase precursor to deposit the films (Pierson, 2006). It is a line of sight process involving physical rather than chemical reactions (Singh, 1997). The term PVD first appeared in the Vapor Deposition book by Powell and Oxley in 1966 (Powell, 1966).

There are many kinds of PVD, for example evaporation, sputtering and ion plating. PVD such as evaporation and reactive sputtering involve the adsorption of atomic or molecule species on the substrate (Jones and Hitchman, 2009).

PVD is a highly flexible method. The coating thickness from this deposition method can be varied from a few atomic layers up to 10 μm. It requires a low processing temperature, less than 100°C. PVD can be used with many kinds of substrate including non-metallic insulators, plastic and ceramic. PVD has a low deposition rate and produced in small batches depending on the applications and reactor systems. The low deposition rate and batch type reactor lead to time and cost constraints.

The applications of coating by PVD are, for example interconnection-wiring on semiconductors, semiconductor devices, coating for cutting tools, electronic

devices, medical applications and development of material such as high-dielectric and piezoelectric film (Krishna, 2002).

2.2. Deposition Mechanism, Thermodynamics and Mass Transport of CVD and PP-MOCVD

2.2.1. Review of the Deposition Mechanism of CVD

There are three principal steps in the deposition of thin films. These are the transportation of the reactants from the source to the substrates, the adsorption and decomposition of the reactants and the nucleation and growth step (Taga, 2001). Figure 2-16 shows the detailed schematic of the deposition mechanism of thin film for a cold wall CVD reactor where only the substrate is heated. Firstly, the reactants are evaporated and transported into the reaction zone via convection and diffusion mass transport. In this zone, the reactants and by-products are produced by chemical reaction in the gas phase and form intermediate species. Those intermediate species are adsorbed on the substrate surface only when the deposition or substrate temperature is lower than the dissociation of the intermediate phase. If the deposition or substrate temperature is higher than the decomposition of the intermediate species, a homogeneous gas phase reaction can occur and generate powder and volatile by-products. This powder may be deposited and form film on the substrate surface but is non-uniform with poor adhesion and a porous microstructure leading to a decrease in efficiency as well (Choy, 2003).

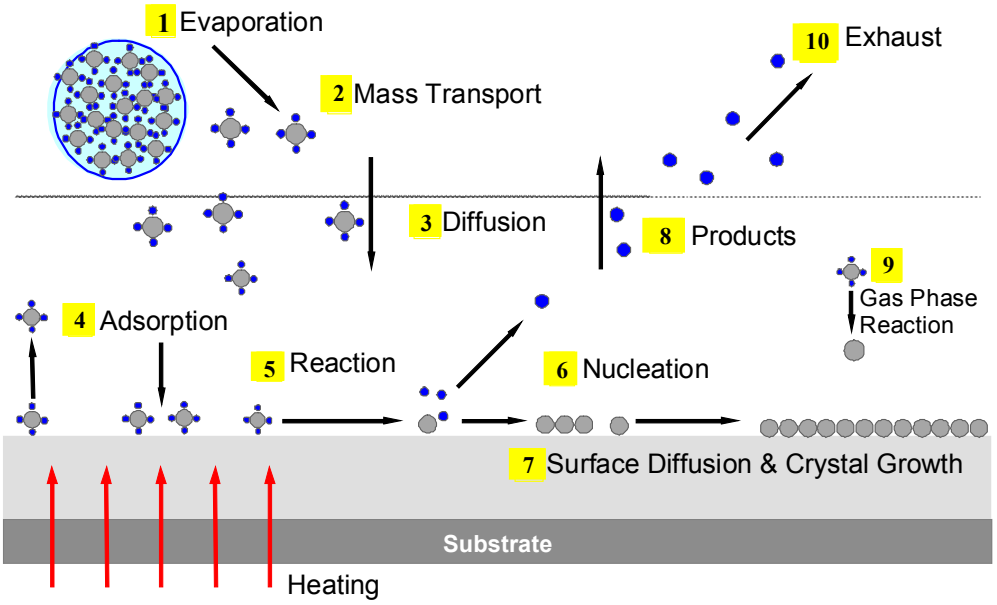

Figure 2-16: The deposition mechanism of a cold wall reactor CVD process. Diagram courtesy of S. P. Krumdieck.

In the further step when the temperature is lower than the decomposition temperature of the intermediate species, the reactants and by-products are adsorbed, react, nucleate and form crystal growth. The remaining reactants along with volatile by-products on the substrate surface are desorbed and diffused back into the reaction chamber and transported out of the reactor by a vacuum pump.

2.2.2. Review of the Thermodynamics of CVD

The thermodynamics of CVD are explained using the relationship between growth rate and deposition temperature. There are three different growth rate regions, which depend on the rate limiting step. The growth or rate limiting step is the slowest step in a deposition process. The three possible growth

limiting steps in a deposition process are mass transport of the first kind, mass transport of the second kind and surface kinetics (Choy, 2003; Morosanu, 1990). Figure 2-17 illustrates the three rate limiting steps on the relationship between natural logarithmic growth rate and inverse deposition temperature.

Mass Transport of the First Kind of Control

A process is controlled by the mass transport of the first kind at a high to ultra-high deposition temperature. The mass transport of the first kind is the rate limiting step when the process is in equilibrium that is determined by mass input at high temperature. The reactant feed or product removals to or from the deposition zone are the slowest steps. The growth rate depends on deposition temperature because of the variation of the total enthalpy of the process. The temperature influences the equilibrium constant, K, as Equation (2-1)

$$K = Ce^{-\Delta H / RT} \tag{2-1}$$

where ΔH is the reaction enthalpy at constant pressure and C is a constant.

The gradual decrease in growth rate at ultra-high temperature is due to depletion of reactants, increase in desorption rate of the products, homogeneous gas phase nucleation in addition to the heterogeneous reactions and particle formation (Morosanu, 1990).

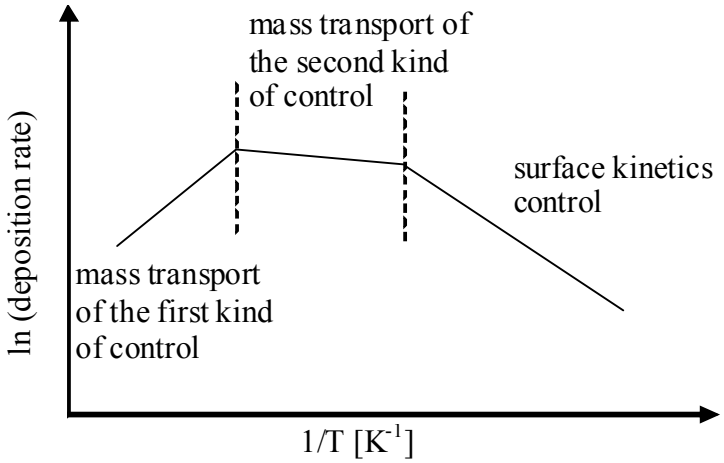

Figure 2-17: The natural logarithmic of growth rate and inverse deposition temperature including the Arrhenius plot.

Mass Transport of the Second Kind of Control

In mass transport of the second kind of control, the reactant transfer between the main gas flow and the substrate surface are the slowest steps. The mass transfer between the main gas flow and the substrate surface is through diffusion or convection. This implies that the diffusion of the active gaseous species through the boundary layer to the surface is the rate limiting step. The diffusion coefficients vary slightly with temperature; hence the deposition flux or growth rate depends weakly on the temperature. The growth rate is almost constant with a remarkably smaller slope than the surface kinetics and mass transport of the first kind of control. The diffusion coefficient and gas velocity inversely depend on pressure. Therefore, the process which operates at high pressure is under the mass transport of the second kind of control (Ohring, 2002).

Surface Kinetics Control

At low deposition temperature, the growth rate depends strongly on temperature because the process is limited by surface kinetics or reaction rate. Surface kinetics include chemisorptions, chemical reactions, surface migration, lattice incorporation and product desorption. Chemical reactions occur when at least the activation energy, E_a, is reached. The growth rate of a heterogeneous process that is controlled by surface kinetics increases in an exponential manner. The exponential relationship follows the Arrhenius law as shown in Equation (2-2)

$$Growth\ \ rate = A\exp\left(-\frac{E_a}{RT}\right) \qquad (2\text{-}2)$$

where A is a constant, R is the ideal gas constant ($J \cdot K^{-1} \cdot mol^{-1}$) and T is the temperature (K).

2.2.3. Review of Mass Transport of CVD

The reactions inside the CVD reactor and on the substrate surface are related to mass transport phenomena. In a CVD system, two dimensionless numbers are normally used to characterise the fluid inside the system. One number is the Reynolds number (Re) and another is the Knudsen number (Kn). The other important dimensionless numbers include Prandtl, Schmidt, Grashof, Rayleigh, Peclet and Damkohler numbers (Ohring, 2002). The Peclet number describes the transport of the molecules whether it is convection or diffusion dominated. A large Damkohler (surface) number implies that the diffusion is the rate

limiting step while a small Damkohler (surface) number means the surface reaction is the rate limiting step. The Damkohler (gas phase) explains the chemical reactions to the equilibrium condition. Grashof and Rayleigh numbers explain the natural convection which affects the flow field. The meaning of each dimensionless number is summarised in Table 2-2.

Table 2-2: Definition of certain dimensionless numbers that are used in mass transport (Ohring, 2002).

Number	Definition	Physical interpretation
Reynolds	$\mathrm{Re} = \frac{\rho u L}{\mu}$	Ratio of inertia forces to viscous forces
Knudsen	$Kn = \frac{\lambda}{L}$	Ratio of gas molecules mean free path to characteristic length
Prandtl	$Pr = \frac{C_p \mu}{K}$	Ratio of momentum diffusivity to thermal diffusivity
Schmidt	$Sc = \frac{C_p \mu}{D}$	Ratio of momentum diffusivity to mass diffusivity
Peclet (mass)	$Pe_m = ReSc$	Ratio of convective mass flux to diffusive mass flux
Damkohler (surface)	$Da_s = \frac{\dot{R}_s L}{C_{in} D}$	Ratio of chemical reaction rate to diffusion rate
Damkohler (gas phase)	$Da_g = \frac{\dot{R}_g L}{C_{in} u}$	Ratio of chemical reaction rate to bulk flow rate
Grashof (thermal)	$Gr_t = \frac{g\rho^2 L^3 \Delta T}{\mu^2 T_r}$	Ratio of buoyancy force to viscous force
Rayleigh	$Ra = GrPr$	Ratio of buoyancy force to viscous force

Note: ρ is mass density ($kg \cdot m^{-3}$), u is fluid flow velocity ($m \cdot s^{-1}$), L is characteristic length (m), μ is viscosity ($Pa \cdot s$), λ is gas molecular mean free path (m), C_p is specific heat ($J \cdot kg^{-1}K^{-1}$), K is thermal diffusivity ($m^2 \cdot s^{-1}$), D is mass diffusivity ($m^2 \cdot s^{-1}$), C_{in} is input gas concentration ($mol \cdot m^3$), g is gravitational constant ($m \cdot s^2$), $\dot{R}_s$ is surface reaction rate ($mol \cdot m^{-2}s^{-1}$), $\dot{R}_g$ is gas reaction rate ($mol \cdot m^{-2}s^{-1}$), ΔT is difference between hot and cold temperature (K), T_r is reference temperature (K).

Reynolds Number

The Reynolds number, Re, is an important dimensionless number in fluid dynamics and heat transfer problems. It is used to characterise the flow of a fluid and to delineate different flow regimes. Re measures the ratio of inertia forces to viscous forces. Considering the fluid flow in a circular pipe, the inertia forces depend on mass density, ρ (kg·m^{-3}), and viscosity, μ (Pa·s). The viscous forces are the ratio of characteristic length, L (m), such as tube diameter to the fluid flow velocity, u (m·s^{-1}). Re is defined as Equation (2-3).

$$\mathrm{Re} = \frac{\rho u L}{\mu} \tag{2-3}$$

The flow is in the laminar flow regime when the Re is less than 2,100. The viscous forces are dominant and the flow is rather smooth with constant fluid flow motion. The flow is in the transition flow regime where laminar and turbulent flow is possible when the Re is between 2,100 and 4,000. The turbulent flow occurs when Re is more than 4,000. The inertial forces are dominant, and the flow is random with fluctuations. Most of the CVD reactors operate in the laminar flow regime when the Re is less than 100 because of the low precursor flow rate (Roth, 1990).

The Re is used to determine the thickness of the viscous boundary layer, Δ (m). The thickness of the boundary layer is inversely proportional to the square root of the Re as Equation (2-4)

$$\Delta = \sqrt{\frac{x}{\mathrm{Re}}} \tag{2-4}$$

where x is the distance from the inlet of the flow direction (m). The thickness of the viscous boundary layer is thinner when the flow velocity is high and the distance from the inlet is short. On the contrary, the thickness of the viscous boundary layer increases with the increase of the distance from the inlet and decrease of the flow velocity (Pierson, 2006).

Knudsen Number

The Knudsen number, Kn, is the ratio of the mean free path of the gas molecules, λ (m), to the characteristic length perpendicular to the flow direction. It defines the limit between viscous, intermediate and molecular flow regimes. The characteristic length is an aperture size normal to flow direction. It can be the reactor diameter or initial trench mouth width depending on the consideration. The mean free path of the gas molecules is defined as the average distance travelled by a molecule before it collides with another molecule as shown in Equation (2-5)

$$\lambda = \frac{RT}{\sqrt{2}\pi d^2 N_A P} \tag{2-5}$$

where R is the ideal gas constant ($m^3 \cdot Pa \cdot mol^{-1} \cdot K^{-1}$), T is the temperature (K), d is the effective molecular diameter (m), N_A is the Avogadro's number (mol^{-1}) and P is the pressure (Pa).

The flow regime is categorised into three ranges using Kn (Roth, 1990).

Viscous flow	Kn < 0.01
Transition flow	0.01 <Kn < 1
Molecular flow	Kn > 1

At low Kn, Kn less than 0.01, or when the flow is in the viscous flow region, intermolecular collisions dominate. The gas phase reactants are convected through the reactor by other molecules in the carrier gas. The reactants diffuse from the bulk gas flow to the substrate surface. The concentration gradient acts as the driving force. The Navier–Stokes equation is normally enough to predict flow characteristics because all the gas molecules behave as a continuum. The mass transport in a continuum flow CVD reactor depends on the bulk gas flow velocity, the physical properties of the fluid, the pressure gradient from inlet to outlet of the reactor and the geometry of the solid surfaces, which interact with the flow (Jones and Hitchman, 2009). This continuum flow pattern determines the arrival rate of the precursor molecules to the substrates. The precursor molecules are diffused through the boundary layer. The boundary layer is the solid-fluid interaction zone.

The Re that is used to predict the thickness of the boundary in the laminar flow is used to describe the characteristic of the flow of a flat substrate in a horizontal tubular CVD reactor in this flow regime. The kinematic viscosity in the Re is used to model the fluid dynamics because it is related to the momentum diffusivity of the fluid. The kinematic viscosity is the ratio of viscosity to mass density of the fluid. The intermolecular momentum transfer depends on the gas density while the momentum transfer of the molecules depends on the viscosity of the flow. The momentum and mass diffusion boundary layer are normally assumed to be the same because the physics that are used to determine the momentum and mass transfer are similar. The momentum transfer occurs when zero-velocity molecules at the surface desorb

and bump into other molecules near the surface. This momentum transfer creates a shear force when the molecules of the bulk flow move along the substrate surface. This shear force to the surface area of the substrate is called viscosity, and this is not sensitive to pressure, while density is strongly dependent on pressure. This leads to an increase in kinematic viscosity when decreasing the pressure.

When Kn is more than 1, the flow is in the molecular flow regime. The molecules are in random motion or ballistic. The molecules will move from the higher density to lower density of the molecules or from higher pressure to lower pressure. The free molecular motion is strongly dependent on the line of sight between two pressures that are characterised by the component conductance. The throughput, Q ($Pa \cdot m^3 \cdot s^{-1}$), of a steady flow rate is a function of pressure and conductance, C ($m^3 \cdot s^{-1}$), as written in Equation (2-6).

$$Q = C(P_1 - P_2) \tag{2-6}$$

The throughput and conductance are important characteristics because they affect the reactor pressure, P (Pa). The conductance changes the exhaust speed, S ($m^3 \cdot s^{-1}$), as shown in Equation (2-7)

$$S = \frac{S_p}{1 + \frac{S_p}{C_{sys}}} \tag{2-7}$$

where S_p ($m^3 \cdot s^{-1}$) is the volumetric pump speed at the nominal operating pressure. The exhaust speed and the throughput can be adjusted to achieve the required reactor pressure as written in Equation (2-8).

$$S = \frac{Q}{P} \tag{2-8}$$

The conductance is generally not a function of pressure when the flow is in the molecular flow regime. This independence of the pressure of the conductance depends on the local pressure and component geometry (Roth, 1990). The relations of conductance for simple component geometry can be found in most of the vacuum science handbooks. The conductance of an entire system, C_{sys}, is written as Equations (2-9) and (2-10) for series and parallel components connections, respectively.

$$\frac{1}{C_{sys}} = \frac{1}{C_1} + \frac{1}{C_2} + \frac{1}{C_3} + \ldots \tag{2-9}$$

$$C_{sys} = C_1 + C_2 + C_3 + \ldots \tag{2-10}$$

The whole system of a series components connection is limited by the smallest conductance component. The conductance of a parallel components connection can be made by adding equipment such as parallel pumps.

2.2.4. Review of Mass Transport of PP-MOCVD

The idea of pulsing is to control the molecular flux to be as uniform as possible. When the precursor enters the low pressure reaction chamber, it undergoes a rapid expansion. The expansion forces are dominant over viscous forces or bulk momentum forces, resulting in an "expansion" mass transport regime (Krumdieck et al., 2007a). This regime exists only when the pressure inside the reaction chamber is either increasing or decreasing at a sufficiently

fast rate. The precursor injection time and pulsing cycle time are crucial in controlling flow field uniformity established by expansion-dominated mass transport. It has been reported that the convection field is uniform throughout the reactor volume up to the pressure studied of 20 kPa, by keeping the precursor injection time and pulsing cycle time in the particular ranges depending on the reactor geometry and vacuum pump speed (Krumdieck et al., 2005).

Figure 2-18 illustrates an ideal pressure profile inside the PP-MOCVD reaction chamber, which was used in this study as a function of processing time. *P(t)* is the reactor pressure at any processing time, *t* (sec). It should be noted that in the real operation situation, occasionally there is a small peak between the pressure at the minimum, P_{min}, and maximum, P_{max}. This is due to the mechanical operation of the valves. Pressure reaches maximum after the liquid precursor is injected into the reactor at injection time, t_i. The rapid raising of the pressure to maximum is due to the flash evaporation of the liquid precursor droplets. These precursor droplets were generated by the ultrasonic nozzle. After the reactor pressure reaches the maximum, a vacuum pump, which is installed with a cold trap, pumps the pressure inside the reactor back to the pressure prior to the next liquid precursor injection. The period after the pressure reaches the minimum before the next liquid injection is called relaxation time. The processing time between each liquid injection is one pulse cycle, t_p-t_0.

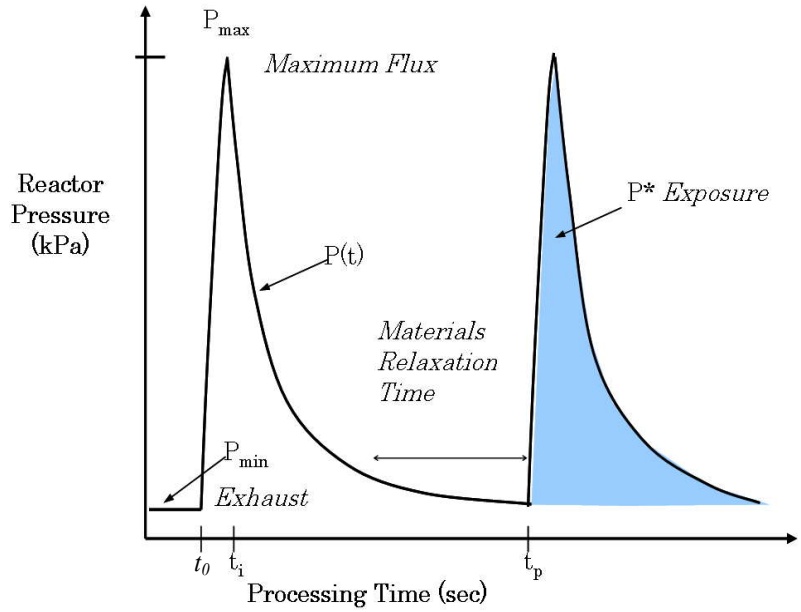

Figure 2-18: The ideal pressure profile inside the PP-MOCVD reactor as a function of processing time.

The reactor pressure at any time can be calculated based on the molecular balance inside the reactor, ideal gas law and vacuum science theory. The molecular balance inside the reactor during one cycle is as Equation (2-11)

$$n_L dt - \frac{S_P}{V_R}((n(t) - n_{\min})dt = d(n(t) - n_{\min}) \qquad (2\text{-}11)$$

where t is the processing time (sec), n_L is the molecular leak rate, which is normally small compared to the number of molecules injected at the beginning of each cycle and the evacuation pump rate, $n(t)$ is the number of molecules remaining in the reactor at any time during the pulse cycle, n_{min} is the number of molecules in the reactor at the minimum pressure, V_R is the reactor volume (m^3). The number of molecules in the reactor at any time during a pulse cycle could be written as Equation (2-12).

$$n(t) = (n_i + n_{\min}) - \int_0^t n(t)dt \tag{2-12}$$

where n_i is the number of molecules from the sample loop with specific supply volume, $\int_0^t n(t)dt$ is the number of molecules evacuated in time t from the beginning of the cycle. By applying the ideal gas law and assuming a constant temperature, the number of molecules injected from a sample loop at the beginning of each cycle is given as Equation (2-13)

$$n_i = (P_{\max} - P_{\min})\frac{V_R N_A}{RT} \tag{2-13}$$

where N_A is Avogadro's number, R is the universal gas constant, and T is the vapour temperature inside the reactor. If the number of molecules from $t = 0$ to $t =$ t were integrated, and Equations (2-12) and (2-13) substituted into (2-11), the pump-down pressure could be written as Equation (2-14)

$$P(t) = (P_{\max} - P_{\min})e^{-\frac{(S_P/V_R)t}{1+S_P/C_{sys}}} + P_{\min} \tag{2-14}$$

where *P(t)* is the reactor pressure at any processing time. By substituting Equation (2-7) and pump-down constant, τ (sec), relationship, Equation (2-14) could be written as Equation (2-15).

$$P^*(t) = \frac{P(t) - P_{\min}}{P_{\max} - P_{\min}} = \exp\left(\frac{-t}{\tau}\right) \tag{2-15}$$

Equation (2-15), $P^*(t)$ is a dimensionless reactor pressure. It could be written as Equation (2-16) to calculate the pressure inside the reactor at any processing time.

$$P(t) = P_{\min} + (P_{\max} - P_{\min}) \exp(\frac{-t}{\tau}) \tag{2-16}$$

The evacuation time, or the pump-down constant, τ (sec), can be determined experimentally or from Equation (2-17).

$$\tau = \frac{V_R}{S} \tag{2-17}$$

The processing time for a pulsing cycle needs to be at least four times the reactor pump-down constant for the P_{max} and P_{min} to be repeated throughout the deposition process.

The area under the reactor profile is called exposure, P^* (Pa·s). The exposure represents the total molecular flux during each pulse for PP-MOCVD. It is directly related to the P_{max} for a stable operation. The molecular flux of vapour to the substrate surface, ϕ ($m^{-1} \cdot s^{-1}$), is expressed using the gas dynamics relation as shown in Equation (2-18)

$$\phi(t) = \frac{N_A P(t)}{\sqrt{2\pi MRT}} \tag{2-18}$$

where M is the precursor molecular mass ($kg \cdot mol^{-1}$). The molecular flux is a function of processing time because PP-MOCVD is a non-steady process. By substituting Equation (2-16) into (2-18), integrating the molecular flux over the

processing time and multiplying by the concentration of the precursor, C_{mo} (mol%), the total molecular flux per unit area per pulse is as shown in Equations (2-19) and (2-20).

$$J = \frac{N_A C_{mol\%} P^*}{\sqrt{2\pi MRT}} \tag{2-19}$$

$$J = \frac{N_A C_{mol\%}}{\sqrt{2\pi MRT}} \left(P_{\min} t_p + \tau \left(P_{\max} - P_{\min} \right) \left(1 - \exp\left(\frac{-t_p}{\tau} \right) \right) \right) \tag{2-20}$$

The dimensionless total molecular flux per unit surface could be written as a function of reactor pressure using Equation (2-17) as shown in Equation (2-21)

$$J^* = \frac{J}{J_{\max}} = \frac{P^*}{P_{\max} t_p} \tag{2-21}$$

where $J_{\max} = \frac{N_A C_{mo}}{\sqrt{2\pi MRT}} P_{\max} t_p$.

Krumdieck et al. (Krumdieck et al., 2007b) have developed a non-dimensional parameter, pulse exposure, *PE*. The pulse exposure relates all the variables that influence the vapour molecular flux to the substrate surface over a pulse cycle. As can be seen in Equation (2-20), peak pressure, processing time and evacuation time constant are important to the molecular flux. Peak pressure can be represented by the relationship of precursor vapour pressure, precursor concentration, precursor injection volume, reactor volume and base pressure. The proposed dimensionless pulse parameter by Krumdieck et al. (Krumdieck et al., 2007b) is shown in Equation (2-22)

$$PE = C_{mo} \frac{P_{\min}}{P_{vap}} \frac{\nu_L}{V_R} \frac{\tau}{t_p} \qquad (2\text{-}22)$$

where P_{vap} is the precursor vapour pressure (Pa) and ν_L is the liquid precursor injection volume (µl).

2.3. Microstructures and Nucleation of Thin Films

The interaction of deposition rate, substrate temperature and nucleation influence the microstructure of thin films in CVD (Krumdieck, 1999). The lower the deposition temperature the higher the content of residual impurities and the films are likely to be amorphous. When the film is polycrystalline, a porous cauliflower structure is normally found at low deposition temperature, low nucleation rate and high deposition rate. Fine-grained microstructure is a commonly desired structure, and this occurs at low pressure, moderate temperature and high precursor concentration, or at supersaturation condition or high gas velocity. Under these operating conditions, the nucleation rate and the deposition rate are high with moderate surface mobility. The grain size is directly dependent on the film thickness. When the film becomes thicker or the film is deposited at high temperature, high pressure and low precursor concentration or low gas velocity, the deposited film tends to be columnar (Pierson, 2006). At high temperature, the grain growth grows uninterruptedly towards the reactant source. The film tends to be prismatic columnar when the nucleation rate is higher and the deposition rate is faster than the columnar microstructure growth conditions.

The microstructure of films also depends on the thickness of the films. Certain studies focused on the influence of TiO_2 film thickness on the photocatalytic activity which is generally less than a micron (Chen and Dionysiou, 2006; Heikkilä et al., 2009; Jung et al., 2005). Fine particles are generally deposited on the substrate surface in the early stage of the deposition. In the case of columnar structure, the size of the column increased as the thickness of the film increased (Jung et al., 2005).

The growth limiting step affects the growth mode, which also depends on substrate surface contamination and sticking coefficient. As illustrated in Figure 2-19, there are three possible growth modes: layer by layer or Frank-van der Merwe (FM) mode, island growth or Volmer-Weber (VW) mode and mixed layer-island or Stranski-Krastanov (SK) mode. FM mode is normally suitable for most of the applications but it is found in a small number of film-substrate combinations (Gilmer et al., 1998). In general, the layer of the film in FM mode may vary in height over distances of tens or even hundreds of monolayers. This is because of random impingement of atoms and two-dimensional nucleation. The precursor may aggregate into clusters either on a bare substrate or on a deposited layer, which means VW and SK mode, respectively. The initial stages of film deposition of metal or semiconductor on oxide substrates are VM mode. The SK mode is commonly found in metal-metal and metal–semiconductor processes.

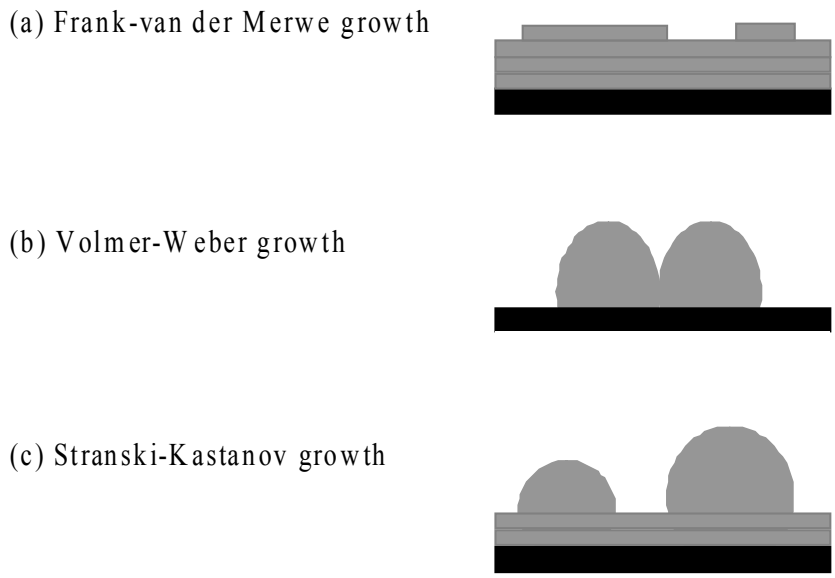

Figure 2-19: Three principal growth modes of thin films deposited on crystalline substrate with large surface mobility: (a) layer by layer, (b) island growth and (c) mixed layer-island mode (Gilmer et al., 1998; Krumdieck, 1999).

Various potential energies influence the nucleation and growth processes of thin films. Interfacial free energy is a key driving force for different morphologies (Gilmer et al., 1998; Ohring, 2002). The interfacial free energies could be divided into three categories: free energy between the deposited film and the substrate, γ_{FS}; free energy between the deposited film and the vapour interface, γ_{FV}; and free energy between the substrate and the vapour interface, γ_{SV}. When γ_{SV} is large or the precursor molecule tends to stick to the substrate more than to the deposited film, it is the FM mode as illustrated in Figure 2-19. On the contrary, when γ_{SV} is less than γ_{FS} and γ_{FV}, it is the VW mode. VM mode occurs when the atoms or molecules are more strongly bound to each other than to the substrate. The SK mode is expected when the reactive sticking coefficient of the substrate is equal to that of the deposited film. However, frequently the differences between the free energies of atoms in the interior of

the deposited films and in macroscopic crystals need to be considered to explain the SK mode.

The heterogeneous nucleation and growth can be divided into seven regimes using material and experimental parameters as shown in Figure 2-20 (Morosanu, 1990). The parameters considered are substrate temperature, T, adatom arrival rate, J, adsorption energy of an isolated adatom on the substrate, E_a, and adsorption energy of an adatom on a monolayer of the condensate, $E_{a'}$. Random nucleation occurs at the lowest substrate temperature, T_{min}, and the highest adatom arrival rate, J_{max}. Amorphous microstructure is formed by random nucleation. Layer by layer nucleation appears when $E_a \geq E_{a'}$ with the substrate temperature and adatom arrival rate at intermediate values, T_i and J_i, respectively. An unstable solid with limited thickness is formed in the equilibrium adsorption nucleation and growth regime. This occurs when $E_a \geq E_{a'}$ with the substrate temperature more than the intermediate value and the adatom arrival rate lower than the intermediate value. The next two nucleation and growth regimes are commonly found in CVD. They are 3-D nucleation at low and high temperatures. The binding forces between atoms in the cluster are stronger than the cluster and the substrate, $E_a < E_{a'}$. The size of the cluster is inversely proportional to the binding energy. There is a growth that starts with the first monolayer, when $E_a > E_{a'}$, then 3-D starts nucleating on top of the monolayer. No nucleation is expected when either E_a or $E_{a'}$ or both are very small. The nucleation could occur when the substrate has defects where the binding energy of atoms may change to a higher value.

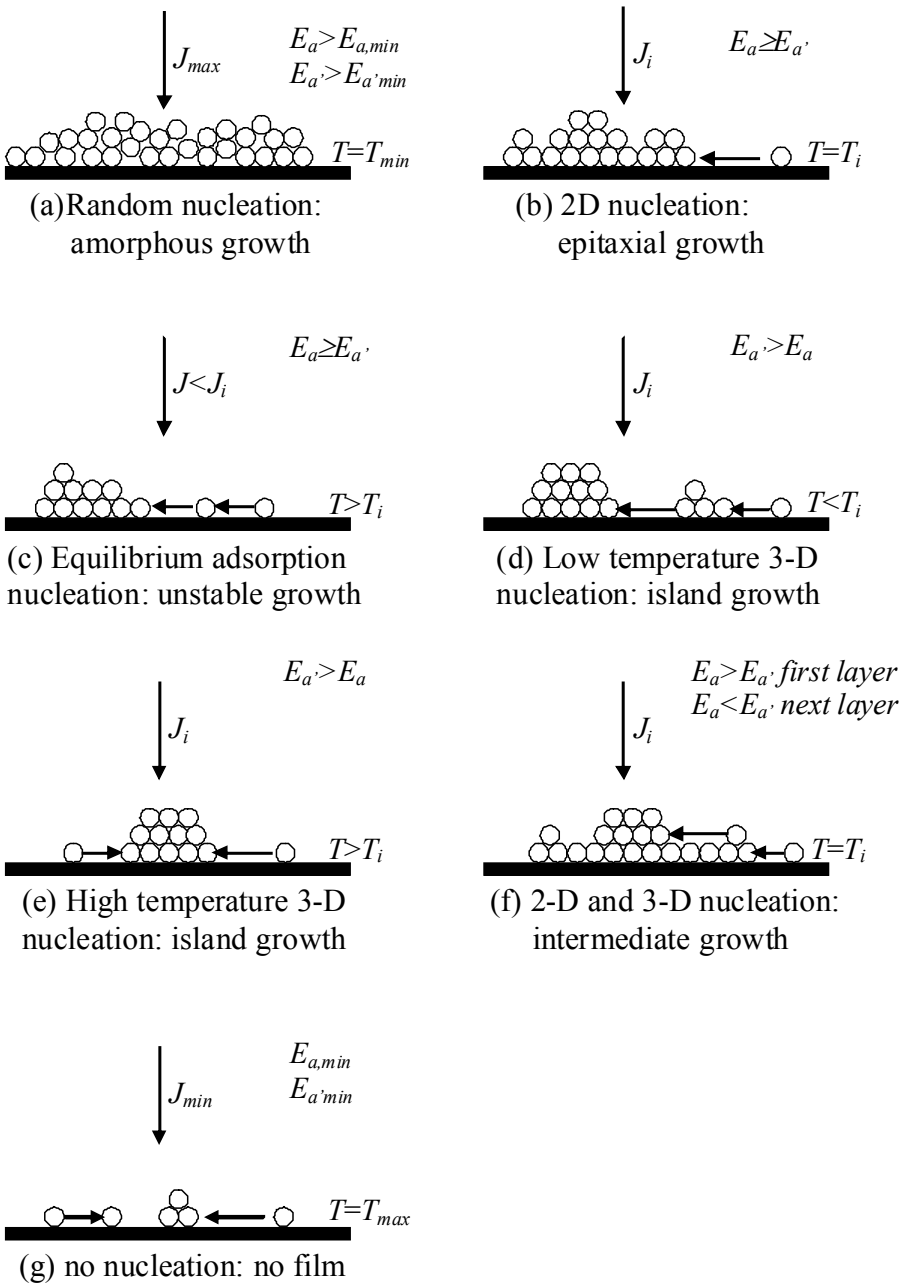

Figure 2-20: The effects of adatom arrival rate, J, substrate temperature, T, adsorption energy of an isolated adatom on the substrate, E_a, and adsorption energy of an adatom on a monolayer of the condensate, $E_{a'}$, on heterogeneous nucleation and growth regimes (Krumdieck, 1999; Morosanu, 1990).

2.4. Review and Literature Review of the Conformality of Thin Films

Conformal step coverage is defined as the even thickness of the film on the horizontal and vertical surfaces of a substrate (Ohring, 2002). The substrate can be flat or have 3-D features. Conformality is important and is required for certain applications including microelectronic and optical coatings. In the development of electronics, the sizes of the structures have been decreasing while the aspect ratios have been increasing. It is therefore more difficult to deposit conformal thin films on 3-D external and internal shapes.

Figure 2-21 illustrates the conformality relating to deposition rate, gas diffusion and surface diffusion. Conformal step coverage is expected to be controllable when surface kinetics is the growth limiting step at a reasonable rate or at low substrate temperature. The reasonable rate means the gas diffusion should be about the same rate as the surface diffusion. When the surface and gas diffusion are faster than the deposition rate, coating levelling occurs. The interference with colour change is a parameter that shows the non-conformality in thickness. The non-conformal coating generally occurs in a mass transport limited region or at high substrate temperature when the deposition rate is faster than surface and gas diffusion (Chen and Derking, 1993; Krumdieck, 1999). Generally, conformality depends on the control of the decomposition reaction on the substrate surface or deposition rate, surface kinetics of gas molecules on the substrate surface or surface diffusion and mass transport of gas phase reactants to the substrate surface or gas diffusion or

arrival rate of the molecules. These process controls rely on the precursors used, the deposition conditions and the delivery system of the precursor into the reactor. Deposition conditions include temperature, pressure, supersaturation of the precursors and the selection of chemical reactions. The pressure affects the thickness of the boundary layer, hence the diffusion and arrival rate. The delivery system affects the convection and diffusion of the precursor to a heated substrate. The principal factors that influence the film growth rate and properties include the precursor chemistry, substrate temperature, evaporator temperature, impurity incorporation, precursor supply rate and concentration in the carrier gas, which is determined by the carrier gas flow rate. The phase of deposited TiO_2 and impurities depends strongly on deposition temperature.

Conformal thin films have been deposited, modelled and reported by many research groups using a range of precursors, operating parameters and reactors. Theoretically, a conformal thin film on a 3-D structure can be achieved by balancing the molecular arrival rate of the vapour, a thermally activated chemical reaction on the surface, physical adsorption on the surface and surface diffusion. It has been stated that the conformal films can only be deposited when the deposition is kinetically controlled (Chen and Derking, 1993).

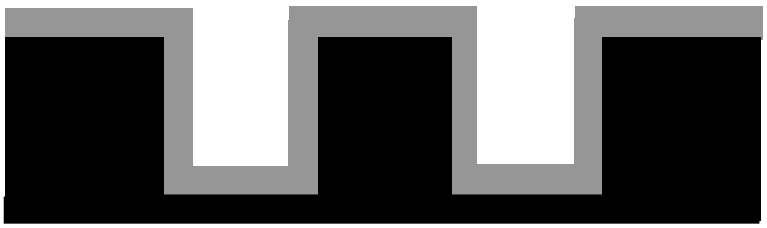

Conformal coverage:
Parity between gas diffusion and surface diffusion

Leveling:
Surface and volume diffusion > deposition rate

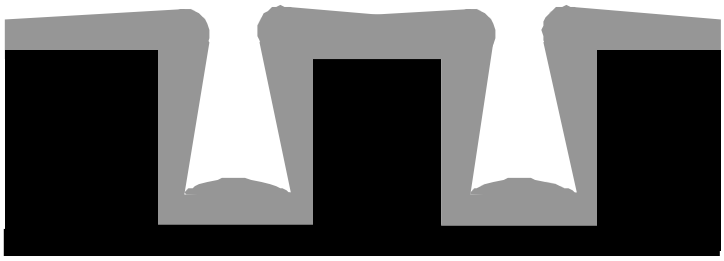

Non-conformal coverage:
Deposition rate > surface and volume diffusion

Figure 2-21: The effect of deposition rate, surface diffusion and gas diffusion on conformality of 3-D internal and external shapes (Krumdieck, 1999).

Table 2-3: Summary of studies of conformal thin films at various deposition methods, conditions, substrates and materials on trench and/or via.

Deposition Method	**Material**	**Substrate**	**Trench/Via Dimension**	**Reference**
ALD	TiO_2	Si(100)	Depth: 7.5 μm Aspect ratio: 1:40	Jõgi et al. (2008)
ALD	Ta_2O_5	Si(100)	0.17x0.30x0.73 μm^3 Aspect ratio: >35	Hausmann et al. (2003)
ALD	TiN	Si(100)	Aspect ratio: 10:1	Kim et al. (2003)
MOCVD	Ta_2O_5	Si	Depth: 1 μm Width: 0.7-1.25 μm	Yun and Rhee (1997)
MOCVD	Al_2O_3	$Al/Al_2O_3/Si$	Aspect ratio: ≤60	Wiest et al. (2006)
MOCVD	$Pb(Zr,Ti)O_3$	$SiO_2/TiAl/Ti/SiO_2/Si$		Funakubo et al. (2007)
LPMOCVD	YSZ	Si	Depth: 3-9 μm Width: 1-3 μm	Akiyama et al. (2002)
CVD	Diamond	Si(100)		Monteiro et al. (2003)
APCVD	SiO_2	Ti/Al/TiN	Al spacing: 0.2 μm Aspect ratio: 3:1	Yuan et al. (1996)
PP-MOCVD	TiO_2	Si(100)	Depth: 1 and 4.6 μm Width: 1-500 μm	Siriwongrungson et al. (2007)

Conformal coating and the phase of TiO_2 on silicon-patterned substrates were investigated by Jõgi et al. using ALD. The temperatures were in the range of 125 to 500°C. The patterns were 7.5 μm in depth with the aspect ratio of approximately 1:40 (Joegi et al., 2008). Absolute conformal step coverage of tantalum (V) oxide (Ta_2O_5) on vias with an aspect ratio greater than 35 was achieved by Hausmann et al. using ALD at deposition temperatures from 50 to 350°C under the pressure inside the reaction chamber of 13.33 Pa. Tantalum alkylamide was used as the precursor while water was used as the oxygen source (Hausmann et al., 2003). With the same deposition method, conformal thin titanium nitride (TiN) films were deposited by Kim et al. on trenches with the aspect ratio 10:1 and substrate temperatures were in the range of 375 to 500°C under pressures from 66.64 to 266.56 Pa (Kim et al., 2003).

Using MOCVD, Yun and Rhee studied the effect of substrate temperature and type of carrier gas on the deposition of Ta_2O_5 on Si substrate using experiment and simulation. The deposition temperatures were in the range of 350 to 440°C with 50 sccm of helium or argon as the carrier gas under the reactor pressure of 66.6 Pa (Yun and Rhee, 1997). Step coverage of over 90% for aluminium oxide (Al_2O_3) on Si trenches was achieved with an aspect ratio up to 60 by Wiest et al. using MOCVD at temperatures below 400°C and a pressure of 100 Pa (Wiest et al., 2006). Funakubo et al. used MOCVD to investigate the effects of source materials, in this case zirconium and titanium, on the conformality of

film thickness and compositions in trenches. Trench substrates were SiO_2/TiAl/Ti/SiO_2/Si (Funakubo et al., 2007).

LPMOCVD was applied by Akiyama et al. for the experimenting and modelling of YSZ growth and composition distribution on Si trench substrates. The trenches were micro-size with a depth between 3 to 9 μm and a width of 1 to 3 μm. The deposition temperatures were in the range of 500 to 750°C (Akiyama et al., 2002). The growth of CVD diamond films on patterned substrates using a microwave plasma-assisted deposition reactor was investigated by Monteiro et al. The study focused on the enhancement of nucleation on horizontal and vertical walls and the promotion of narrow trench filling using seed layers (Monteiro and Liu, 2003). The deposition of silicon dioxide (SiO_2) conformality as functions of ozone concentration and deposition temperature using APCVD was investigated by Yuan et al. The precursor was tetraethoxysilane or tetraethylorthosilicate (TEOS) in the presence of ozone under low temperature (Zheng et al., 1996).

Using PP-MOCVD, it was reported that conformal step coverage of over 0.80 was achieved. The deposition temperatures were in the range of 400 to 600°C with Si as the trench substrate. The trenches were 1 and 4.6 μm deep with 1 to 500 μm wide (Siriwongrungson et al., 2007).

Measurements of Conformality

The measurements of conformality varied from study to study. In general, the thicknesses were measured at the top, middle and bottom of the trench to determine the conformality of the deposited film (Hausmann et al., 2003; Joegi et al., 2008; Kim et al., 2003). Figure 2-22 illustrates the schematic diagram of a deposited film on a trench with step coverage measurement parameter definitions.

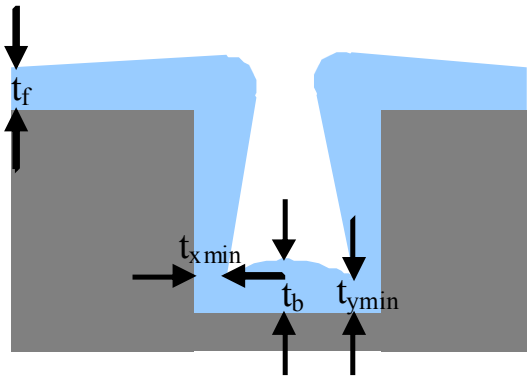

Figure 2-22: The thickness parameter measurements at each point on a deposited film. t_f is the thickness at the top of a trench. t_b is the thickness in the middle of the trench. t_{xmin} is the minimum thickness in the x-axis of a trench. t_{ymin} is the minimum thickness in the y-axis of a trench (Hong et al., 1997).

Yun and Rhee defined the step coverage as the ratio of the thickness of the deposited film at the centre point of the trench bottom to the top of the trench (t_b/t_f) (Yun and Rhee, 1997). A similar step coverage definition was applied to the study of Wiest et al. and Al-Mohssen et al. Wiest et al. defined the step coverage as the ratio of thickness in per cent between the thickness at the bottom to the top of the trench (t_b/t_f), the thickness at the middle to the top of the trench and the thickness at the bottom to the middle of the trench (Wiest et al., 2006). Al-Mohssen simulated the step coverage using Direct Simulation

Monte Carlo (DSMC) of a CVD system by defining the step coverage as the ratio of the thickness of a deposited film at the location of interest to the thickness of the deposited film on the flat surface area as far as possible from the trench (Al-Mohssen and Hadjiconstantinou, 2004). Hong et al. used the DSMC to study the uniformity and sticking coefficient of an uneven surface on a CVD system. This group defined the uniformity as t_b/t_f, t_{xmin}/t_f and t_{ymin}/t_f in order to represent the step coverage at vulnerable spots (Hong et al., 1997). In the present study of PP-MOCVD conformality, the dimensionless conformality as written as Equation (3-3) in section 3.3.4 was applied (Siriwongrungson et al., 2007).

2.5. Precursor Chemistry

The precursor is one of the most important components of making good films and powders by CVD. The chemicals that are used as a precursor usually have the following properties. They are stable and able to generate a stable vapour phase at room temperature for storing and transferring purposes. They have high vapour pressure and sufficient volatility at low temperatures to avoid condensation problems in the line before entering the reactor. They can undergo chemical reaction or decomposition at a temperature below the melting temperature and phase transformation of the substrate to avoid substrate properties change. They have a suitable deposition rate, for example, low for thin film applications and high for thick coating applications and are able to react without producing side or parasitic reactions. They are cost-effective and with good conversion efficiency for thin film and coating

deposition. In order to minimise contamination of the deposited film, the chemicals are able to react with minimum carbon incorporation in the reaction zone and are capable of producing films with a very high degree of purity. The chemicals used as precursors should have low toxicity and explosiveness and be nonflammable for safety purposes(Choy, 2003; Pierson, 2006).

2.5.1. Types of Precursor for MOCVD

There are many types of precursors based on metal groups and chemical groups. MOCVD precursors can be categorised such as alkoxide, alkyl compounds and β-diketonates for the ligands attached to the metal (Jones and Hitchman, 2009; Pierson, 2006). Table 2-4 shows the characteristics of the MOCVD precursors and their examples according to their precursor type.

Table 2-4: Types of precursor and examples (Condorelli et al., 2007; Jones and Hitchman, 2009; Pierson, 2006).

Type of Precursor	**Precursor Characteristics**	**Examples**
Alkoxide	Composed of alkoxide and a metal element: $[M(OR)_x]_n$ where M is the metal element and n is the degree of saturation	$Ti(OC_2H_5)_4$, $Al(OC_3H_7)_3$, $Cr(C_5H_7O_2)_3$, $Zr(C_{11}H_{19}O_2)_3$
Alkyl compound	Composed of a group IV metal and an aliphatic hydrocarbon or alkyl halide: MR_4	$(C_2H_5)_2Te$, $(CH_3)_2Zn$, $(CH_3)_3Sb$,$(C_2H_5)_3In$, $(CH_3)_3Al$
β-diketonate	Composed of β-diketonate and a metal element: $M(RCOCHCOR)_x$	$Sr(thd)_2$, $[Sr(thd)_2]_3$, $[Ba(thd)_2]_4$

Alkoxide

Alkoxide is composed of alkoxide [RO^-] and a metal element. It can be written as $[M(OR)_x]_n$, where M is the metal atom and n is the degree of saturation. The degree of saturation influences the volatility of the alkoxide. Metal alkoxides usually have low thermal stability; hence they can be used to deposit oxide films at low deposition temperatures. The thermal stability of an alkoxide is determined by hydrogen on the second carbon from the coordinated oxygen. This hydrogen is commonly known as a β-hydrogen (Jones and Hitchman, 2009).

Alkyl Compound

Alkyls are nonpolar volatile liquids. The alkyl group precursors are formed using a group IV metal with an aliphatic hydrocarbon or alkyl halide such as methyl, ethyl, isopropyl and butyl. The alkyl compounds could be written as MR_4. Alkyl compounds usually have very poor thermal stability as they lack of β-hydrogen.

β-Diketonate

Metal β-diketonate can be written as $M(RCOCHCOR)_x$ where M is the metal atom and R is the alkyl, aryl, etc. The group II metal β-diketonate is widely used as a MOCVD precursor because of its high thermal volatility, thermal stability, chemical stability and mass transport properties (Condorelli et al., 2007). The first generation of β-diketonate was based on 2,2,6,6-tetramethyl-3,5-heptanedione, $M(thd)_n$ (Jones and Hitchman, 2009). The group II β-diketonate complexes can be oligomeric or polymeric, $[M(thd)_2)]_x$, to lower

volatility to overcome side decompositions of these precursors. The second generation of β-diketonate which is widely investigated is based on 1,1,1,5,5,5-hexafluoro-2,4-pentanedione which is the combination of fluorinated β-diketonate arrays and ancillary coordinated polyether (Condorelli et al., 2007).

2.5.2. Precursors for TiO_2 Film Deposition

The most commonly used precursors for TiO_2 film deposition are titanium halides and titanium alkoxides. In general, halide based precursors favour the growth of the crystalline phase and lead to halide ion residue contamination. Alkoxide based precursors enable amorphous growth with carbon residues. The titanium halides are, for example, titanium tetrachloride ($TiCl_4$), titanium trichloride ($TiCl_3$) and titanium tetraiodide (TiI_4). Titanium alkoxides include ethoxide, propoxide and tetraisopropoxide (Hitchman and Alexandrov, 2001). Among them, titanium tetraisopropoxide (TTIP) is one of the most commonly used, and it is the liquid precursor used throughout this study.

2.5.3. Titanium Tetraisopropoxide

Titanium tetraisopropoxide, TTIP, has been chosen as a precursor in this study because it does not need an additional oxygen atom to produce stoichiometric TiO_2 by thermal decomposition, and it meets the ideal chemical characteristics for a metalorganic precursor (Fictorie et al., 1994). The TTIP chemical nomenclature found in literature includes isopropyl titanate, titanium (IV) isopropoxide, tetratitanium (IV) isopropoxide, tetrakis (isopropoxo) titanium (IV) and tetraisopropoxide titanium (TPT) (Krumdieck, 1999) TTIP has the

chemical formula $Ti(OC_3H_7)_4$ or $Ti(OPri)_4$ and has the chemical bonding as illustrated in Figure 2-23 (Palma and Alavi, 2005).

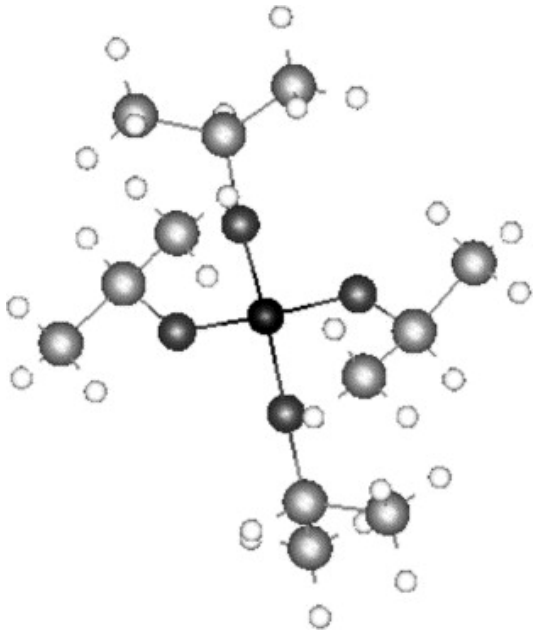

Figure 2-23: Chemical structure of TTIP. The black ball is Ti central atom; dark grey balls are oxygen atoms; grey balls are carbon atoms; white balls are hydrogen atoms. (Reprinted from Computational Materials Science, Palma et al., An ab initio study of titanium tera-iso-propoxide (TTIP) adsorption mechanism on a Si (100) surface, pp 244–249, 2005 with permission from Elsevier.)

TTIP can decompose and make TiO_2 films at a low substrate temperature. It has an unsaturated four-coordinate Ti(IV) in the centre that makes it quickly hydrolysed in air (Clark et al., 1975; Jones and Hitchman, 2009). The moisture in the atmosphere induces the decomposition that will propagate throughout the entire precursor volume once started. In addition, TTIP is flammable and corrosive, therefore the storage, handling and transfer of TTIP especially in solution-based liquid injection MOCVD are difficult and challenging and should be carried out with care. Table 2-5 shows certain values of TTIP and toluene physical properties.

Table 2-5: Physical properties of TTIP and toluene (Aesar, 1998; Krumdieck, 1999).

Physical Properties	**TTIP**	**Toluene**
Molecular weight [g·gmole^{-1}]	284.26	92.14
Density [g·cm^{-3}]	0.955	0.865
Boiling point [°C]	232	111
Melting point [°C]	20	
Vapour pressure at 25°C [Pa]	20.71	5300
Molecular volume [m^3]	4.94x10^{-28}	1.76x10^{-28}
Molecular area [m^2]	6.25x10^{-19}	1.46x10^{-19}
Surface tension [N·m^{-1}]		2.74x10^{-2}

2.5.4. Chemical Reactions of TiO_2 from TTIP

Three main reactions for the deposition of thin TiO_2 film from TTIP have been reported so far (Fictorie et al., 1994). These are heterogeneous reactions (a) and (b), intermediate reaction (c) and homogeneous reaction (d).

(a) $Ti(OC_3H_7)_4(g) \rightarrow TTIP(ad) \rightarrow TiO_2(s) + 4C_3H_6 + 2H_2O$

(b) $Ti(OC_3H_7)_4(g) \rightarrow TTIP(ad) \rightarrow TiO_2(s) + 2C_3H_6 + 2HOC_3H_7$

(c) $Ti(OC_3H_7)_4(g) \rightarrow TiO_2(g) \rightarrow TiO_2(s)$

(d) $Ti(OC_3H_7)_4(g) \rightarrow TiO_2(p) \rightarrow TiO_2(s)$

where (g) is gas, (ad) is adsorbed, (s) is solid and (p) is particle.

There are reactions other than these three principal reactions. The homogeneous reaction generally occurs at a high deposition temperature of at least 500°C. The chemical reactions (a) and (b) are for the deposition temperature in the range of 400 to 700°C. At a deposition temperature in the

range of 200 to 350°C, which is a heterogeneous reaction (b), the products are propene and isoproponol. For the higher deposition temperature, heterogeneous reaction (a), the products are propene and water (Fictorie et al., 1994). The homogeneous reaction is preferred when fine powder is expected, whereas the combination of homogeneous and heterogeneous is favoured for the formation of films (Choy, 2003).

Several researchers have investigated the activation energy, E_a, of the thermal decomposition reaction for TTIP under a range of composition conditions. The activation energy for TTIP varied from 20 to 150 $kJ \cdot mole^{-1}$ depending on the deposition conditions. Fictorie et al. reported the heterogeneous thermal decomposition of TTIP of 57±8 $kJ \cdot mole^{-1}$ by using the production of isoproponol to calculate the rate of the decomposition reaction (Fictorie et al., 1994). Chen and Dirking found the activation energy of 87 to 115 $kJ \cdot mole^{-1}$ using horizontal cold wall LPCVD (Chen and Derking, 1993). Giovanni et al. stated the activation energy of 20 $kJ \cdot mole^{-1}$ using an AP-MOCVD with nitrogen as the carrier gas (Battiston et al., 1999). As can be seen, the activation energy in the broad range depends on deposition conditions.

2.5.5. The Studies of TiO_2 Film Deposition From TTIP

Many studies show successful TiO_2 deposition from TTIP. The following are some examples. An anatase phase of uniform thin films was deposited on Si (111) wafers by Chen and Dirking in a horizontal cold wall LPCVD reactor at deposition temperatures between 325 and 400°C under precursor partial pressure of 0.22 Pa (Chen and Derking, 1993). Thick crystalline films and

nanocrystalline particles were prepared by Seifried et al. using a modified CVD method called chemical vapour synthesis (CVS) in a hot wall reactor at temperatures varying from 400 to 1200°C under total pressure of 2000 Pa (Seifried et al., 2000). Properties such as structure, growth rate, grain size and phase of thin films on indium phosphide (InP) substrate were studied by Lee et al. in a horizontal cold wall MOCVD reactor at temperatures in the range of 300 to 550°C under reactor pressure of $1.33x10^3$ Pa (Lee et al., 2001). Anatase to rutile phase transition of thin films on Si (100) was investigated by Byun et al. using an MOCVD reactor at deposition temperatures in the range of 250 to 550°C under a deposition pressure of $1.33x10^2$ Pa (Byun et al., 1997). With the same substrate and deposition method, growth rate of thin films was examined by Kang et al. at deposition temperatures between 300 and 700°C under a reactor base pressure of $1.33x10^5$ Pa (Kang et al., 2000).

The morphology and composition of thin films on Si (100) were investigated by Babelon et al. in a horizontal AP-MOCVD at growth temperatures in the range of 400 to 750°C (Babelon et al., 1998). The thin TiO_2 films of a few nanometers in thickness were deposited on Si (100) by Brevet et al. using an MOCVD reactor. The study investigated the initial stages of the TiO_2 thin films deposition by MOCVD at a temperature of 650°C under a reactor pressure of $2.93x10^2$ and 5.07 Pa (Brevet et al., 2005).

Table 2-6: Summary of the studies of TiO_2 film deposition from TTIP

Deposition Method	Temperature [°C]	Pressure [x10^3 Pa]	Substrate	Reference
LPMOCVD	400-800	0.67-2.67	Sapphire	Chang et al. (1992)
LPCVD	325-400	1.50	Si (111)	Chen and Dirking (1993)
CVD	700-900	$1.33x10^{-10}$-$1.33x10^{-6}$	Single crystal TiO_2	Fictorie et al. (1994)
MOCVD	250-550	0.13	Si(100)	Byun et al. (1997)
AP-MOCVD	400-750	101.32	Si(100)	Babelon et al. (1998)
CVS	400-1200	2.00	Si(100)	Seifried et al. (2000)
MOCVD	300-700	133	Si(100)	Kang et al. (2000)
MOCVD	300-550	1.33	InP	Lee et al. (2001)
MOCVD	650	0.005-0.29	Si(100)	Brevet et al. (2005)

The structural properties of epitaxial films on sapphire were studied at temperatures in the range of 400 to 800°C by Chang et al. using LPMOCVD under a reactor pressure of $6.67x10^2$ to $2.67x10^3$ Pa (Chang et al., 1992). Fictorie et al. studied the kinetic and mechanism of thin TiO_2 film deposition by CVD (Fictorie et al., 1994). The temperature was in the range of 700 to 900°C and the base pressure of the chamber was $1.33x10^{-7}$ Pa. The CVD

reactor in this study could be operated as high as $1.33x10^{-3}$ Pa. Table 2-6 summarises the researches related to TiO_2 film deposition from TTIP.

2.5.6. Precursor Solvents

Metalorganic precursors are commonly dissolved in relatively inert solvent such as tetrahydrofuran or a hydrocarbon. Hydrocarbons used as metalorganic solvents include toluene, heptane and nonane (Jones and Hitchman, 2009). Toluene has been chosen as the precursor solvent in this study. Toluene has the chemical formula C_7H_8 or $C_6H_5CH_3$ with the chemical bonding as illustrated in Figure 2-24.

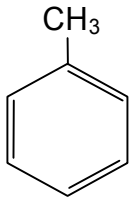

Figure 2-24: Chemical structure of toluene

Toluene can be used as a common solvent, an octane booster in gasoline, a carbon source for multi-wall carbon nanotube manufacture and a reactant for the production of chemicals. Toluene is used as a solvent in this study because it has sufficient vapour pressure and can dissolve the TTIP. A material safety data sheet (MSDS) is required for safety and prevention of hazards before dealing with solvents. Toluene is flammable and toxic by inhalation, ingestion or contact with eyes or skin. It can cause severe irritation and damage to liver, kidneys, bladder and brain tissues.

2.6. Titanium Dioxide Thin Films

Titanium dioxide (TiO_2) is a ceramic material. It has many other names such as titania, titanic acid anhydride, titanic anhydride, titanic oxide, titanium (IV) oxide and titanium white. There are three well-known bulk crystalline phases: rutile, anatase and brookite with rutile and anatase being the commonly found phases. The phase depends on the deposition temperature and pressure as well as post-deposition treatment. Rutile is found to be more stable at high temperatures while anatase is more stable at high pressure (Zhang et al., 2006). It has been observed that rutile is the only thermodynamically stable phase while the anatase phase is metastable (Seifried et al., 2000). Brookite was found at high deposition temperature and high pressure (Bernardi et al., 2001). TiO_2 has a different crystal structure and properties for different phases. The crystal structure of rutile and anatase are illustrated in Figure 2-25 (Ma et al., 2007).

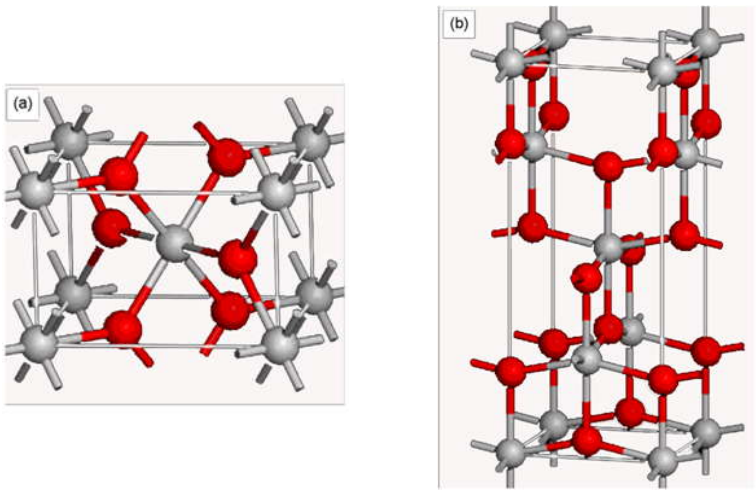

Figure 2-25: Crystal structure of (a) rutile and (b) anatase phase. Grey atoms represent titanium atoms and red atoms represent oxygen atoms. (Reprinted from Applied Surface Science, Ma et. al., Raman study of phase transformation of TiO_2 rutile single crystal irradiated by infrared femtosecond laser, pp7497–7500, 2007 with permission from Elsevier.)

In general, TiO_2 is composed of a Ti atom that is surrounded by six oxygen atoms; hence so-called TiO_6 octahedron. The TiO_6 octahedron is interconnected in a different way that leads to dissimilar structures and symmetries of each phase. The crystal structure of rutile and anatase phase is tetragonal but they can be differentiated using a space group. The crystal structure of brookite is orthorhombic. The space group describes the symmetry that is inherent in the crystal structure. The tetragonal space group of rutile, anatase and brookite are $P4_2/mnm$, $I4_1/amd$, and Pbca, respectively. Table 2-7 shows the lattice parameters of TiO_2 rutile, anatase and brookite phases.

Table 2-7: The lattice parameters of TiO_2 at various phases (Liu and Wang, 2002).

Phase	**a [nm]**	**b [nm]**	**c [nm]**
Rutile	0.4594		0.2958
Anatase	0.3785		0.9514
Brookite	0.9184	0.5447	0.5145

Table 2-8 illustrates the Raman shift related to its Raman active mode. The Raman active mode involves a change in polarisability of the molecules and only the Raman active mode can appear in Raman spectra. The polarisability is the ratio of dipole to the electric field, and it involves the displacement of charges when a molecule is in an electric field. In accordance with the crystal structure, there are four Raman active modes for rutile: $A_{1g}+B_{1g}+B_{2g}+E_g$, and six Raman active modes for anatase: $A_{1g}+2B_{1g}+3E_g$. It should be noted that the amorphous TiO_2 does not have any Raman active modes. According to Zhang et al., the strongest peak of the anatase phase is at Raman shift of 144 cm^{-1}

while 143 cm^{-1} is the lowest peak for the rutile phase. Different phases of TiO_2 have different properties and applications.

Table 2-8: Raman shift (cm^{-1}) of single crystal TiO_2 and their assignment from various references.

Phase	Assignment	Raman Shift (cm^{-1})		
		Ma et al. (Ma et al., 2007)	**Zhang et al. (Porto et al., 1967)**	**Musice et al. (Musice et al., 1997)**
Rutile	B_{1g}	140.2	143	
	Multi-photon scattering	235.5	235	
	E_g	445.8	447	
	A_{1g}	609.8	612	
	B_{2g}	825.5		
Anatase	E_g	140.9	144	
	E_g	196.3	197	
	B_{1g}	396.0	399	
	A_{1g}	515.4	515	
	B_{1g}	515.4	519	
	E_g	632.7	639	
Brookite	Strong			128
	Strong			153
	Medium			247
	Strong			636

Table 2-9: Physical properties of rutile and anatase phase TiO_2 (Bloor et al., 1994; Clark et al., 1975; Krumdieck, 1999).

Physical Properties	**Rutile**	**Anatase**
Crystal Structure	Tetragonal	Tetragonal
Molecular weight [g·gmole^{-1}]	79.90	79.90
Density [g·cm^{-3}]	4.26	3.84
Melting point [°C]	1855	-
Thermal expansion coefficient [°C^{-1}]	7.1x10^{-6}	7.1x10^{-6}
Thermal conductivity [W·m^{-1}·K^{-1}]	6.70	6.70
Dielectric Constant [1MHz]	85	85
Energy Band Gap [eV]	3.0	3.2
Refractive Index at 550 nm	2.75	2.54

Table 2-9 illustrates the physical properties of TiO_2 rutile and anatase phases. The following are examples of TiO_2 properties and applications. Both anatase and rutile phases have high refractive indexes of 2.54 and 2.7 respectively (Liu and Wang, 2002). TiO_2 has high dielectric constant, k varies from 86 to 170 for the rutile phase (Jones and Hitchman, 2009), that makes it suitable for high-k material uses in dynamic random access memories and bioelectronics (Joegi et al., 2008). This high refractive index and high dielectric property make TiO_2 suitable for optical and electronic applications. The optical transparency of TiO_2 is in the visible spectrum from 400 to 3000 nm. This makes TiO_2 a very promising photonic material for the multilayer coating of visible and near infrared (IR) range (Nami et al., 1997a). Rutile is denser and found at higher temperatures than the anatase phase. TiO_2 has a large band gap of 3.0 eV for

rutile and 3.2 eV for anatase phase (Kitazawa et al., 2006; Sankapal et al., 2005). The large band gap property is a requirement in semiconductor production, solar energy conversion and photocatalysis. The anatase phase is more suitable for photocatalysis application because of a higher band gap than rutile (Kitazawa et al., 2006). TiO_2 is used as a self-cleaning coating on glass because it has a very low surface affinity for organic molecules (Leistner et al., 2002). Because TiO_2 is chemically inert or chemically stable, it has been applied in corrosion resistance applications. TiO_2 is used as thermal barrier because it is a thermally stable property. Compared to SiO_2, TiO_2 has better thermodynamic stability that makes it an alternative for gate dielectric material in metal oxide semiconductor field effect transistors (MOSFETS) (Jones and Hitchman, 2009). Additionally, TiO_2 is biocompatible making it suitable for medical implant applications such as joint replacement (Leng, 2008). Combined with ferroelectric oxides, for example $SrTiO_3$, $(Ba,Sr)TiO_3$ and $Pb(Zr,Ti)O_3$, it has been used in infrared detectors and non-volatile computer memories (Jones and Hitchman, 2009). TiO_2 is used as a white pigment for paint, plastic, paper and cosmetic.

There are a number of ways to produce TiO_2 depending on whether it is thin film, thick film or powder. For TiO_2 thin films, the deposition could be carried out using APMOCVD or APCVD with the temperature in the range of 400 to 600°C (Neyts et al., 2007), LPCVD at a temperature between 325 and 400°C (Chen and Derking, 1993), sol-gel, hydrothermal synthesis dip-coating and spray-pyrolysis (Duminica et al., 2007). The phase of deposited TiO_2 and

impurities depends strongly on deposition temperature. The lower the deposition temperature the higher the content of residual impurities.

2.7. Substrate Materials

In this study, TiO_2 was deposited on Si and Si_3N_4, substrates. The physical properties and characteristics of Si and Si_3N_4 are reviewed. Table 2-10 summarises the physical properties of Si and Si_3N_4 measured at room temperature.

2.7.1. Silicon

Silicon, Si, is the one of the most abundant elements on earth; however, it is hardly ever found as a pure free element in nature and normally appears in the form of silicon dioxide, SiO_2, or silica and silicate. Nevertheless, it can be found in gold and volcanic exhalations. Silica is found in different forms such as sand, amethyst, agate, quartz, rock crystal, chalcedony, flint, jasper and opal. Silica appears in combination not only with silicon and oxygen but also with another metal. It is found for example in clay, sand and rocks such as granite and sandstone. Si has many known isotopes with its mass number ranging from 22 to 24. ^{28}Si is the most commonly found while ^{30}Si is a stable isotope. ^{32}Si is a radioactive isotope, with approximately 170 years half-life, generated from the decay of argon.

Silicon is an active element with halogens, dilute alkalis and acids such as hyperreactive combinations of nitric and hydrofluoric acid. It has a negative temperature coefficient of resistance; hence it maintains its semiconductor

properties at high temperature. Moreover, its native oxide can be easily grown in a furnace with higher semiconductor and dielectric interface improvement than other materials. With its properties, pure silicon is normally used for semiconductor, electronics and photovoltaic applications. In general, the electrical response of pure silicon can be adjusted by doping with other elements and controlling its charge of current carriers. This doped-Si is important for electronics and high technology applications such as transistor, solar cell, microprocessor, semiconductor detector, integrated circuit or microchip and many more. For large area applications such as LCDs and thin film solar cells, hydrogenated amorphous silicon is the solution for low-cost production. In automotive industries, metallurgical grade silicon is used in aluminium silicon alloys for parts-casting production. The compound of silicon and oxygen and silicon and carbon, generally known as silicone, provides polymer-like properties. These properties include flexibility and chemical as well as water resistance; hence it is used as waterproof material, a moulding compound, mould releasing agent, mechanical seal, high temperature grease and wax and an explosive. Silica, which is another commonly found form of silicon, is the principal component in the production of cement, pottery, enamels and glass, which includes windows, containers and insulators.

Table 2-10: Physical properties of single crystal Si and Si_3N_4 measured at room temperature unless otherwise stated (Bloor et al., 1994; Virginia Semiconductor, 2002).

Physical Properties	**Si**	**Si_3N_4**
Crystal Structure	Diamond	Hexagonal
Molecular weight [g·gmole^{-1}]	28.09	140.28
Density [g·cm^{-3}]	2.32	3.10
Melting point [°C]	1414	1900
Thermal expansion coefficient [°C^{-1}]	2.6x10^{-6}	3.4x10^{-6}
Thermal conductivity [W·m^{-1}·K^{-1}]	150	27
Dielectric Constant [1MHz]	11.7	9.4
Energy Band Gap [eV]	1.12	4.0
Refractive Index	3.42	2.10

2.7.2. Silicon Nitride

Silicon nitride, Si_3N_4, has three crystallographic structures: α, β and γ phases. The α and β phases are more common and can be produced under normal temperature conditions while the γ phase requires high-pressure and high-temperature manufacturing conditions. Silicon nitride is the second ceramic after silicon carbide, SiC, that has the strongest covalent bond. The natural existence of silicon nitride is restricted to meteorites, where it very rarely occurs as mineral nierite.

Silicon nitride has a high strength over a wide range of temperatures, superior thermal shock resistance, good chemical oxidation resistance, exceptional wear

resistance, good mechanical fatigue and creep resistance, high fracture toughness, an extremely smooth surface, high dielectric constant, radiation immunity and high optical transmittance. The properties of silicon nitride, such as band gap, depend on its Si to N ratio. The band gap of Si-rich film with Si to N ratio of about 0.91, increases from 2.05 eV to 5.1 eV compared with Si to N ratio of approximately 0.75. The pure Si-rich film improves radiation immunity properties as well. From its properties, silicon nitride has been applied to many applications including chemical plant parts such as heat exchangers and valves, engine components such as turbochargers, rotors, ball bearings and rollers, cam followers, and tappet shims, turbine blades and cutting tools. Other applications are, for example, an etch mask in bulk micromachining and a dielectric in capacitors in analog chips because of its electrical insulation property (Glocker and Shah, 1995).

CHAPTER 3

METHODS

This chapter explains the experimental work including the substrate and precursor preparation, apparatus and material analysis. The analysis calculations are summarised for an understanding of the results and discussions in the next chapter. The outline of the methods chapter is as follows:

3.1. Experimental Apparatus and Preparation Methods

3.2. Material Analysis Methods

3.3. Concentration, Deposited Film Properties and Growth Parameter Calculations

3.4. Experimental Design

3.1. Experimental Apparatus and Preparation Methods

This section explains how the substrate and precursor were prepared. The experimental apparatus is then described.

3.1.1. Substrates and Precursor Preparation

Three substrates were used for titanium dioxide (TiO_2) deposition, namely silicon (Si), silicon nitride (Si_3N_4) and quartz. Si was chosen as it is a well-known substrate used in many applications. Si_3N_4 is one of the mould materials employed for nanoimprint lithography. It is more suitable as a nanoimprint lithography mould than Si because the aspect ratio and mould durability are higher while the adhesion between the mould and imprint polymer is lower

(Alkaisi et al., 2001). Quartz was used to investigate the optical properties of deposited TiO_2, and it can be used for 3-D nanoimprint lithography UV moulds. In addition, those substrates have melting points and decomposition temperatures higher than the highest deposition substrate temperature of 600°C used in this study.

The Si substrates were cut to 10x10 mm^2 from 500 μm thick three-inch p-type Si(100) wafers. The Si wafer was single crystal with one side polished. Si_3N_4 was deposited on a similar Si wafer using the CVD technique to approximately 300 nm thick. The Si and Si_3N_4 wafers were supplied by Silicon Quest International. The features on the Si and Si_3N_4 coated Si were prepared by Khairudin Mohammed (Mohamed et al., 2006) from the Electrical and Computer Engineering Department at the University of Canterbury, Christchurch, New Zealand. The patterned substrates production and cleaning were carried out in the Nanofabrication Laboratory, which is a class 10k grade laboratory. The micro-scale features on Si substrates were gratings with different periods. The dimensions were varied from 1 to 500 μm wide and 1 μm deep. The nano-scale trenches were made on Si_3N_4 substrates. The aspect ratios for the features were 1:1 and 1.5:1 with dimensions between trenches of 100 and 500 nm.

The featured substrates were fabricated by first spin coating bi-layers of polymethyl methacrylate (PMMA) on cleaned substrates with resist thickness of approximately 50 to 250 nm. The resist was spun coated at 4000 rpm for one minute. PMMA is a positive photoresist with a glass transition temperature of

105°C (Konijin et al., 2005). It has poor sensitivity to UV and poor dry etch resistance with a small thermal expansion coefficient of $5x10^{-5}$ per °C and a low pressure shrinkage coefficient of $2.6x10^{-3}$ per Pa (Chou and Krauss, 1997). The first layer of PMMA was spun using 4% low molecular weight (LMW) PMMA. Then the substrate was hard baked for 30 min at a temperature of 185°C. It was cooled down to room temperature before the second layer was coated. The second layer of PMMA was spun using 2.5% high molecular weight (HMW) PMMA followed by hard baking under the same conditions as the first layer of PMMA. The pattern was written on to the bi-layers of PMMA resist by Raith 150 electron beam lithography (Götzberger et al., 2003) at 10 kV. The exposed pattern was then developed in a 3 to 1 solution of methyl isobutyl ketone and isopropyl alcohol (MIBK:IPA) at a temperature of 23°C for 30 sec. After that a 25 to 40 nm thickness of nichrome (NiCr) was deposited as a masking material using a metal evaporator. The lift-off process was carried out by soaking the patterned substrate in acetone for three hours. Reactive ion etching (RIE) using sulphur hexafluoride/oxygen (SF_6/O_2) was applied to dry etch the Si substrate anisotropically or to transfer the pattern. For the steep sidewall profile fabrication, a gas mixture recipe of trifluoromethane and argon (CHF_3/Ar) was used for Si_3N_4 substrates as an etching process at a temperature of -20°C under a pressure of 15 mTorr with a radio frequency (RF) power of 200 W for four minutes. The gas flow rate of CHF_3 was 30 sccm while argon was 25 sccm. The remaining NiCr layers were removed by soaking the patterned substrate in chrome etch solution for 30 sec.

Before the deposition of TiO_2 film, the substrates, either patterned or non-patterned, were cleaned using three solvents. Acetone was followed by methanol and IPA in an ultrasonic bath, each for five minutes. After that the substrates were dried in an oven set at a temperature of 95^{o}C for 30 minutes. The substrates were fastened on to the cleaned susceptor with edge clips in the reaction chamber of the PP-MOCVD system.

The precursor used throughout this study was 97% titanium (IV) isopropoxide supplied by Sigma-Aldrich with chemical abstracts service (CAS) number 546-68-9. Other names for TTIP are tetraisopropyl orthotitanate and TYZOR®organic titanate with the molecular formula $Ti(OCH(CH_3)_2)_4$. The precursor solvent, toluene, was also supplied by Sigma-Aldrich with CAS number 108-88-3. It was solvent grade with less than 99.3% laboratory reagent. The toluene was dried over calcium hydride (CaH_2) under an argon or nitrogen atmosphere using a distillation apparatus before mixing with TTIP.

Because TTIP is sensitive to moisture, the preparation of the precursor was made in a glove box under an argon or nitrogen atmosphere. The bottle was then capped with a polypropylene (PP) cap inaugurated with Swagelok before installation into the experimental system under pressurised argon. All the equipment was dried in a drying furnace and cooled under argon or nitrogen before use. The prepared precursor was stored away from light to reduce the chemical decomposition rate.

3.1.2. Apparatus

The PP-MOCVD system comprises four principal subsystems: the reactant supply system; the reactor system; the exhaust system and the control system. Figure 3-1 to Figure 3-3 illustrate certain apparatuses of the PP-MOCVD system applied in this study. The specifications of measurements and components are given below.

Push Gas Pressure Regulator

The push gas pressure regulator in this system was CIGWELD Comet 5000. It is rated for pressure up to 3000 kPa. The delivery pressure was set to approximately 50 to 70 kPa during the experiment.

Pressure Gauge

The bourdon tube pressure gauge from WIKA was installed and the full-scale value is 250 kPa. According to the datasheet of the bourdon tube pressure gauge from WIKA, the operating temperature is -40°C to 60°C with copper alloy as the main material for connections and the bourdon tube.

Glass Bottle

The solvent and precursor glass bottles were 250 ml SCHOTT DURAN that can stand the pressure in the range operated. The glass bottle comes with a polypropylene screw cap and ring. The cap was designed and modified to fit with an in-house stainless steel part for quick connect and tube fitting.

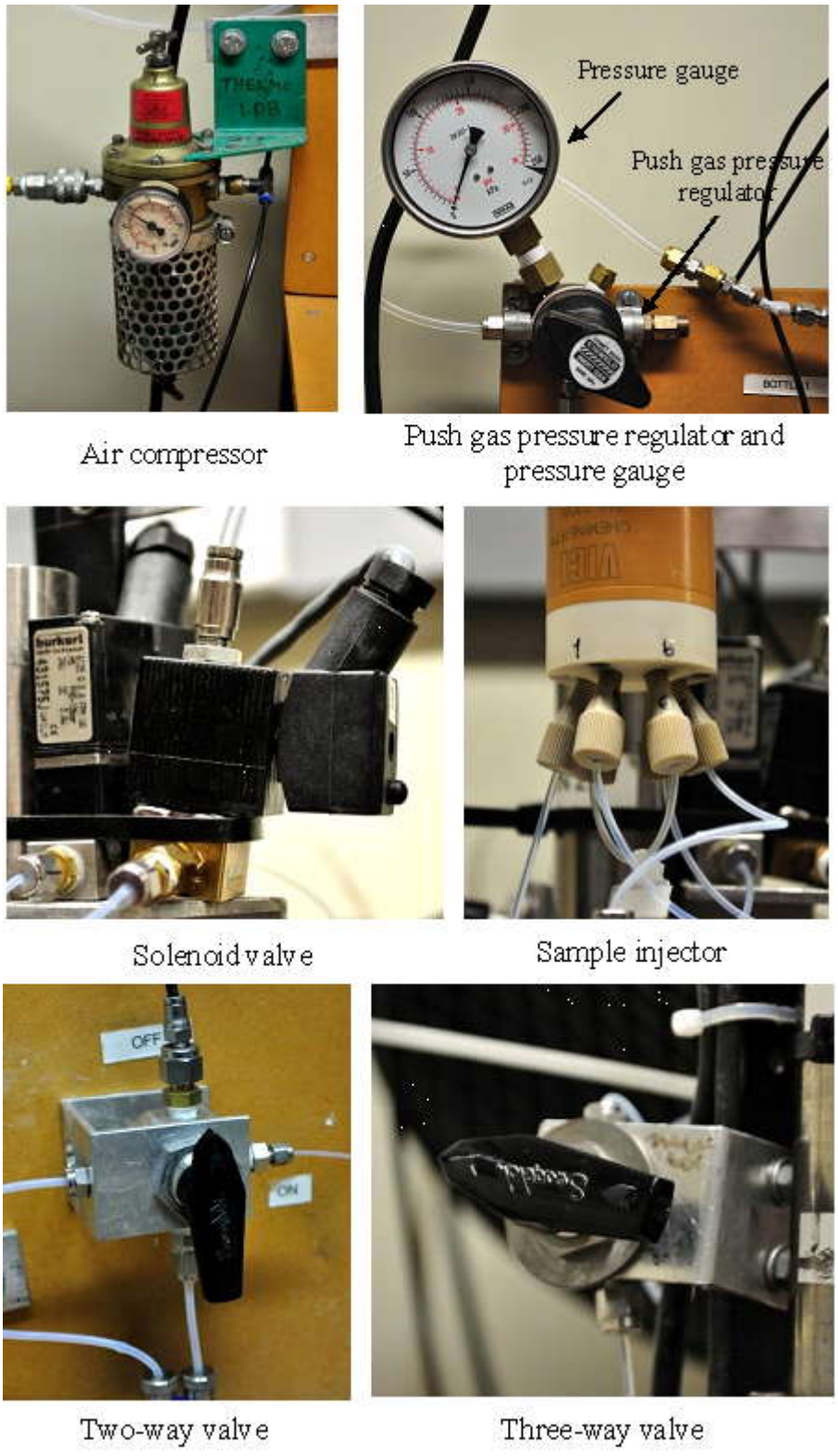

Figure 3-1: Apparatuses that were applied in the precursor supply system of PP-MOCVD in this study. From the top are the air compressor, push gas regulator and pressure gauge. In the middle are the solenoid valve and the sample injector. At the bottom are the two-way and three-way valves.

Sample Loop and Tubes

The sample loop and tubing were made from polytetrafluoroethene (PTFE) or Teflon®, which is the well-known trademark of DuPont. The sample loops were 1.5875 mm in outside diameter (OD), 0.762 mm in internal diameter (ID) with 50, 100 and 250 μl. The precursor supply line tubing had two sizes. One was 1.5875 mm OD, 0.762 mm ID and the other was 3.175 mm OD, 2.159 mm ID. The ferrules attached to the tubes were made from polyaryletherketones (PEEK). Both PTFE and PEEK have good chemical resistance. The sample loop and tubing were supplied by VICI.

Quick Connect and Tube Fitting

The quick connect and tube fitting were from SWAGELOK and were made from 316 stainless steel.

Mobile Phase Filter

The mobile phase filter was connected directly by simple press to the 3.175 mm OD PTFE tubing inside the precursor bottle. The mobile phase filter was supplied from Cheminert Fittings of VICI. The housing of the filter was made from PTFE with 2 micron titanium frit.

Two-Way and Three-Way Valves

The two-way and three-way valves were from SWAGELOK and were made from 316 stainless steel.

Sample Injector

A 6-port external sample injector from VICI was used as the sample injector. It can withstand low pressure and accepts 1.5875 mm VALCO zero dead volume (ZDV) fittings. The sample injector generally comes with VALCO ZDV PEEK nuts and ferrules and is controlled by an air actuator.

Air Compressor

The air compressor was used to produce compressed air to activate the air actuator. This was Model 73ACX from NORGREN. The pressure gauge of the air compressor was from WIKA which can read the pressure up to 600 kPa.

Solenoid Valve

The solenoid valve used to control the pulsing system was a 16 mm miniature rocker solenoid valve with an isolating diaphragm for technical application. The control valves were BURKERT 6125/6126 three-way and two-way two-position valve. Their bodies were made from stainless steel that can stand fluid temperatures from 0 to 50°C and an ambient temperature of 50°C. The operation pressure range was from 0 to 10.31 kPa. The solenoid valve was supplied with a 24 V/DC actuator with power consumption of 3.4 W. The response time of the valve is approximately 25 msec. The solenoid valve can tolerate a voltage of 10% and liquid contact surfaces of the solenoid valve are compatible with toluene.

Reactor Flange

In-house manufactured stainless steel flanges were used to ensure a vacuum was maintained inside the glass tube reactor. An ultrasonic nozzle was mounted on the top flange by a compressive O-ring seal. The bottom flange had three outlets, one of which was connected to a vacuum pump and air release valve, and another was attached to the thermocouples. The third was connected to the heater power supply and pressure gauge.

Reactor Glass Tube

The reactor was made from a PYREX glass cylinder with OD of 85 mm and 3.5 mm thick. The reactor was 350 mm high but the system was designed to suit cylinders with a maximum height of 450 mm. Two VITON O-rings were used at both ends of the glass cylinder together with fittings and screw flanges as a vacuum seal that maintained the low pressure inside the reactor. The vacuum seals were not exposed to high temperatures. The glass tube was heated near the substrate heater to the range of 40 to 55 °C.

Substrate Heater

Substrate heaters were made in-house from kanthal, which can withstand temperatures of up to 1200°C, and clay. The heater was placed inside a susceptor and can heat the susceptor up to approximately 700°C. It was then placed inside an in-house manufactured stainless steel holder mounted on three 10 mm OD, 45 mm high stainless steel poles. A molybdenum sheet was placed

around the holder to reduce heat loss from radiation. The heater was connected to a power supply using a ceramic connector block.

Susceptor

An in-house stainless steel 25.5 mm in diameter susceptor was placed on top of the heater. After the deposition of thin film, the susceptor was polished prior to each deposition process in order to remove the deposited thin film. Three substrates of 10x10 mm^2 can be placed on the susceptor for one run.

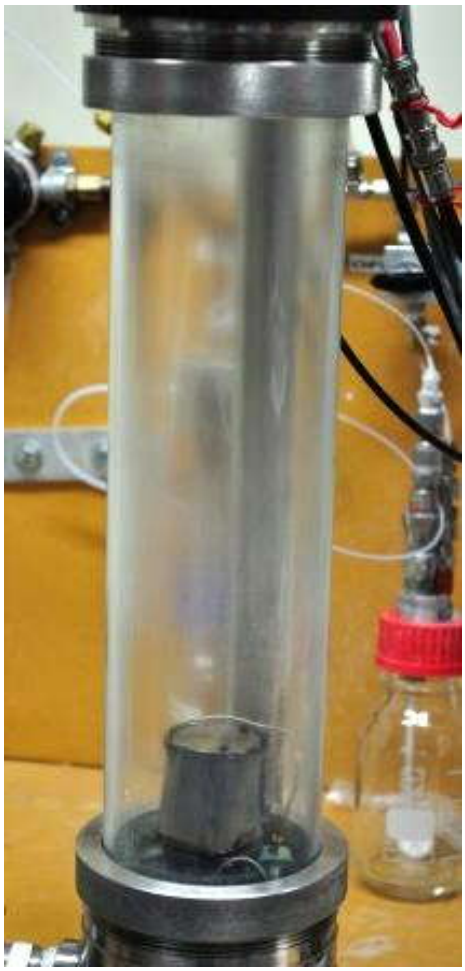

PP-MOCVD reactor

Ultrasonic nozzle

Substrate heater

Figure 3-2: The PP-MOCVD reactor glass tube and top and bottom flanges (left), the ultrasonic nozzle (top right) which was installed at the top flange and the in-house made substrate heater (bottom right).

Ultrasonic Nozzle

The ultrasonic nozzle used in this study was SONO-TEK 8700-120 cone shape micro spray. This model has an operating frequency of 120 kHz with a maximum flow rate of 0.4 gph and a median drop diameter of 18 μm as supplied by the manufacturer. The nozzle power was controlled by an ultrasonic nozzle generator from SONO-TEK. The maximum power input should not exceed 5.5 watts. The power of the nozzle controls the frequency, hence the droplet size of the precursor.

Thermocouple

Two type K (chromel-alumel) thermocouples were supplied from RS Components Ltd. They were used to measure the temperature on and inside the susceptor in contact with the heater. The thermocouples have accuracy between ±3.0 and ±4.5°C in the deposition temperature range. The temperature range for the probe is from 0 to 1100°C. These thermocouples are compatible with high vacuum operating conditions.

Temperature Measurement

The temperature measurement of the thermocouple on the susceptor was taken with a digital thermometer TX10 from YOKOGAWA Meters and Instruments. The temperature of the heater was measured through the control box. The accuracy of the digital thermometer is ±3.0 and ±4.5°C for the control box as supplied by the manufacturer.

Controlling Software

The Laboratory Virtual Instrumentation Engineering Workbench (LabVIEW) program was utilised to collect and store the data and control the system. The pressure data is stored in Excel file format, which is easy to interpret. The LabVIEW controlling screen is shown in. Figure 3-3.

Sample injection control

A VICI VALCO two-position air actuator was used to control the external sample injector. The standard air actuator can withstand a temperature of up to 70°C with typical pressure of 270 to 340 kPa. The response time is within 0.3 to 0.5 sec. The solenoid valves were controlled through a control box using the LabVIEW program to control the time and interval of opening and closing for each valve.

Vacuum Connection Valve

There were two valves in the exhaust system for this study. One was a butterfly valve that connected the reaction chamber and the vacuum pump. The other was a ball valve that linked the reactor to the atmosphere. Both valves were supplied by SWAGELOK.

Liquid Nitrogen Trap

The liquid nitrogen trap was a 20 mm ID internal glass tube and a 60 mm ID external glass tube. This trap was connected to the reaction chamber and a foreline filter before entering the vacuum pump using 25 mm ID PVC hose.

Vacuum pump

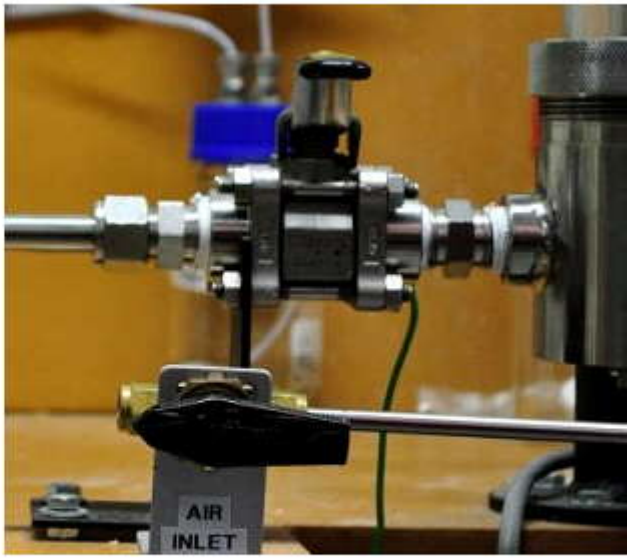

Vacuum connection valve

Control box

Liquid nitrogen trap

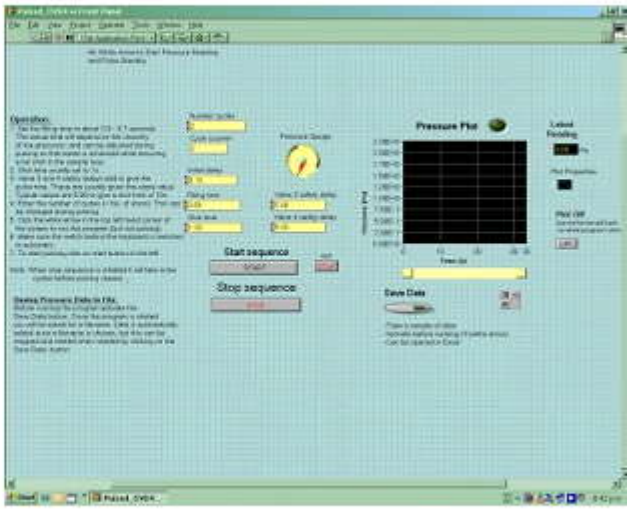

LabVIEW operation screen

Figure 3-3: Certain apparatuses in the exhaust and control system of PP-MOCVD in this study. On the left, a yellow jacket vacuum pump and a liquid nitrogen trap. On the right, butterfly and ball valves (top) connected to the vacuum pump and atmosphere, the control box (middle) that controls the solenoid valves and the LabView operation screen (bottom).

Vacuum Pump

A two-stage YELLOW JACKET Supervac Pump, 170 L/M 60 Hz and 142 L/M 50 Hz vacuum pump was used to maintain and provide the vacuum to the reactor system. The exhaust from the pump was connected by a 25 mm ID hose to a ventilation system. The pump characteristics are shown in Table 3-1.

Table 3-1: Vacuum pump characteristics

Motor	Single phase, 220V, 50Hz
Vaned pump stages	2
Nominal rotation speed	1500 rev·min^{-1}
Free air displacement	10 m^3·h^{-1}
Base pressure (without gas ballast)	<0.01 Pa
Power	0.37 kW

Exhaust System Conductance

Exhaust system conductance was calculated based on molecular flow (Roth, 1990). The length of the tubing, dimension of apertures, location of bents and conductance of the system calculation are in Appendix C. The conductance of the system, C_{sys}, was 0.56 l·s^{-1} with the vacuum pump speed at the reactor exit of 0.46 l·s^{-1}. The vacuum pump speed supplied by the manufacturer is 2.6 l·s^{-1}.

Reactor Pressure Data Reading

A MKS 317 convection-enhanced Pirani sensor was applied to obtain the pressure data. It was connected to the deposition chamber via a 5 cm stainless

steel tube of 0.5 cm in diameter. The pressure transducer can measure the pressure with a range of 0.133 Pa to 133 kPa. The time constant is less than 20 msec, which shows a good value of dynamic response and an accuracy of 0.25%. The transducer was connected to a MKS PDR-C-2C power supply and a digital pressure data display MKS 947 convection-enhanced pirani. The pressure data in the LabVIEW has been calibrated to agree with the reading on the MKS digital pressure display.

Heater Power and Temperature Control

Heater power and temperature were controlled using a POWERTECH MP 3090 power supply. The power supply was 15 V at approximately 6.5 A. The temperature was controlled manually by adjusting the power output from the power supply.

3.2. Material Analysis Methods

Deposited materials require analysis methods to identify material composition, structure and properties. Information on material analysis includes film morphology, phase, orientation and structure identification, composition and contamination quantification, defect detection, thickness, growth rate and grain size estimation. There are many techniques that can be applied to analyse thin films. Interferometer, ellipsometry, profilometry and ultrasonic multilayer-film metrology are used for thickness analysis. Film surface characteristics are analysed by scanning electron microscope (SEM), transmission electron microscopy (TEM), X-ray diffractometry (XRD), and atomic force microscopy

(AFM). Chemical characteristics are identified by energy dispersive X-ray spectroscopy (EDS), auger electron spectroscopy (AES), X-ray photoelectron spectroscopy (XPS), Rutherford backscattering (RBS) and secondary-ion mass spectrometry (SIMS). Analytical methods applied in this study are the colour shift method, scanning electron microscopy (SEM), energy dispersive X-ray spectroscopy (EDS), atomic force microscopy (AFM), X-ray diffraction (XRD), Raman spectroscopy and UV-Visible light spectroscopy.

3.2.1. Colour Shift Method

The colour shift method was used to estimate film thickness during the deposition process. It is not suitable to be used as the quantitative result because the observation of colour changes depends not only on the film thickness, but also on the observation angle or position. Calibration of thicknesses calculated from the colour shift method has to be carried out in every experiment using SEM.

The colour changes follow Bragg and Snell's law as the film grows. It changes from colour to colour with the next longest wavelength in the spectrum until the colours are no longer visible. The colour at that point is grey. Table 3-2 shows the thickness of TiO_2 estimated from colour changes. *j* represents the time at which green or red colour appears. The colour pattern at the initial stage of the film growth is yellow, purple, blue, clear, yellow, purple, blue, green, red, green, red and so on until grey.

Table 3-2: TiO_2 thickness estimation through colour changes at TiO_2 refractive index of 2.3 (Krumdieck, 1999).

j	Colour	Thickness [μm]
1	green	0.039
1	red	0.078
2	green	0.117
2	red	0.156
j	green	0.039(2*j*-1)
j	red	0.039(2*j*)

3.2.2. Scanning Electron Microscopy

Scanning electron microscopy (SEM) is applied to estimate the thickness and surface morphology of deposited films. The SEM used throughout this study was JEOL 7000 FE-SEM, which is a field emission SEM, as illustrated in Figure 3-4.

Figure 3-4: The JEOL 7000 FE-SEM used in this study.

To obtain high resolution images, a small probe diameter is preferred. This could be achieved by adjusting the operational variables which include probe current, working distance and acceleration voltage. The probe current should be small in order to obtain a small probe diameter. As the working distance is inversely dependent on the convergence angle, which is inversely dependent on the probe diameter, the working distance should be small in order to achieve a small probe diameter. The probe diameter directly varies with the wavelength of the electrons, which is inversely dependent on acceleration voltage; hence the larger the acceleration voltage the smaller the probe diameter. The depth of field can be achieved with the trade-off in the resolution. In general, the SEM is set at intermediate working distance and aperture size. Figure 3-5 illustrates the definition of the probe diameter, convergence angle, final aperture diameter, working distance and depth of field.

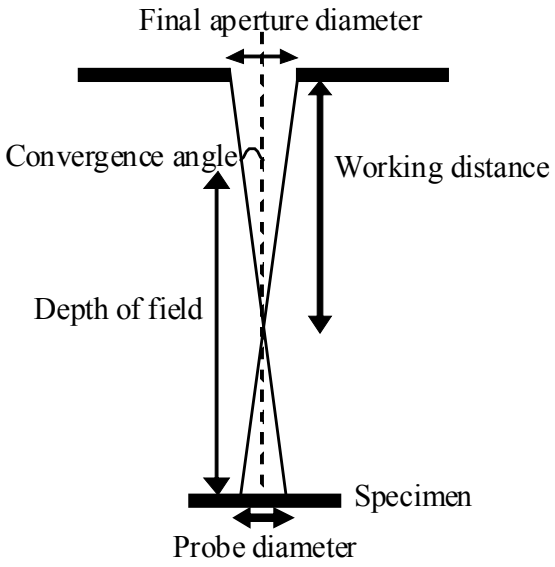

Figure 3-5: Definition of the probe diameter, convergence angle, final aperture diameter, working distance and depth of field.

Not only has the resolution of the image had to be considered but also the specimen. Suitable probe current and acceleration voltage depend on the deposited film and the substrate. The high probe current and acceleration voltage can be used when the substrate and deposited film are conductive. The high probe current gives a strong signal but decreases the resolution while the high acceleration voltage increases the resolution; hence balancing the probe current and acceleration voltage is important. Because the TiO_2 is not conductive, the probe current normally used is less than seven with operating voltages of 3 to 10 kV.

In general, a suitable specimen for SEM analysis should be conductive. In the case of non-conductive material or dielectric, conductive material coating is normally applied to optimise the electron scattering and enhance the contrast from SEM. The most commonly used material is carbon because it is cheap, almost invisible to most X-rays and has no effect on elemental analysis. The thickness of this layer is about 20 nm, or in certain circumstances 4 nm, in order for the layer not to interfere with the dimension of the surface features. The other materials that could be coated are gold, gold-palladium and platinum. One needs to be certain when coating these materials because they will distort the composition analysis. Gold was sputtered on certain deposited TiO_2 in this study for better image resolution.

3.2.3. Energy Dispersive X-ray Spectroscopy

Energy dispersive X-ray spectroscopy (EDS) was used to identify and quantify the composition in films. It was applied to qualitatively identify the

composition of deposited TiO_2 films in this study. An Oxford EXL EDS was used as it is a tool attached with JEOL 7000 FE-SEM. The probe current applied was normally 13 with an operating acceleration voltage of at least 10 kV in order to get enough counts for accurate results.

When a specimen is bombarded with high-energy electrons, the electron interaction volume is limited by energy loss through the elasticity of the electrons. The depth and volume of the electron penetration depend on the angle of incidence, probe current, acceleration voltage and average atomic number of the sample. Figure 3-6 illustrates the electron interaction volumes with various acceleration voltages and average atomic numbers.

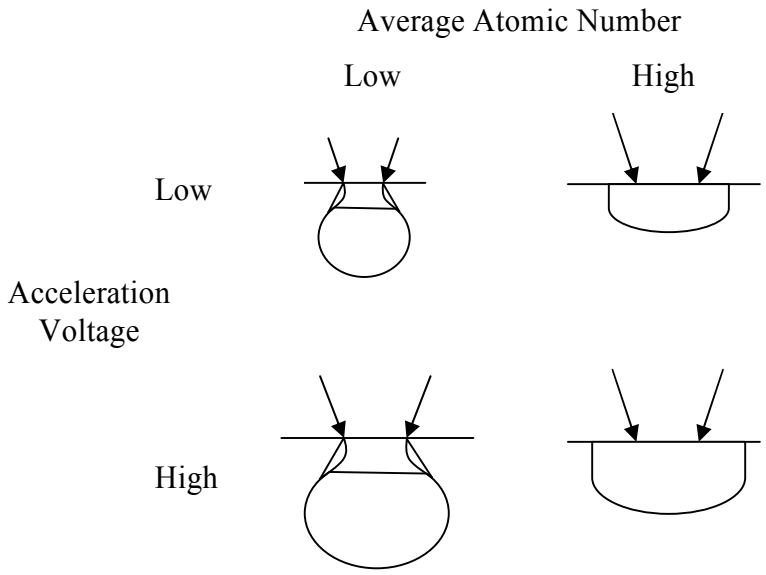

Figure 3-6: Variation of electron interaction volumes with average atomic numbers and acceleration voltages.

The signal detected in the EDS is from characteristic X-rays. In general, EDS uses a dispersive spectrometer to detect the quantum energy of the emitted X-ray. Since the electron beam could pass through thin films into the substrate,

distortion in quantification analysis could occur. In our samples, which have film thicknesses less than 500 nm, the qualitative composition has been identified with EDS. Nevertheless, EDS can be used to determine the relative quantities of elements and specify impurities in the deposited films.

3.2.4. Atomic Force Microscopy

Atomic force microscopy (AFM) is normally used to obtain three dimensional surface topography images and the image for sample characterisation. AFM was applied to identify grain size and surface roughness in this study. The AFM used was Digital Instruments dimension 3100 with Nanoscope IIIa software. The tapping mode with a commercial silicon NSC11 triangular cantilever was used. The tapping mode was chosen because it can provide high resolution on most samples. It uses lower forces; hence there is less damage to soft samples imaged in air. The offline operations of AFM applied were root mean square (RMS) roughness and grain size estimation with the measured area of 5x10 μm^2 and 1x1 μm^2. The RMS roughness is the standard deviation of the Z values in a given area. The built-in analysis formulas used were found in the manual from Scanning Probe Microscopy Training Notebook, Digital Instruments, Group Scientific Pty Ltd, Australia.

As the signal detected from AFM is the topography of a sample, it was used to quantify the surface roughness, grain size and height of a non-planar sample. AFM has high spatial resolution and can produce images of either conducting or insulating samples. The limitations of AFM include the artifact, which is induced by the tip geometry, the scan range that is limited to 100 microns

laterally and 6 microns in Z direction, and the problem might occur with samples that have considerable roughness and features smaller than the tip.

3.2.5. X-ray Diffraction

X-ray diffraction (XRD) is a non-destructive technique used to identify phase and crystal orientation and estimate the average crystallite size of thin films in this study. The XRD analysis was carried out at Industrial Research Limited (IRL) in Lower Hutt, New Zealand by Martin Ryan. The XRD at IRL is the Bruker D8 Advance, as illustrated in Figure 3-7, with θ-θ vertical goniometer and a long fine focus tube. Measurement conditions were Co K_α radiation 1.79 A° with α_1 1.78896 A° and α_2 1.79026 A°, tube voltage of 40 kV, tube current of 35 mA, 0.23 degree parallel plate collimator, using NaI(TI) scintillation counter, step scan mode with a step size of 0.05°, counting time 5 sec per step, and scan range from 25 to 60° 2θ at fix 0.5 to 1.3° incident angle.

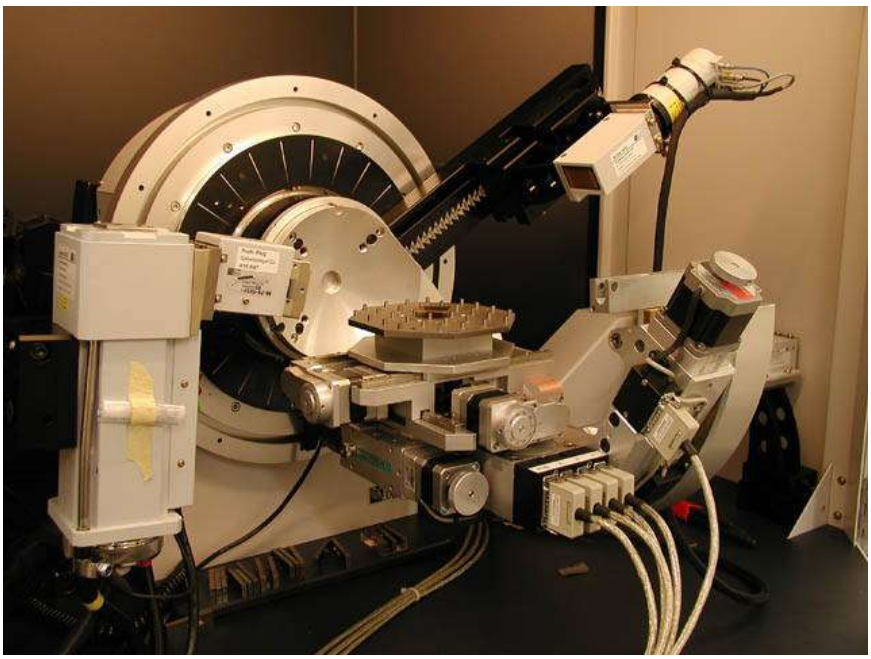

Figure 3-7: Bruker D8 Advance at IRL. Picture courtesy of M. Ryan.

XRD uses a single wavelength X-ray beam to characterise the crystalline materials. The incident X-ray beam is diffracted by the crystallographic plane of the materials. For thin film analysis, the diffraction intensity of a spectrum and diffraction angle (2θ) is recorded by rotating the detector. The parallel incident beam has a small incident angle, which is usually less than 1° and is fixed during the measurement. The scanning diffraction angle is not continuous but in steps. The step size influences the accuracy in peak location and intensity. Small step sizes result in peak shifts while the large step sizes result in suppression of peak intensity. The crystallite size of the materials affects the peak width which is inversely dependent on the crystallite size.

Crystalline phases of a material are identified by comparing the diffraction spectrum with the known crystalline spectrum database. X-ray diffraction data are recorded as a powder diffraction file (PDF).

3.2.6. Raman Spectroscopy

Raman spectroscopy was applied to identify the phase of deposited TiO_2 in this study. The spectrometer was TRIAX 320. The detector was a charge-coupled device (CCD). The SPECTROMAX was applied as operating software for the spectrometer and detector. This software was designed so that the input wavelength always hits the centre pixel of CCD; hence the display wavelength is calibrated and corrected. The argon laser at the excitation wavelength of 333.6 and 488 nm was applied. The entire wavelength recorded by the CCD required further calculation because the CCD and the spectrometer were controlled using separate systems. The manual calculation was carried out by

positioning the laser line on both ends of the CCD and recording the wave number difference using the spectrometer. The calculations at 333.6 and 488 nm were found to be 0.40 $cm^{-1} \cdot pixel^{-1}$ and 0.25 $cm^{-1} \cdot pixel^{-1}$, respectively.

The argon gas laser was used as the excitation source in this study. The excited laser beam was filtered by a pre-monochromator or a low band pass laser filter, which makes the laser a true monochromatic light source by filtering all the plasma lines.

This filter step is critical because the intensity of the plasma line is greater than the Raman spectrum. A holographic notch filter was used to minimise the excitation wavelength of the Rayleigh scattering, which has higher intensity than Raman, and to protect the sensitive detector. This filter results in a better signal to noise ratio and Raman intensity. The filtered light was collected and focused into the spectrometer. The scattered light was passed through a diffraction grating which disperses Raman scattered light according to its wavenumbers. The diffracted light was detected by a CCD which converted photon signals to electric signals. It is an effective array of 256x1024 individual detectors, each called a pixel. Each pixel records a single wavelength of diffracted light. The CCD is cooled by liquid nitrogen to maintain its sensitivity. The information from the CCD is processed and displayed.

3.2.7. Ultraviolet-Visible Light Spectroscopy

The ultraviolet-visible light spectroscopy was applied to measure the transmittance (%T) of the deposited TiO_2. The UV-VIS Spectroscopy used was Cary 14 PMT Recorder Spectrophotometer with an operating wavelength from 300 to 750 nm. The transmission and the absorption of the samples are measured as a function of wavelength.

The light from a source, normally an incandescent bulb for the visible wavelengths, or a deuterium arc lamp for the ultraviolet, or a flash lamp or a tunable laser, passes through a diffraction grating or monochromator before passing through the sample and reaching a detector at the end. There are two types of spectrometer: single beam and double beam. The single beam was used in this study. For a single beam spectrometer, all of the light will pass through the sample which must be removed to measure the light without the sample as a reference background. With a double beam spectrometer, the light is split into two beams. There is no need to remove the sample to measure the reference light intensity without the sample.

3.2.8. Contact Angle Measurement

Contact angle measurement was analysed to characterise the wettability of the deposited TiO_2 films. A small liquid droplet of 1 μl was placed on the surface using an immobilised syringe and allowed 10 sec for the liquid droplet to be stabilised. A light source was applied to illuminate the droplet for image observation. The images of the droplets were captured using a camera. The

ImageJ software with LB-ADSA plug-in was applied for contact angle measurements.

The contact angle is the angle between a tangent line of the surface of a liquid droplet and a solid surface at the interface. It is the angle at which a liquid and vapour interface meets the solid surface. The contact angle is determined from the interactions across the three interfaces, which are solid and liquid, solid and vapour, and liquid and vapour. The three forces and the contact angle are determined using the ideal Young's relationship (Frohn and Roth, 2000).

Figure 3-8 shows the wettability of a surface at various contact angles. The high contact angle of at least 90° shows a non-wetting surface while the low contact angle shows a good wetting surface. A contact angle of 180° means there is no adhesion between the solid and the liquid. A 0° contact angle results in a completely wet solid surface (Frohn and Roth, 2000).

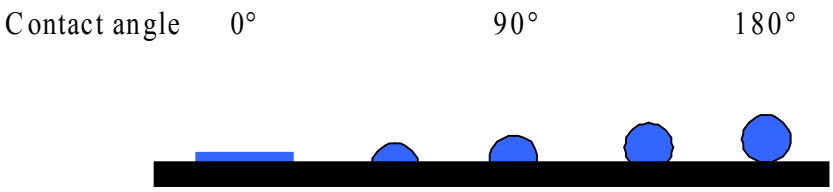

Figure 3-8: The droplet of a liquid at various contact angles.

3.3. Concentration, Deposited Film Properties and Growth Parameter Calculations

3.3.1. Concentration

The precursor concentration was calculated from the respective measured volumes of precursor and solvent

$$C_{mo} = \frac{\frac{v_{precursor} d_{precursor}}{Mw_{precursor}}}{\frac{v_{precursor} d_{precuror}}{Mw_{precursor}} + \frac{v_{solvent} d_{solvent}}{Mw_{solvent}}} x100 \qquad (3\text{-}1)$$

where C_{mo} is the precursor concentration (mol%); v is the volume of the precursor or solvent as subscripted (ml); d is the density of the precursor or solvent as subscripted ($g \cdot ml^{-1}$); Mw is the molecular weight of the precursor or solvent as subscripted ($g \cdot mol^{-1}$).

3.3.2. Growth Rate

The growth rate was generally calculated from the average film thickness observed from the SEM divided by the deposition time; hence the unit of the growth rate is in $nm \cdot min^{-1}$. In case of relaxation time variation, the growth rate was calculated from the average film thickness obtained from the SEM divided by the number of pulses instead of the deposition time. The unit of the growth rate in this case would be $nm \cdot pulse^{-1}$.

Figure 3-9 illustrates the thickness of TiO_2 measurement. The measurements were carried out on fractured surfaces using SEM. At least three sampling points were taken for non-structured and 15 for featured substrates.

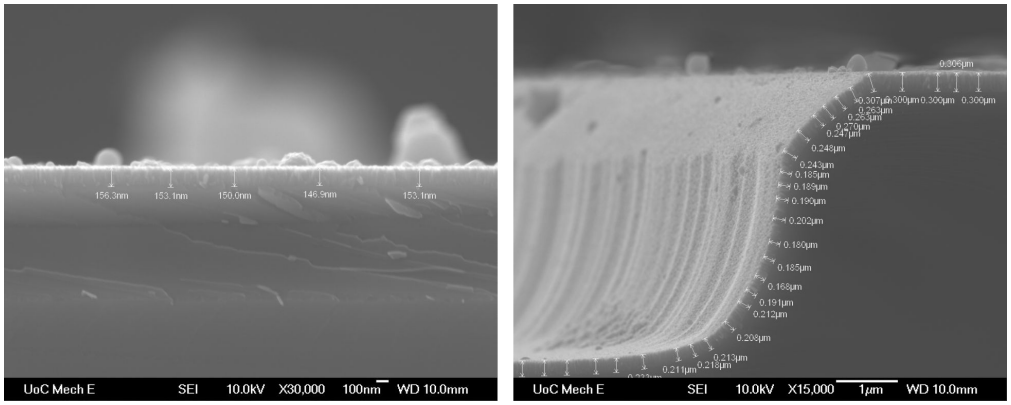

Figure 3-9: The thickness measurement of fractured surfaces of deposited TiO_2 on non-featured substrate (left) and featured substrate (right).

3.3.3. Crystal/Grain Size

Two methods were employed to estimate the grain size of deposited TiO_2 thin films. One involved simply using the atomic force microscopy (AFM) analysis tool. The other method used the Scherrer equation as written as Equation (3-2) (Koch et al., 2007).

$$D = \frac{0.9\lambda}{\beta \cos\theta} \qquad (3\text{-}2)$$

where D is the crystallite size (nm); λ is the wavelength of radiation (nm); β is the full width at half maximum (FWHM) value of a peak in a diffraction pattern (radians); θ is the angle of diffraction (radians).

According to Equation (3-2), the crystallite size is inversely related to FWHM. This implies that the wider the peak in the diffraction pattern, the smaller the crystal size with a low degree of periodicity. When the crystal has a high degree of periodicity, the peak will be tall and narrow because the incident beam is diffracted in the same angle independently of the layers of the material.

3.3.4. Conformality

The conformality calculation was adapted from the statistical method developed to measure relative mass transport uniformity by Krumdieck et al. (Krumdieck et al., 2005). A set of thickness measurements, δ_i, were taken over the area of interest along the cross-section of the film surface using the SEM image at 15,000x magnification. The film thickness was in nm with a thickness measurement error of ± 5 nm. The film conformality is given by Equation (3-3)

$$C = \frac{\sum_{i=1}^{M} \delta_i - \sum_{i=1}^{M} \left| \delta_i - \bar{\delta} \right|}{\sum_{i=1}^{M} \delta_i} \tag{3-3}$$

where C is dimensionless conformality; $\bar{\delta}$ is the average film thickness; M is the thickness sampling point index. As can be seen from the Equation (3-3), the maximum value of conformality is 1, which would represent a perfectly evenly coated film. The conformality calculated by this equation is dimensionless; hence one can compare the conformality of films independently of thicknesses.

3.3.5. Pulse Exposure and Total Molecular Flux

The total molecular flux and pulse exposure represent the rate of the precursor that arrives at the surface of the substrate. They depend on the number of precursor molecules that are injected into the reaction chamber and evaporated. The number of precursor molecules is controlled by the injection volume and the concentration of the precursor. The dimensionless total molecular flux is written as Equation (2-21).

$$J^* = \frac{J}{J_{\max}} = \frac{P^*}{P_{\max} t_p} \tag{2-21}$$

When the peak pressure is represented by the relationship of precursor vapour pressure, precursor concentration, precursor injection volume, reactor volume and base pressure, a dimensionless pulse parameter, pulse exposure, is calculated. The pulse exposure is as given as Equation (2-22).

$$PE = C_{mo} \frac{P_{\min}}{P_{vap}} \frac{\nu_L}{V_R} \frac{\tau}{t_p} \tag{2-22}$$

3.3.6. Refractive Index and Band Gap

The refractive index is calculated from a transmittance spectrum using the envelope method (Guemues et al., 2006), (Richards et al., 2004), (Caglar et al., 2006). The envelope method covers the minimum and maximum of the interference fringes in the thin film transmittance spectrum. Refractive index is estimated using Equations (3-4) and (3-5)

$$n = \sqrt{N + \sqrt{N^2 - n_s^2}} \tag{3-4}$$

$$N = \frac{(n_s^2 + 1)}{2} + 2n_s \frac{(T_{\max} - T_{\min})}{T_{\max} T_{\min}} \tag{3-5}$$

where n is the refractive index of the deposited film, n_s is the refractive index of the substrate, T_{max} and T_{min} are the maximum and minimum transmittances obtained at the same wavelength in the fitted envelope curves on the transmittance spectrum.

The energy band gap (E_g) is deduced from a plot of the square of the optical absorption coefficient, $(\alpha(hv))^2$, and the photon energy hv. The intercept of hv where $\alpha(hv)$ is equal to zero is the E_g. The relation of the curve is written as Equation (3-6) (Fox, 2001)

$$\alpha(hv) = K\sqrt{hv - E_g} \tag{3-6}$$

where K is a constant and α is the absorption coefficient. The optical absorption coefficient is determined from transmittance measurements as written as Equation (3-7)

$$\alpha = -\frac{1}{t}\ln(T) \tag{3-7}$$

where T is the normalised transmittance and t is the film thickness. When the envelope method is still valid, which means a weak absorption region, the normalised transmittance is calculated using Equation (3-8).

$$T = \frac{(n+1)(n-n_s)(\sqrt{\frac{T_{\max}}{T_{\min}}}-1)}{(n-1)(n-n_s)(\sqrt{\frac{T_{\max}}{T_{\min}}}+1)} \quad (3\text{-}8)$$

3.4. Experimental Design

The effect of processing parameters was investigated in order to characterise the effects of processing parameters on the conformality of thin films on featured substrates. The processing parameters were precursor concentration, injection volume, substrate deposition temperature, reactor base pressure and relaxation time. The characteristics were growth rate, conformality, surface roughness, grain size, surface morphology, phase and composition. Three different substrates investigated were Si, Si_3N_4 and quartz. The characteristic of each substrate influences film growth rate because of the substrate thickness and thermal resistance. Because Si and Si_3N_4 absorb the spectrum in the range of ultraviolet and visible light, quartz is useful for testing the optical properties of deposited TiO_2.

Table 3-3 shows the experimental range of processing parameters and principal processing variables.

Table 3-3: The variables used for PP-MOCVD conformality study experiments.

Parameter	**Experimental Value**
Injection Volume	50-250 µl
Precursor Concentration	0.15-0.50 mol%
Injection Time	1 sec
Reactor Volume	1.87 l
Peak Pressure	300-400 Pa
Base Pressure	100-200 Pa
Pulse Cycle Time	10-20 sec
Deposition Temperature	400-600 °C

The size of the nano-scale features was in the range of 100 to 300 nm with the aspect ratio of 1:1, 1.5:1. The size of the micro-scale structures varied from 1 to 500 µm wide and 1 deep. In this study, the aspect ratio of a trench means the ratio of substrate trench depth to the substrate width of the trench mouth. The experiments were categorised as shown in Table 3-4.

Table 3-4: Experimental conditions for the characterisation of conformality in this study.

Run Number	Temperature [°C]	Pressure [Pa]	Concentration [mol%]	Injection volume [µl]	Pulsing Time [s]
1	400	100	0.50	100	10
2	450	100	0.50	100	10
3	500	100	0.50	100	10
4	550	100	0.50	100	10
5	600	100	0.50	100	10
6	400	100	0.25	100	10
7	400	100	0.25	50	10
8	500	100	0.25	50	10
9	400	100	0.15	50	10
10	500	100	0.15	50	10
11	400	100	0.15	100	10
12	450	100	0.15	100	10
13	500	100	0.15	100	10
14	400	100	0.15	250	10
15	500	100	0.15	250	10
16	400	100	0.15	50	10
17	450	100	0.15	50	10
18	500	100	0.15	50	10
19	400	50	0.15	50	10
20	450	50	0.15	50	10
21	500	50	0.15	50	10
22	400	150	0.15	50	10
23	450	150	0.15	50	10
24	500	150	0.15	50	10
25	400	200	0.15	50	10
26	450	200	0.15	50	10
27	500	200	0.15	50	10
28	400	100	0.15	50	12.5
29	450	100	0.15	50	12.5
30	500	100	0.15	50	12.5
31	400	100	0.15	50	15
32	450	100	0.15	50	15
33	500	100	0.15	50	15
34	400	100	0.15	50	20
35	450	100	0.15	50	20
36	500	100	0.15	50	20

CHAPTER 4

RESULTS AND DISCUSSION

This chapter summarises and discusses the results obtained from the study. An understanding of the influences of the processing parameters on the films' growth and properties is necessary for the optimisation of a coating process on 3-D features by PP-MOCVD. An outline of the results of, and the discussion about, the deposited TiO_2 thin films by PP-MOCVD is listed below.

4.1. Thickness of TiO_2 versus the Number of Pulses

4.2. Growth Rate of Deposited TiO_2 Thin Films

4.3. Conformality of Deposited TiO_2 Thin Film on 3-D Featured Substrate

4.4. Surface Morphology and Microstructure of Deposited TiO_2 Thin Films

4.5. Phase of Deposited TiO_2 Thin Films

4.6. Grain Size and Surface Roughness of Deposited TiO_2 Thin Films

4.7. Optical Properties of Deposited TiO_2 Thin Films

4.8. Measurements Accuracy

4.1. Thickness of TiO_2 versus the Number of Pulses

The relationship between TiO_2 thin film thickness and the number of pulses in PP-MOCVD was examined for Si_3N_4 substrates. This relationship was used as a guideline to determine the film thickness by controlling the number of pulses

at specific deposition conditions. The thicknesses were measured using the average thicknesses observed from the deposited TiO_2 fractioned surface by SEM. The depositions and the substrate were chosen based on the preliminary results of the conformality study on micro-scale features (Siriwongrungson et al., 2007). The deposition conditions were: a deposition temperature (T) of 400°C; base pressure (P_{min}) of 100 Pa; TTIP concentration (C_{mo}) of 0.15 mol%; injection volume (ν_L) of 50 µl and pulsing time (t) of 10 sec.

According to Figure 4-1, the linear relationship between the thickness and the number of pulses was obtained. The number of pulses was set to the maximum of 40 pulses because the thickness requirement of TiO_2 film for nanoimprint application was less than 50 nm. The linear relationship is written as Equation (4-1) with R^2 of 0.98.

$$\text{Film thickness} = 4.5\text{x}\text{Number of pulses} - 8.0 \qquad (4\text{-}1)$$

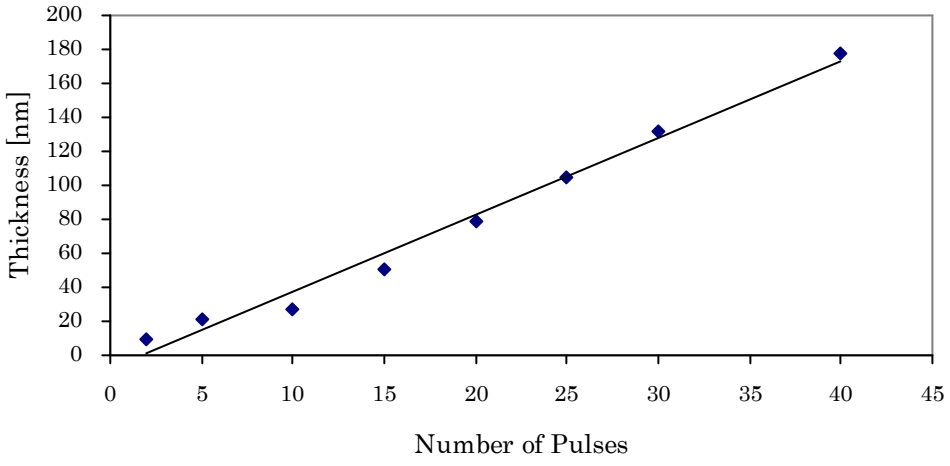

Figure 4-1: The thickness of TiO_2 as a function of the number of pulses in PP-MOCVD. (T = 400°C, P_{min} = 100 Pa, C_{mo} = 0.15 mol%, ν_L = 50 µl, t = 10 sec)

The linear fit relationship gave the growth rate of TiO_2 at the specified deposition conditions of 4.5 nm·pulse^{-1}. There was an initiation period for the growth of TiO_2 on Si_3N_4. The growth of TiO_2 started at approximately pulse number 1.8 and the growth initiation period depends on the substrate and material.

4.2. Growth Rate of Deposited TiO_2 Thin Film

The growth rate was investigated as a function of temperature, base pressure, precursor concentration, injection volume, pulsing or relaxation time and pulse exposure. Relaxation time is a unique processing parameter of PP-MOCVD as mentioned in Chapter 2.

4.2.1. Influence of Deposition Temperature on Growth Rate

The TiO_2 thin films were deposited on Si_3N_4 substrates at various deposition temperatures in the range of 400 to 600°C. The other deposition conditions were the base pressure of 100 Pa, precursor concentration of 0.50 mol%, injection volume of 100 μl and pulsing time of 10 sec or relaxation time of 0 sec. The growth rate increased as the deposition temperature increased and reached the maximum at 450°C with a growth rate of approximately 80±5 nm·min^{-1} as illustrated in Figure 4-2 and Figure 4-3. Figure 4-2 shows the Arrhenius relationship of inverse deposition temperature on natural logarithm growth rate to find the activation energy when surface kinetics is the rate limiting step, according to Equation (2-2). Figure 4-3 illustrates the effect of

deposition temperature on growth rate. The growth rate decreased as the deposition temperature increased after the maximum was reached.

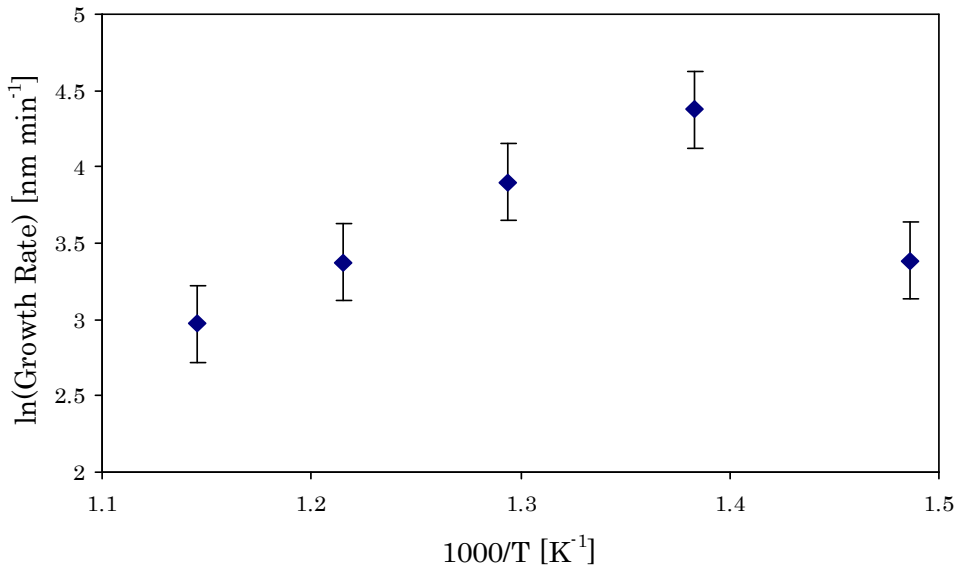

Figure 4-2: The natural logarithmic growth rate of TiO_2 as a function of inverse temperature.
(T = 400-600°C, P_{min} = 100 Pa, C_{mo} = 0.50 mol%, v_L = 100 µl, t = 10 sec)

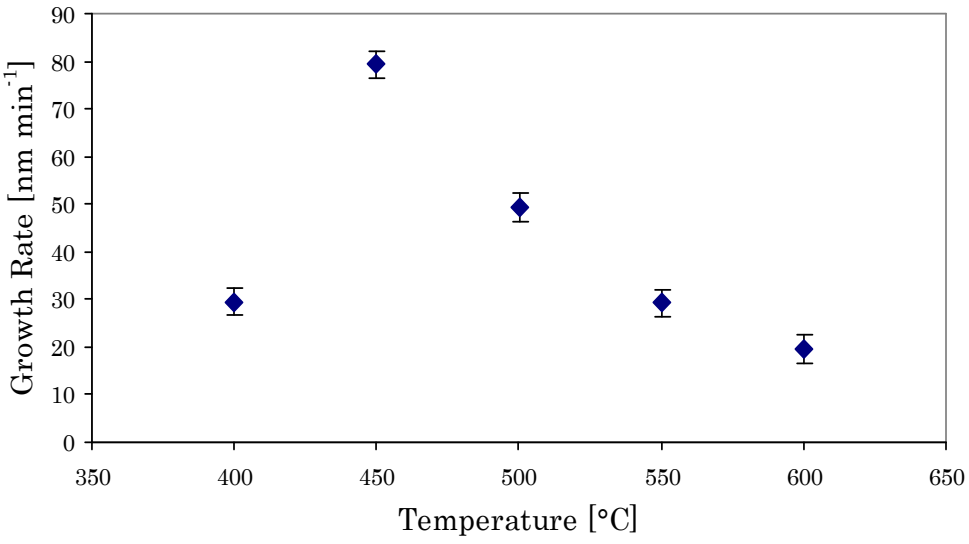

Figure 4-3: The growth rate of TiO_2 as a function of temperature showing surface kinetics and mass transport limited regions.
(T = 400-600°C, P_{min} = 100 Pa, C_{mo} = 0.50 mol%, v_L = 100 µl, t = 10 sec)

The influence of the deposition temperature on the growth rate of TiO_2 on Si_3N_4 by PP-MOCVD can be categorised based on many studies (Krumdieck, 1999; Morosanu, 1990). The surface kinetics was the rate limiting step before the growth rate reached the maximum. After the growth rate reached the maximum, it was limited by mass transport of the first kind, hence the gradual decrease in the growth rate.

Using the Arrhenius plot principle as given in Equation (2-2), the activation energy (E_a) was found to be 80±6 kJ·mole^{-1}. This activation energy of the TiO_2 deposition was close to the activation energy of 95±5 kJ·mole^{-1} for TiO_2 deposition on nickel from the study of Krumdieck (Krumdieck and Raj, 2001b).

4.2.2. Influence of Base Pressure on Growth Rate

The effect of base pressure on the growth rate of TiO_2 was investigated using Si_3N_4 substrates without any micro- or nano-scale patterns. The deposition temperatures were 400, 450 and 500°C. The precursor concentration, injection volume and relaxation time were kept constant at 0.15 mol%, 50 µl and 0 sec, respectively. The growth rate was in the range of 15.7 to 22.7 nm·min^{-1}.

In conventional steady flow over a substrate CVD process, the base pressure has a strong effect on growth rate when mass transport of the second kind is the rate limiting step. The base pressure influences the boundary layer thickness on the substrate surface, hence the diffusion of the precursor to the substrate

surface. The boundary layer thickness increases as the pressure increases (Pierson, 2006).

According to this study as illustrated in Figure 4-4, the base pressure has minor effects on growth rate and total molecular flux. The peak pressure and the exposure were slightly decreased as the base pressure increased. This implies that the total molecular flux was not strongly affected by the base pressure and the evaporation rate tended to decrease with increased base pressure. The pulsing of the liquid precursor of PP-MOCVD results in a pulsing pressure profile that reduces the effect of base pressure on growth rate. The diffusion boundary layer thickness on the substrate surface is not a function of base pressure for PP-MOCVD. This agrees with the growth rate versus temperature as shown in Figure 4-2 and Figure 4-3. There was no mass transport of the second kind limited in this study.

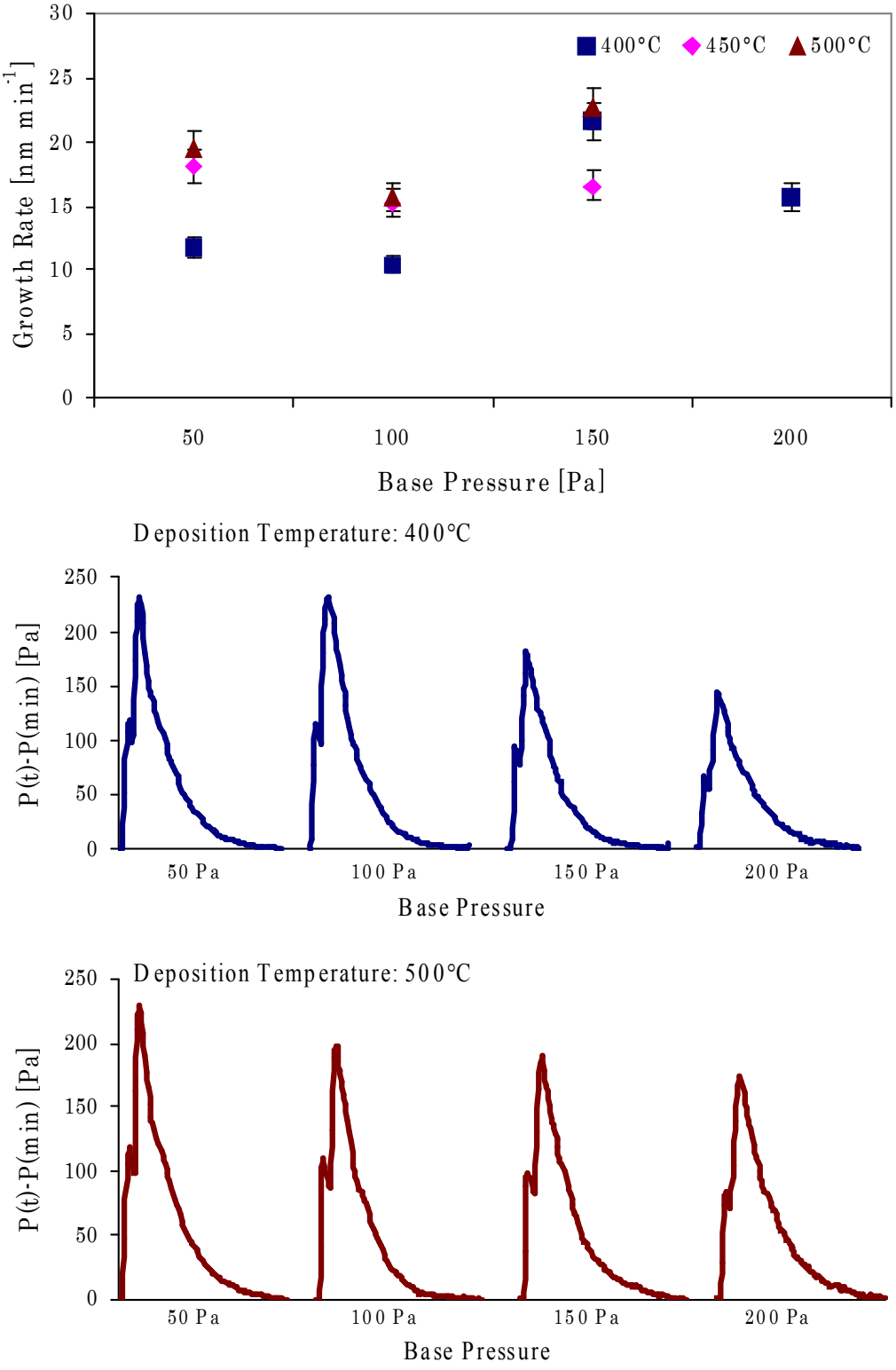

Figure 4-4: The growth rate of TiO_2 and reactor pressure as a function of base pressure showing the independence of growth rate on base pressure and the decrease of peak pressure with increasing base pressure.

(T = 400-500°C, P_{min} = 50-200 Pa, C_{mo} = 0.15 mol%, ν_L = 50 µl, t = 10 sec)

4.2.3. Influence of Precursor Concentration on Growth Rate

The influence of the precursor concentration on the growth rate of TiO_2 was examined on Si_3N_4 with nano-scale featured or non-featured substrates. The precursor concentrations were 0.05, 0.15, 0.25 and 0.50 mol%. Other processing parameters were kept constant at the deposition temperature of 400°C, base pressure of 100 Pa, injection volume of 50 μl and relaxation time of 0 sec. The growth rate was varied in a range between 2.8 and 18.4 $nm \cdot min^{-1}$ for featured substrates and 7.4 and 44.7 $nm \cdot min^{-1}$ for non-featured substrates.

Figure 4-5 shows the growth rate of deposited TiO_2 as a function of precursor concentration. The growth rate increased as the precursor concentration increased. In the case of non-featured substrate, the growth rate increased linearly to the maximum before decreasing at the precursor concentration of 0.50 mol%. The growth rate of non-featured substrate before decreasing implies a first order relationship between growth rate and precursor concentration. Generally, the growth rate increases in the first order of reactant partial pressure (Morosanu, 1990). Additional information is needed to verify the decrease in the growth rate at the precursor concentration of 0.50 mol%.

In the case of featured substrates, the growth rate also increased as the precursor concentration increased but with less effect. More experiments are needed to identify the relationship between growth rate and precursor concentration in this case. The growth rate increased drastically at the precursor concentration of 0.50 mol% because of the average thickness measurement as mentioned in Section 3.3.2. The deposited film was thicker at

the top of the trench where the average thickness was taken. This resulted in a strong decrease in conformality.

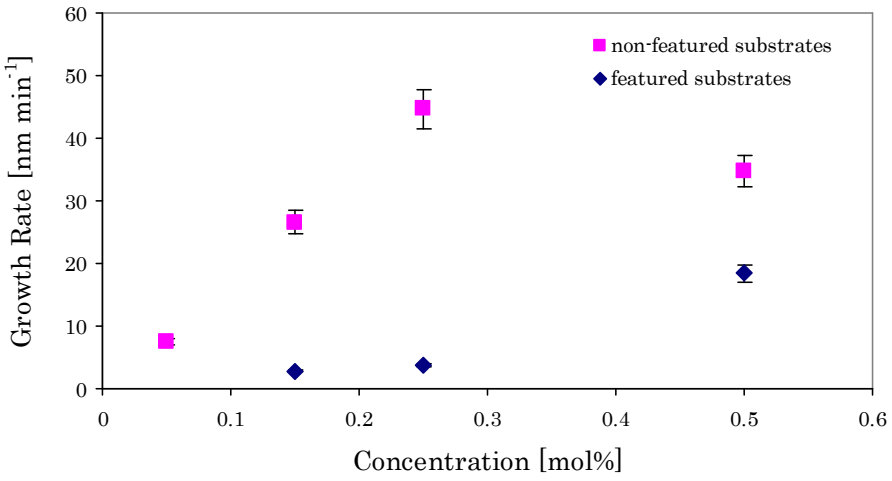

Figure 4-5: The growth rate of TiO_2 as a function of precursor concentration on silicon nitride non-featured and featured substrates.

(T = 400°C, P_{min} = 100 Pa, C_{mo} = 0.05-0.50 mol%, v_L = 50 µl, t = 10 sec)

The precursor concentration did not affect the peak pressure at the same base pressure and exposure. This might be because the precursor was dissolved in toluene; hence the vapour pressure of the toluene is the principal influence on peak pressure and exposure.

4.2.4. Influence of Injection Volume on Growth Rate

The effect of the injection volume on the growth rate was examined on substrates with nano-scale features of Si_3N_4. The injection volumes were 50, 100 and 250 µl at the deposition temperatures of 400 and 500°C. The precursor concentration, base pressure and relaxation time were kept constant at 0.15 mol%, 100 Pa and 0 sec, respectively. The growth rate was between 2.8 and 16.5 nm·min^{-1}.

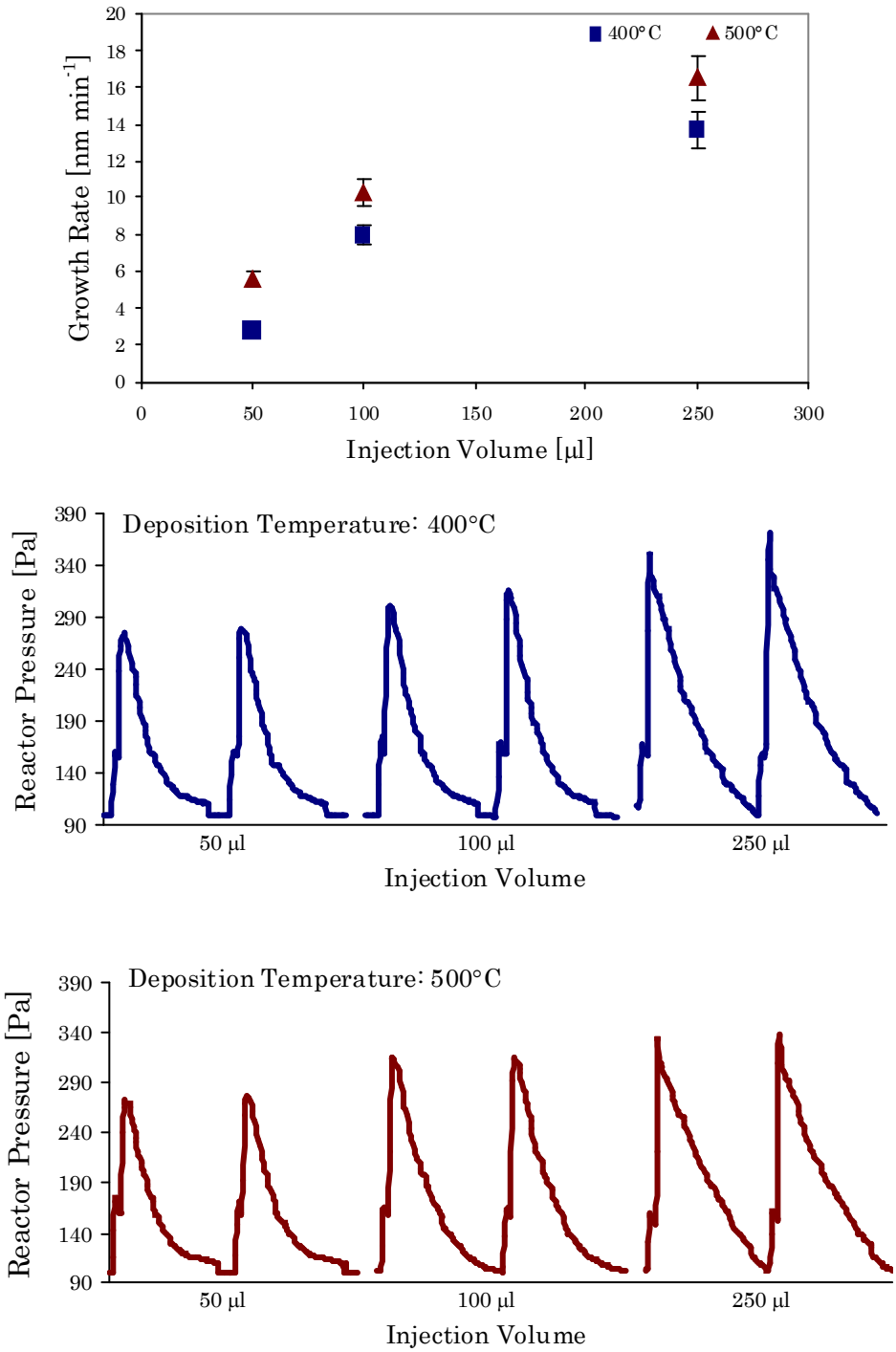

Figure 4-6: The increase in the growth rate of the as-deposited TiO_2, peak pressure and exposure with the increase in precursor injection volume.

(T = 400, 500 °C, P_{min} = 100 Pa, C_{mo} = 0.15 mol%, v_L = 50-250 µl, t = 10 sec)

Figure 4-6 shows the growth rate and reactor base pressure as a function of precursor injection volume at the deposition temperatures of 400 and 500°C. There was no difference in growth rate and reactor base pressure between the two different deposition temperatures. The growth rate, peak pressure and exposure increased as the injection volume increased.

The influence of the injection volume on the growth rate was expected to have a similar trend to concentration. The injection volume and precursor concentration affected the total molecular flux as shown in Equations (2-19) and (2-21). The injection volume influenced the exposure, hence total molecular flux

4.2.5. Influence of Relaxation Time on Growth Rate

The effect of the relaxation time on the growth rate of TiO_2 was investigated using plain Si_3N_4 substrates without any micro- or nano-scale structures. The base pressure, precursor concentration and injection volume were kept constant at 100 Pa, 0.15 mol% and 50 µl, respectively. The relaxation times were varied at 0, 2.5, 5 and 10 sec at the deposition temperatures of 400, 450 and 500°C. The growth rate ranged from 0.9 to 2.9 nm·pulse^{-1}.

The growth rate was calculated in nm·pulse^{-1} as the longer the relaxation time the slower the growth rate in nm·min^{-1}. The deposited TiO_2 films have an average thickness of 255±4.5 nm, excluding the data point at the deposition temperature of 400°C with 0 sec relaxation time, which has the film thickness

of 141 nm. The number of pulses was varied to keep the thickness in the same range and ranged from 88 to 200 pulses.

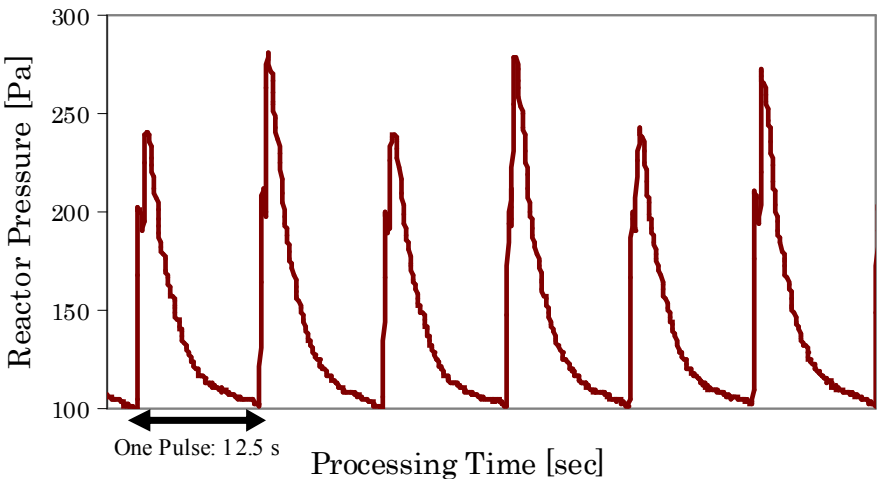

Figure 4-7: The unique reactor pressure at the relaxation time of 2.5 sec showing two peak pressures in every two pulses cycles.

(T = 500°C, P_{min} = 100 Pa, C_{mo} = 0.15 mol%, ν_L = 50 µl, t = 12.5 sec)

Peak pressure and exposure at the relaxation time of 2.5 sec were unique. There were two peak pressures repeated in the pattern as shown in Figure 4-7. Nothing can be concluded at this point about the reactor pressure behaviour at a relaxation time of 2.5 sec.

As illustrated in Figure 4-8, there was no difference in peak pressure and exposure at different deposition temperatures. The peak pressure and exposure at other relaxation times were slightly increased as the relaxation time increased. Peak pressure and exposure should be independent of the relaxation time in this study because the reactor reached the minimum at the relaxation of 0 sec. Other parameters that affect exposure and peak pressure were remained constant except the evaporation rate.

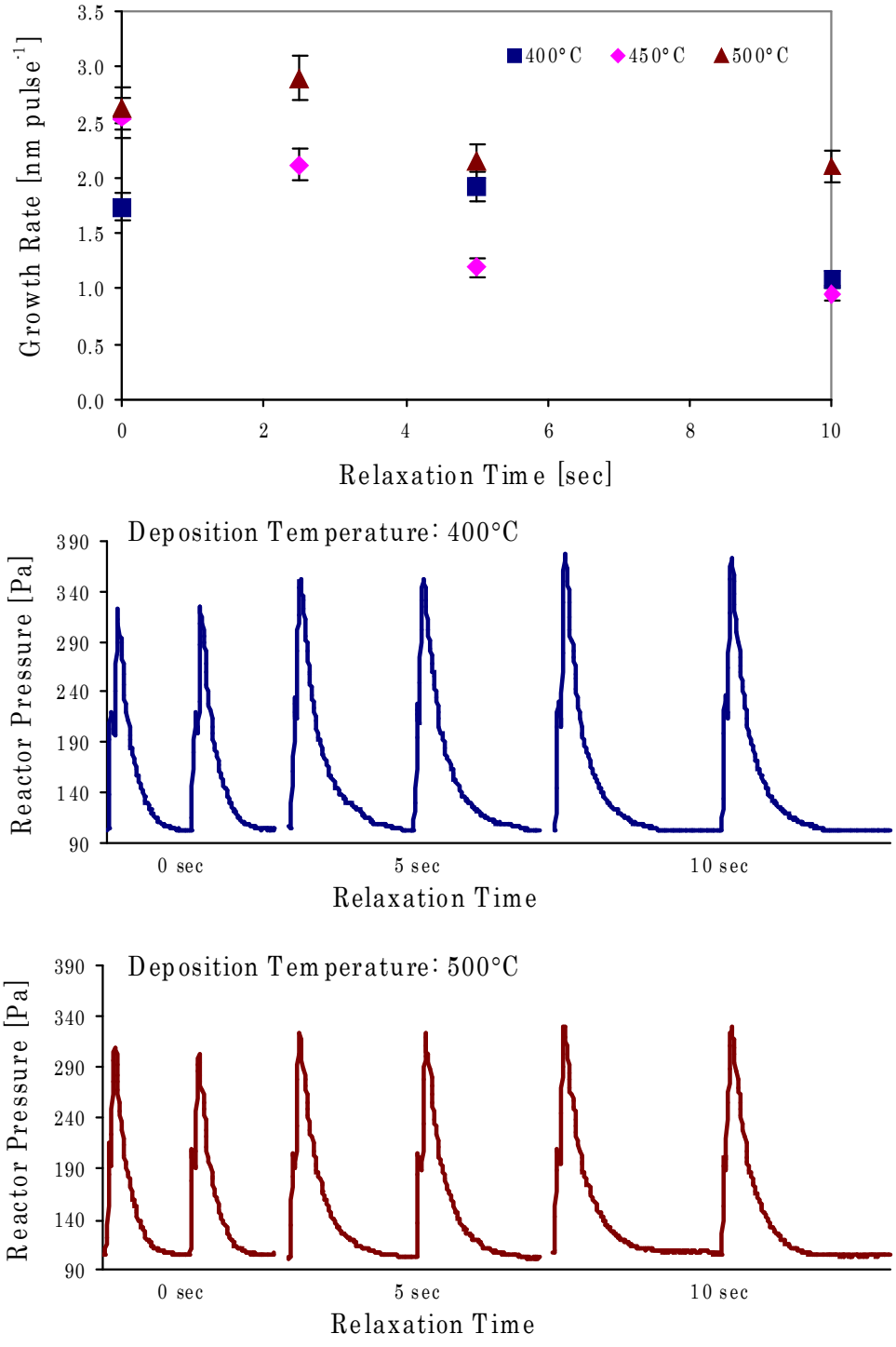

Figure 4-8: The growth rate of TiO_2 reactor pressure at various relaxation times.

(T = 400-500°C, P_{min} = 100 Pa, C_{mo} = 0.15 mol%, ν_L = 50 µl, t = 10-20 sec)

Relaxation time has a minor effect on the growth rate at the deposition temperatures of 400 and 500°C. The growth rate should not be affected by the relaxation time because the relaxation time provided time for the precursor atoms to incorporate and grow with other crystals. The growth rate slightly decreased as the relaxation time increased at the deposition of 450°C. The growth rate is expected to reach a minimum when the evaporation rate of the adsorbed precursor molecules is no longer changing with relaxation time.

4.3. Conformality of Deposited TiO_2 Thin Film on 3-D Featured Substrate

The conformality of deposited TiO_2 on micro- and nano-scale featured substrates using TTIP by PP-MOCVD was investigated over a range of deposition temperatures, precursor concentration and injection volume. Three processing parameters were chosen because of the limited number of patterned substrates. The deposition temperature, precursor concentration and injection volume influenced the growth rate of deposited TiO_2. The injection volume also affected the peak pressure and exposure of the precursor molecules on the substrate surface. The base pressure and relaxation time have minor effects on growth rate, peak pressure and exposure; hence they were not included in the conformality study.

The effect of deposition temperature was carried out on micro-scale featured substrates. Nano-scale featured substrates were used to study the influence of precursor concentration and precursor injection volume on conformality.

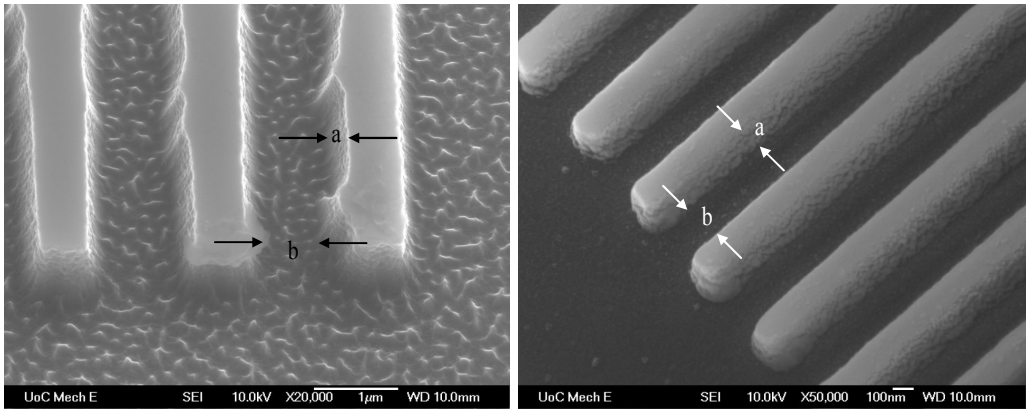

Figure 4-9: Two examples of silicon (left) and silicon nitride (right) featured substrates before deposition where (a) is the trench depth and (b) is the trench width.

Figure 4-9 illustrates the micro-scale features on Si and nano-scale structures on Si_3N_4 substrates. The aspect ratio is defined here as the trench depth to trench width as depicted as (a) and (b), respectively in Figure 4-9. The conformality was calculated using Equation (3-3).

4.3.1. Influence of Deposition Temperature on Conformality

The influence of deposition temperature on deposited TiO_2 conformality was studied using micro-scale structures on Si with an aspect ratio of 1:1 as substrates. The deposition temperature was varied between 400 and 600°C. The base pressure, precursor concentration, precursor injection volume and relaxation time were kept constant at 100 Pa, 0.50 mol%, 100 μl and 0 sec, respectively. The conformality of deposited TiO_2 as a function of deposition temperature was in the range of 0.82 to 0.95.

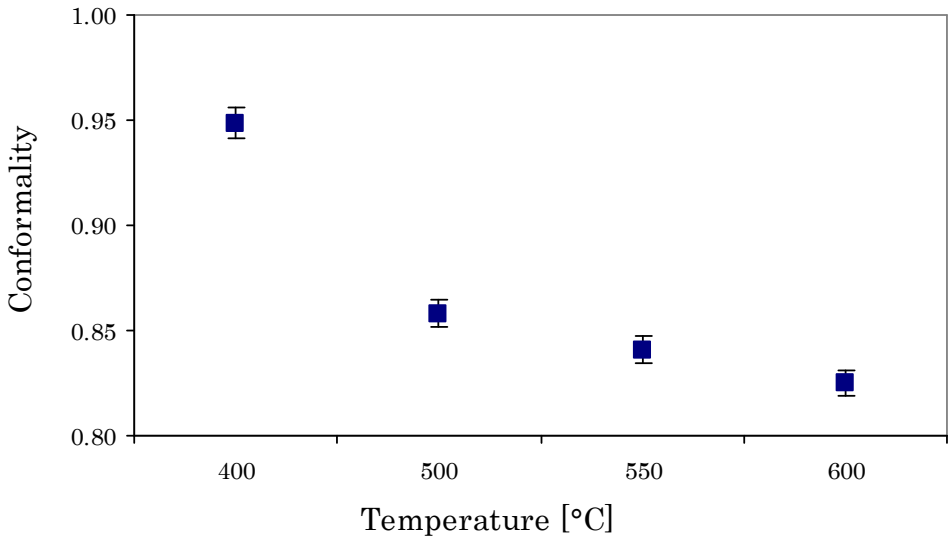

Figure 4-10: The decreasing of conformality of as-deposited TiO_2 thin films with an increase in deposition temperature.

(T = 400-600°C, P_{min} = 100 Pa, C_{mo} = 0.50 mol%, ν_L = 100 µl, t = 10 sec)

Figure 4-11 and Figure 4-12 show the SEM images of the cross-section of fracture surfaces of deposited TiO_2 with average top and bottom thickness for conformality at various deposition temperature studies. Qualitatively, the deposited TiO_2 films had the same thickness with an insignificant difference on the edge of the micro-scale features and flat surface. Quantitatively, the conformality of the films varied inversely with the deposition temperature as shown in Figure 4-10. The maximum conformality of 0.95 was obtained at the deposition temperature of 400°C, which was the lowest deposition temperature in this study. The minimum conformality of 0.82 was calculated at the deposition temperature of 600°C, which was the highest deposition temperature in this case.

The conformality of the films in conventional cross-flow CVD reactors is affected by the flow regime, gas phase reaction, surface kinetics and mass

transfer (Dauksher et al., 2006). At a lower deposition temperature, the surface reaction is the rate limiting step. Surface kinetics is favourable in order to produce a good conformal coating on the features. The rate limiting step changes from surface kinetics to mass transport as the deposition temperature increases. The deposition temperature also influences the relative rates of sticking or re-evaporation, thermal decomposition reaction and surface diffusion or crystal growth. As the deposition temperature increases, the precursor molecules tend to stick, adsorb and react once they reach the substrate surface. This might cause precursor depletion and the films on top of the features to be thicker than at the bottom.

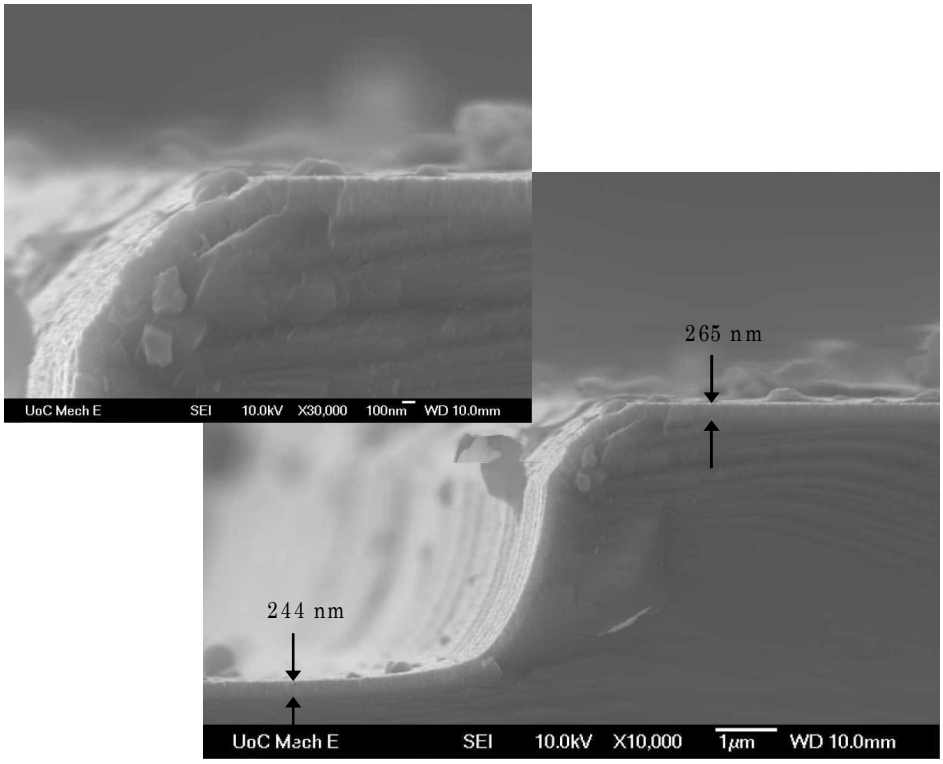

(a) 400 °C; C = 0.93

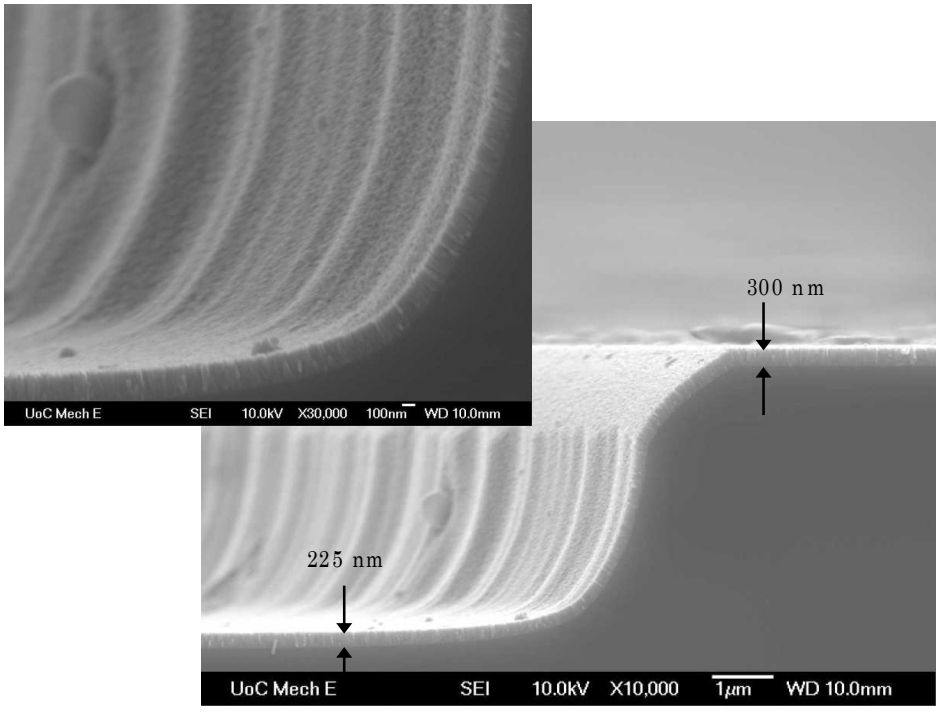

(b) 500 °C; C = 0.87

Figure 4-11: SEM images at 10,000 and 30,000x magnification for the corner close-up of the cross-section of a fracture surface of deposited TiO_2 thin films showing the conformality as a function of temperature with average top and bottom thickness as indicated. C is the conformality calculated from Equation (3-3).

(T = 400-500°C, P_{min} = 100 Pa, C_{mo} = 0.50 mol%, ν_L = 100 μl, t = 10 sec)

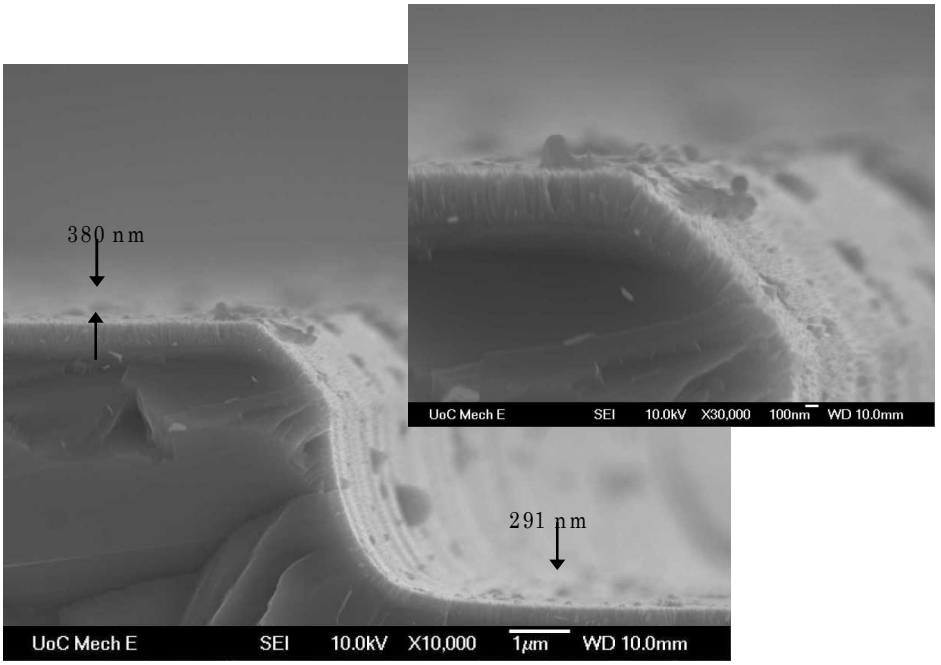

(a) 550 °C; C = 0.83

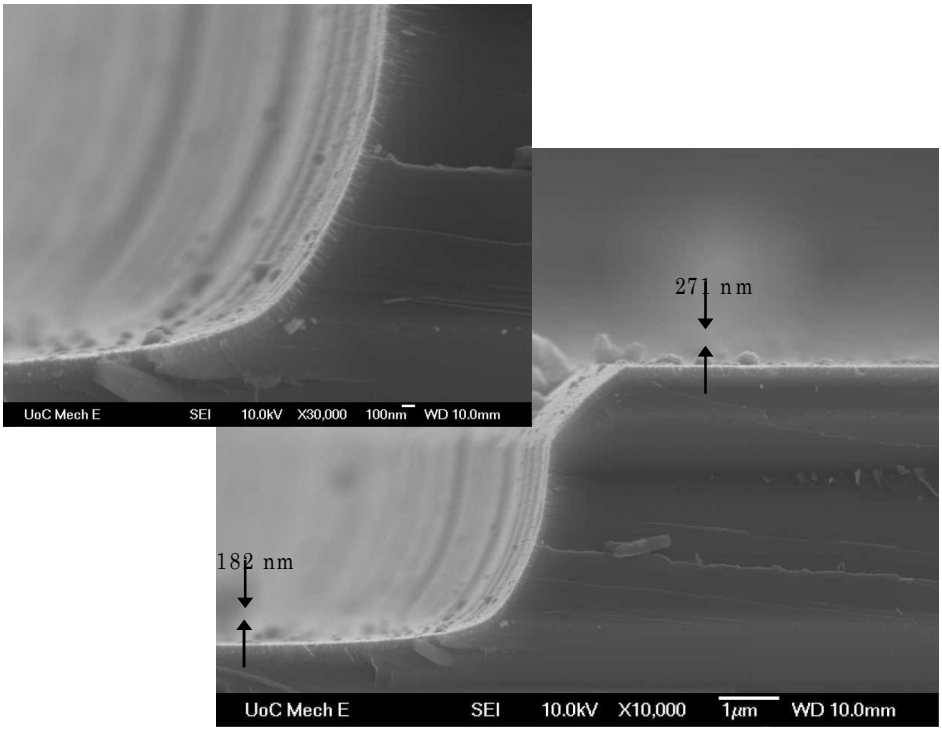

(b) 600 °C; C = 0.82

Figure 4-12: SEM images at 10,000 and 30,000x magnification for the corner close-up of the cross-section of a fracture surface of deposited TiO_2 thin films showing the conformality as a function of temperature with average top and bottom thickness as indicated. C is the conformality calculated from Equation (3-3).

(T = 550-600°C, P_{min} = 100 Pa, C_{mo} = 0.50 mol%, v_L = 100 μl, t = 10 sec)

4.3.2. Influence of Injection Volume on Conformality

The influence of liquid precursor injection volume on conformality was examined with the substrate having nano-scale structures on Si_3N_4 with the aspect ratio of 1:2. The injection volumes were 50, 100 and 250 μl. The deposition temperature was held at 400 and 500°C. The base pressure, precursor concentration and relaxation time were maintained at 100 Pa, 50 μl and 0 sec, respectively. The conformality of deposited TiO_2 as a function of liquid precursor injection volume was in the range of 0.81 to 0.87.

Figure 4-13 illustrates the conformality at the deposition temperature of 400 and 500°C with various precursor injection volumes. The conformality was not affected by injection volume at deposition temperatures of 400 and 500°C. Figure 4-14 shows SEM images of the cross-section of a fracture surface of deposited TiO_2 at various deposition temperatures and injection volumes. The thicknesses at the top of the trenches are slightly thicker than at the bottom of the trenches. There were no noticeable variations in thicknesses difference between the top and bottom of the trenches at various deposition temperatures and injection volumes.

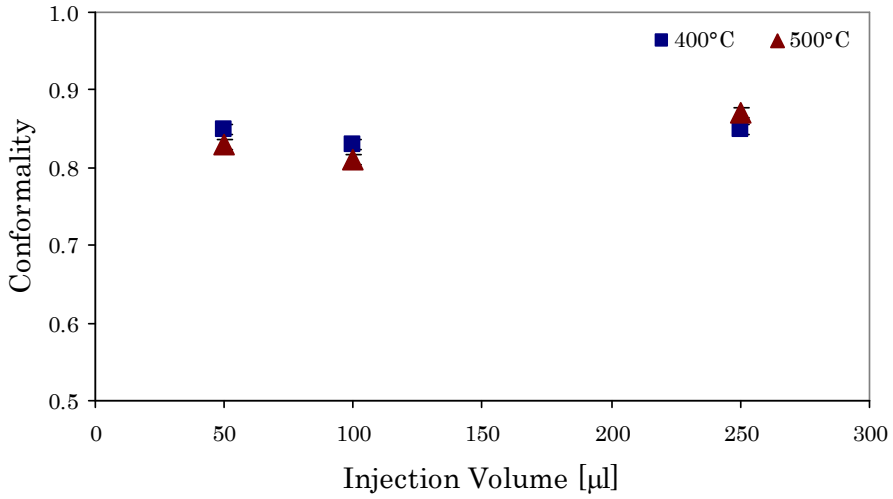

Figure 4-13: The independence of the conformality of deposited TiO_2 thin films from the injection volume.

(T = 400, 500°C, P_{min} = 100 Pa, C_{mo} = 0.15 mol%, ν_L = 50, 100, 250 µl, t = 10 sec)

The deposited films were thicker at the top of the trench compared to the bottom of the trench because of the difference in free energy, sticking coefficient and nucleation as discussed in Section 4.3.2. The sticking coefficient depended on deposition temperature and crystal orientation on the substrate surface. The increase in injection volume did not affect the sticking coefficient. The chance of molecules diffusing and reacting on the substrate surface was less affected by an increase in injection volume compared to precursor concentration.

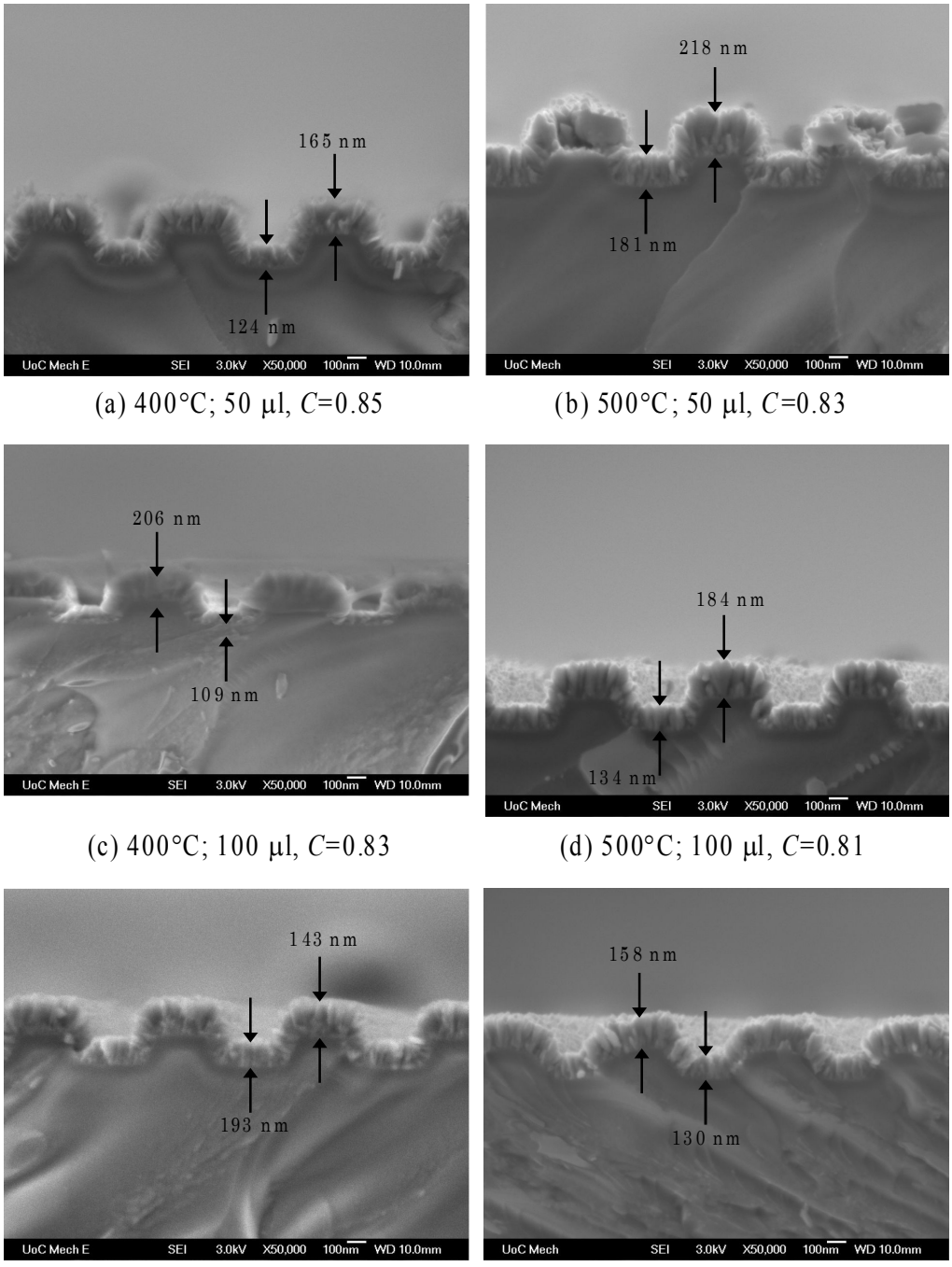

(a) 400°C; 50 µl, C=0.85 (b) 500°C; 50 µl, C=0.83

(c) 400°C; 100 µl, C=0.83 (d) 500°C; 100 µl, C=0.81

(e) 400°C; 250 µl, C=0.85 (f) 500°C; 250 µl, C=0.87

Figure 4-14: SEM images at 50,000x magnification of the cross-section of a fracture surface of deposited TiO_2 thin films showing conformality at various liquid precursor injection volumes and deposition temperatures on Si_3N_4 substrate with features size of 300 nm and aspect ratio of 1:2.

(T = 400, 500°C, P_{min} = 100 Pa, C_{mo} = 0.15 mol%, ν_L = 50, 100, 250 µl, t = 10 sec)

4.3.3. Influence of Pulse Exposure on Conformality

The influence of peak pressure and exposure were discussed in Section 4.1. The peak pressure that affected the exposure and total molecular flux were base pressure, precursor injection volume and relaxation time. In this section, the effect of pulse exposure, as written in Equation (2-22), was investigated.

The influence of pulse exposure on conformality includes the effect of injection volume and precursor concentration as one dimensionless parameter. The study was conducted on micro- and nano-scale patterned Si_3N_4 substrates and the pulse exposures were varied from 32 to 214. Table 4-1 shows the conformality and the influences of precursor concentration and injection volume on pulse exposure at the deposition temperature of 400°C. The temperature, base pressure and relaxation time were fixed at 400 and 500°C, 100 Pa and 0 sec, respectively. The maximum conformality was 0.87 and the minimum was 0.81.

Figure 4-15 illustrates the conformality at various pulse exposures. The pulse exposure has minor effects on conformality, which was strongly dependent on the deposition temperature, as shown in Section 4.3.1. Conformality of at least 0.80 was expected in this study.

Table 4-1: The effect of pulse exposure from injection volume and precursor concentration on conformality at the deposition temperature of 400°C.

Pulse Exposure	Concentration [mol%]	Injection Volume [µl]	Conformality
32	0.15	50	0.85
53	0.25	50	0.83
64	0.15	100	0.83
160	0.15	250	0.85

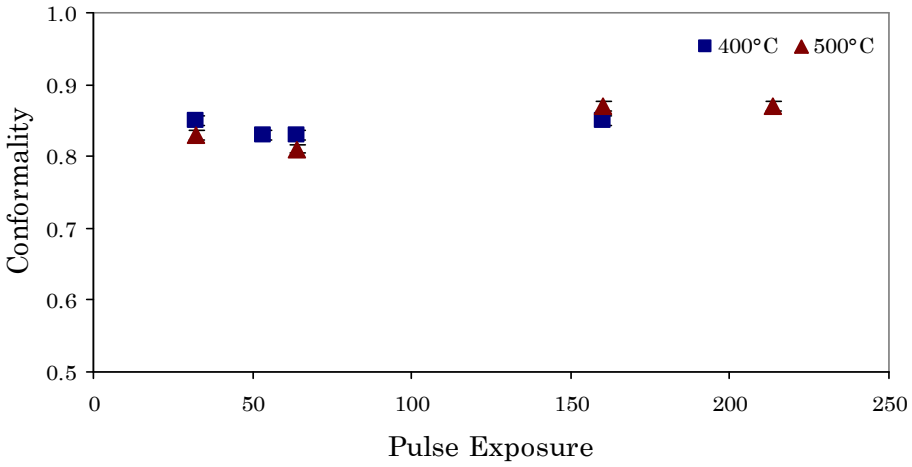

Figure 4-15: The fairly constant conformality with the changing of pulse exposure. (T = 400, 500°C, P_{min} = 100 Pa, C_{mo} = 0.15-0.50 mol%, ν_L = 50-250 µl, t = 10 sec)

In PP-MOCVD, the peak pressure affects nucleation as peak pressure represents the molecular arrival rate of the precursor (Ramirez et al., 2008). The molecular arrival rate affects the surface and gas diffusion, hence mass transport. The conformality outcomes imply that surface kinetics was the rate limiting step for the depositions. According to this study, the injection volume influenced peak pressure and total molecular flux but had no effect on conformality. Other processing parameters that affect peak pressure and total

molecular flux as well as pulse exposure are base pressure and relaxation time, which were not included in the conformality study.

Base pressure affects the mean free path of the precursor molecules, and further study should be undertaken to confirm the effects of base pressure. The mean free path is longer at lower base pressure. The precursor molecules that have a long mean free path cannot diffuse into a small trench or via that is smaller in size than the mean free path. At high base pressure, the precursor molecule is likely to stay on the surface of the patterned substrate because the mean free path is too short to diffuse down to the bottom of a trench or via.

4.3.4. Conformality Observations on Various Features Size

The conformality over the range of feature sizes, aspect ratio and deposition conditions of TiO_2 on Si_3N_4 is illustrated in Figure 4-16. The feature sizes were from 100 nm to 500 nm wide and 100 nm to 500 nm deep which yields the aspect ratio of 1:1, 1:2 and 2:1. The deposition temperatures were 400 and 500°C with precursor concentration from 0.15 to 0.50 mol%. The precursor injection volumes were 50 and 250 μl. The reactor base pressure and relaxation time were the same at 100 Pa and 0 sec, respectively.

Figure 4-16 and Figure 4-17 are cross-section SEM images of fracture surfaces of deposited films with different precursor concentrations on featured substrates with different aspect ratios and features sizes and shapes. The maximum conformality of deposited TiO_2 by PP-MOCVD on a nano-scale trench was 0.87 as shown in Figure 4-16 (a). The feature size was 200 nm with

the aspect ratio of 1:2. Figure 4-16 (b) illustrates a deposited TiO_2 film on a small feature size of 100 nm. The features were triangular cross-section shape and the deposited TiO_2 films tended to follow the shape. However, the conformality calculated in this study gave the low conformality of 0.51. The film growth was accentuated at the pointed tip of the triangle shape.

Figure 4-17 shows the SEM images of conformality observation at two deposition temperatures on the nano-scale featured substrates of similar size and aspect ratio. Conformality noticeably decreased as the deposition temperature increased from 400 to 500°C with other process parameters remaining the same. The deposition at the precursor concentration of 0.25 mol% and deposition temperature of 500°C resulted in the poorest conformality in this study. The film was three to six times thicker at the top than the bottom of the trench. The deposited film had fairly conformal coating inside the trench but accelerated growth on top. This growth regime can be useful in making closed voids or holes in a substrate.

Conformality depends not only on the rate limiting step, but also on the sticking coefficient and free energy of precursor molecules that influence nucleation and film growth. The sticking coefficients of the surfaces of the trench can be of different crystallographic orientations, and the trench dimensions are varied (Kasu and Kobayashi, 1997). In addition, the free energy is lower at the edge of the trench mouth. These resulted in higher nucleation and film growth at the edge and on top of the trench at higher temperature.

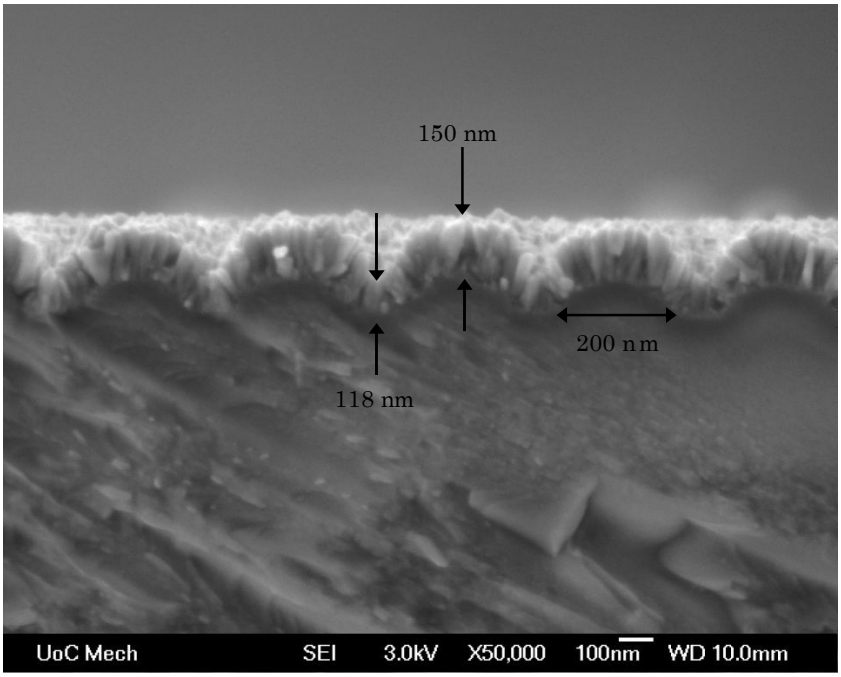

(a) 500°C; 0.15 mol%; 250 µl; $C = 0.87$;
58 pulses; Aspect Ratio: 1:2; 50,000x

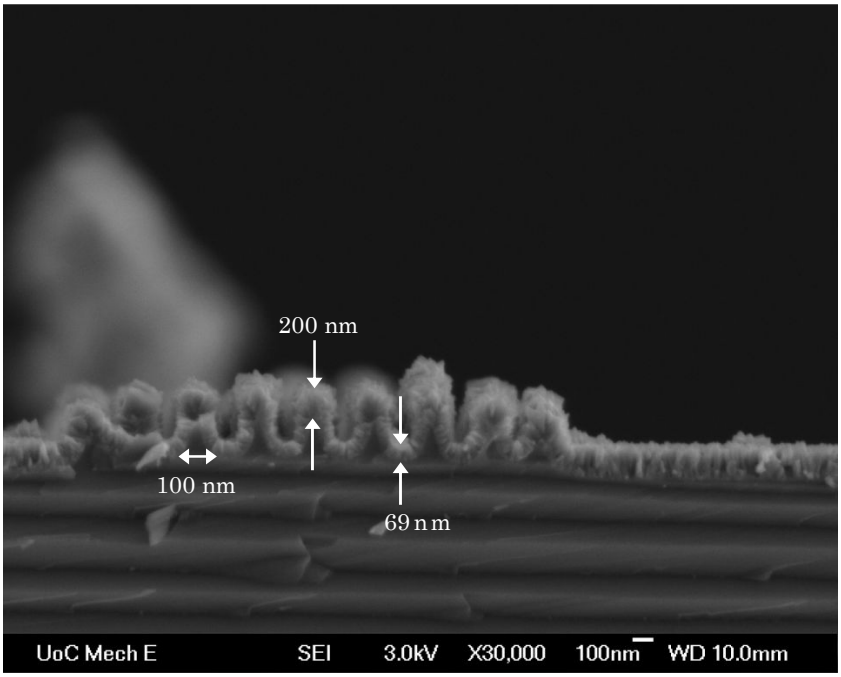

(b) 400°C; 0.50 mol%; 50 µl; $C = 0.51$;
60 pulses; Aspect Ratio: 1:1; 30,000x

Figure 4-16: The conformality of deposited TiO_2 on Si_3N_4 featured substrates with various feature sizes and deposition conditions. (a) possible filling over a trench with the aspect ratio of 1:2 (b) low conformal coating on a nano-scale feature size.

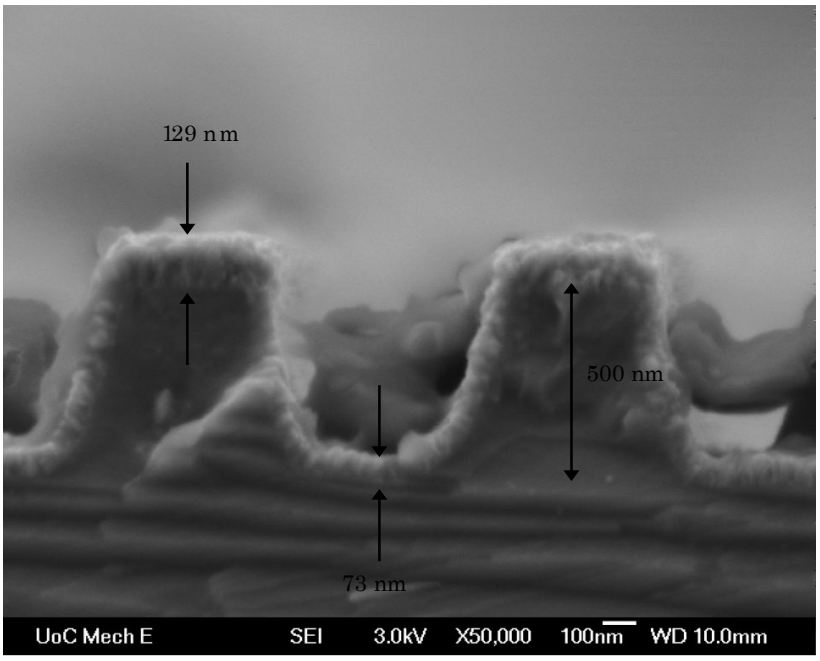

(a) 400°C; 0.25 mol%; 50 µl; $C = 0.83$;
143 pulses; Aspect Ratio: 1:1; 50,000x

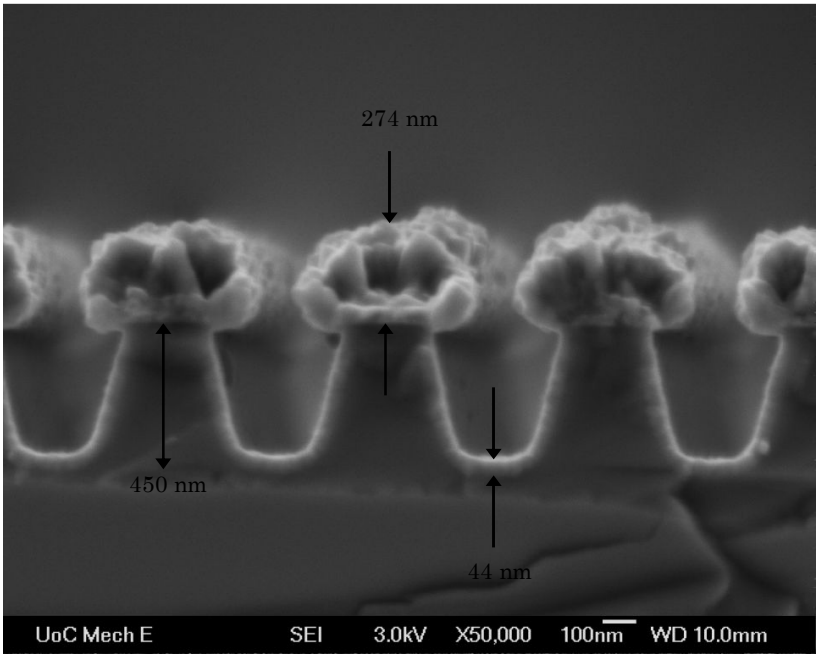

(b) 500°C; 0.25 mol%; 50 µl; $C = 0.45$;
159 pulses; Aspect Ratio: 1:1; 50,000x

Figure 4-17: The conformality of deposited TiO_2 on Si_3N_4 featured substrates with various feature sizes and deposition conditions. (a) conformal coating with aspect ratio of 1:1 (b) closed gap with void coating possibility over a trench.

4.4. Surface Morphology and Microstructure of Deposited TiO_2 Thin Film

The surface morphology and microstructure of as-deposited TiO_2 thin films at different deposition conditions were analysed using scanning electron microscopy (SEM). The processing parameters studied included deposition temperature, base pressure, precursor concentration, precursor injection volume and relaxation time. The substrate types are known to influence the microstructure, properties and crystallite size of the deposited films (Duminica et al., 2007; Sankapal et al., 2005). Nevertheless, the effect of substrates on the TiO_2 morphology was not included in this study.

4.4.1. Surface Morphology and Microstructure of Deposited TiO_2 at Various Temperatures

The TiO_2 was deposited on 1 to 500 μm gratings on Si_3N_4 substrates. The deposition conditions were maintained at a base pressure of 100 Pa, 0.50 mol% of precursor concentration, 100 μl of injection volume and a relaxation time of 0 sec. The deposition temperatures were in the range of 400 to 600°C, and the thicknesses of the deposited films were between 260 nm to 2.60 μm with the number of pulses between 41 and 80. The number of pulses was 200 pulses for the film thickness of 2.6 μm. The thickest film was deposited at 450°C when the maximum growth rate occurred.

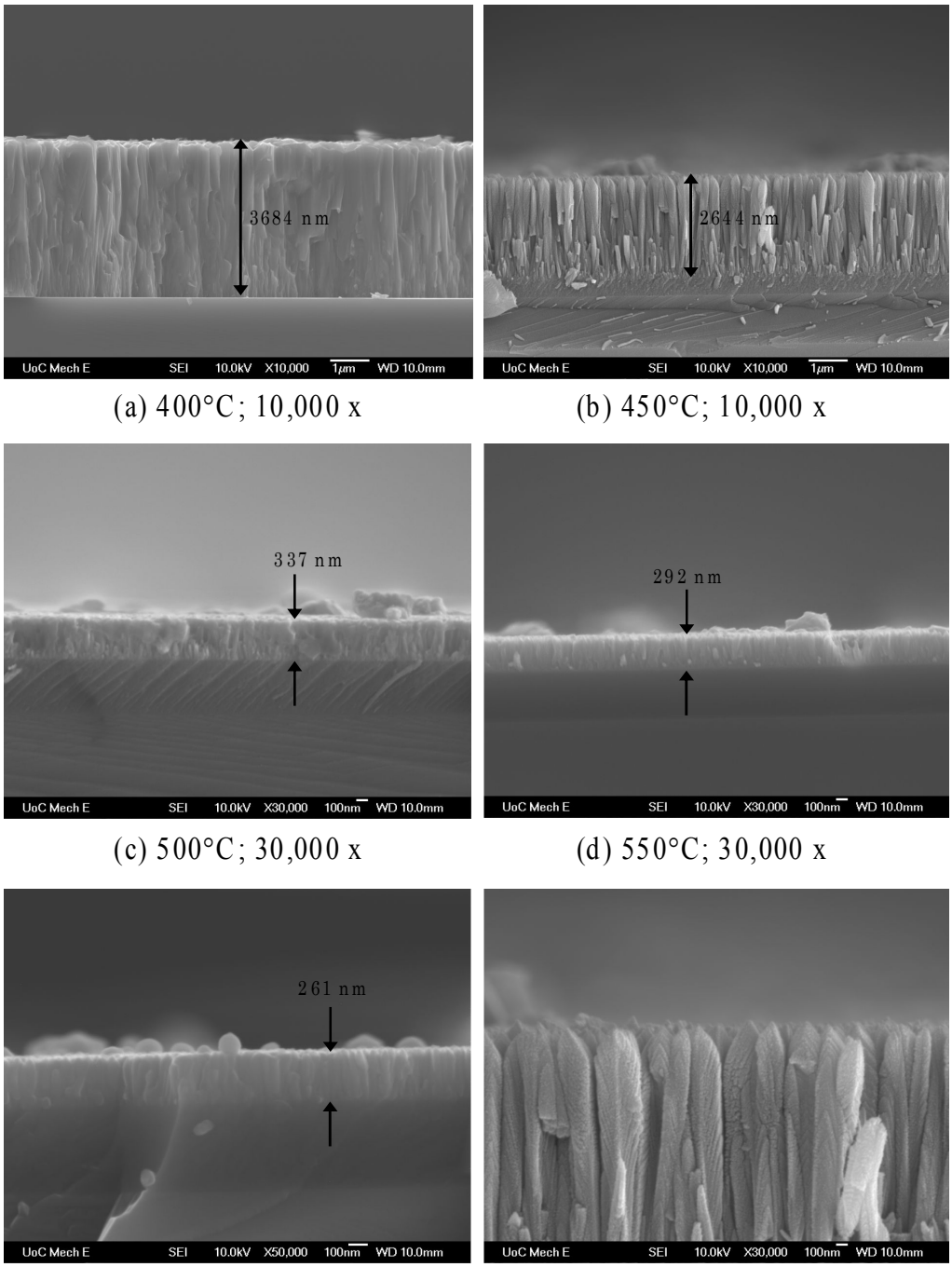

(a) 400°C; 10,000 x (b) 450°C; 10,000 x

(c) 500°C; 30,000 x (d) 550°C; 30,000 x

(e) 600°C; 50,000 x (f) 450°C; 30,000 x

Figure 4-18: SEM images of cross-sections of a fracture surface of deposited TiO_2 thin films on Si_3N_4 substrates showing columnar structure at various deposition temperatures with the average of 88 pulses.

(T = 400-600°C, P_{min} = 100 Pa, C_{mo} = 0.50 mol%, v_L = 100 µl, t = 10 sec)

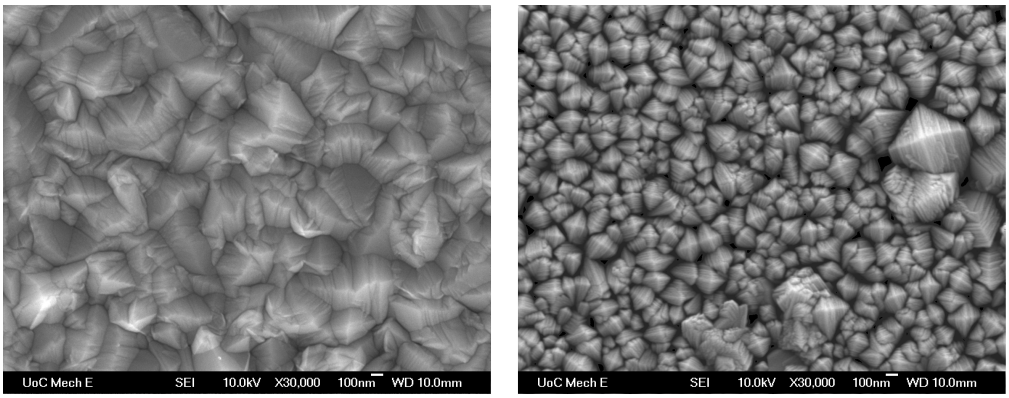

(a) 400°C (b) 450°C

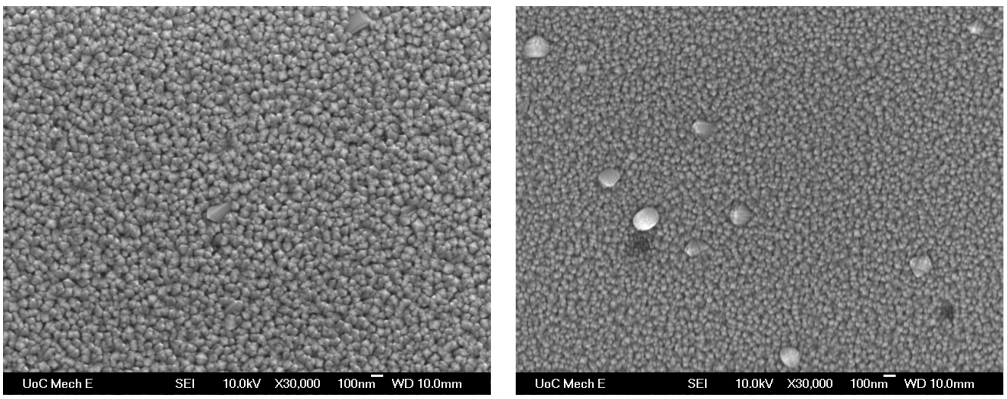

(c) 500°C (d) 550°C

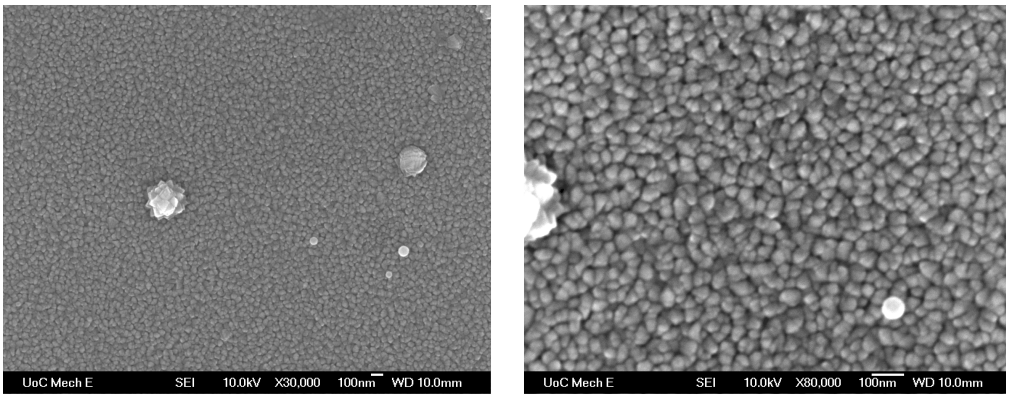

(e) 600°C (f) 600°C at 80,000 x

Figure 4-19: SEM images of surface micrographs at 30,000x magnification of deposited TiO_2 thin films on Si_3N_4 substrates over the range of deposition temperatures with the average of 88 pulses. The grain sizes appeared to decrease with increasing deposition temperature.

(T = 400-600°C, P_{min} = 100 Pa, C_{mo} = 0.50 mol%, v_L = 100 µl, t = 10 sec)

Figure 4-18 shows SEM images of fracture surface cross-sections of films grown on Si_3N_4 single crystal substrates. Figure 4-19 illustrates SEM images of surface morphology of deposited TiO_2 of the same Si_3N_4 substrate at various deposition temperatures.

The deposited TiO_2 films were crystalline with columnar microstructure. As illustrated in Figure 4-19, the crystal structure of the film at the deposition temperature of 400°C looked different from that at the other deposition temperatures. This agreed with the XRD analysis, which will be explained later in this chapter, that certain anatase peaks were missing compared to the result at the deposition temperature of 600°C. Some large round structures were observable on the surface of the deposited films. This might be because of the initiation of the decomposition of the precursor in the vapour phase at a higher temperature. More large structures were observed at higher temperatures. These structures appear to be on the surface, yet somewhat incorporated into the film and were not blown off by a compressed air jet. The round structures also appear to be crystalline in structure, and there is also some fracture debris visible on some sample surfaces. This debris is usually flat in shape instead of round.

4.4.2. Surface Morphology and Microstructure of Deposited TiO_2 at Various Base Pressures and Relaxation Times

The surface morphology and microstructure of as-deposited TiO_2 was examined on Si_3N_4 substrates. The deposition temperatures were 400 to 500°C. The precursor concentration and injection volume were kept constant at 0.15 mol% and 50 μl, respectively. The base pressure was held at 100 Pa when the relaxation time was varied, and the relaxation time was maintained at 0 sec when the base pressure was adjusted. The base pressure was varied in the range of 50 to 200 Pa, and the relaxation time was from 0 to 10 sec. The deposited TiO_2 thin films had thicknesses of 245 to 440 nm, and the number of pulses was in the range of 88 to 168 pulses.

Figure 4-20 shows the surface morphology and microstructure of the deposited TiO_2 on Si_3N_4 substrate at the deposition temperature of 450°C at various base pressures. The SEM images of cross-sections of fracture surfaces of TiO_2 show that the deposited TiO_2 thin films have a crystalline structure with columnar microstructures. The base pressure has no noticeable effects on the surface microstructure from the SEM images. The base pressure has minor effects on the growth rate of the thin TiO_2 films on Si_3N_4 substrates as discussed in Section 4.2.2.

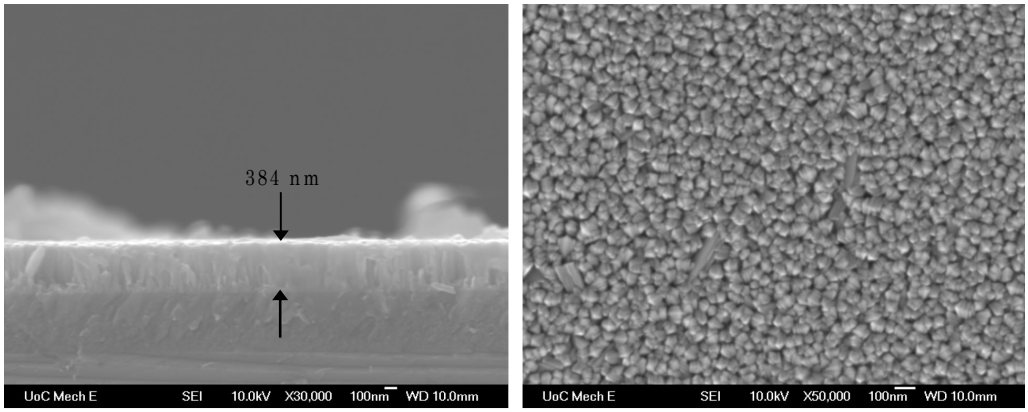

(a) Base Pressure: 50 Pa; No. of Pulses: 128

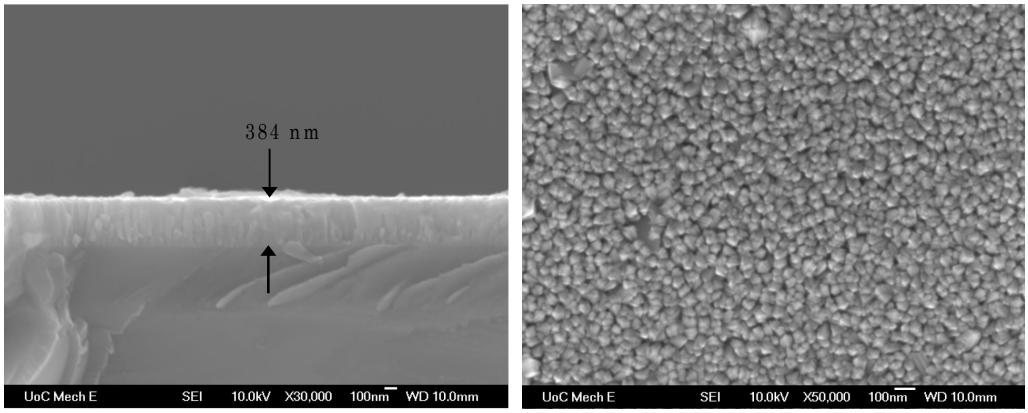

(b) Base Pressure: 100 Pa; No. of Pulses: 151

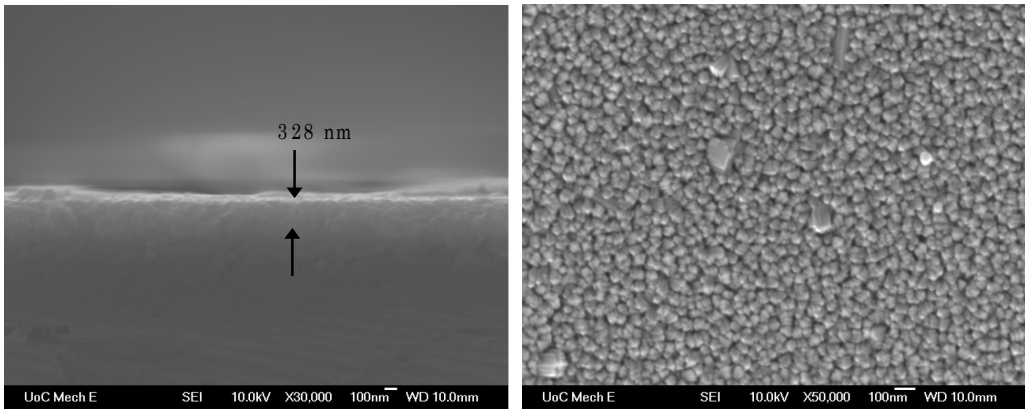

(c) Base Pressure: 200 Pa; No. of Pulses: 119

Figure 4-20: SEM images of cross-sections of a fracture surface at 30,000x magnification (left) and surface micrographs at 50,000x magnification (right) of deposited TiO_2 thin films on Si_3N_4 substrates at 450°C and various base pressures with the number of pulses between 91 and 151 pulses. The deposited films were columnar and there were no influences of base pressure on grain sizes.

(T = 450°C, P_{min} = 100-200 Pa, C_{mo} = 0.15 mol%, ν_L = 50 µl, t = 10 sec)

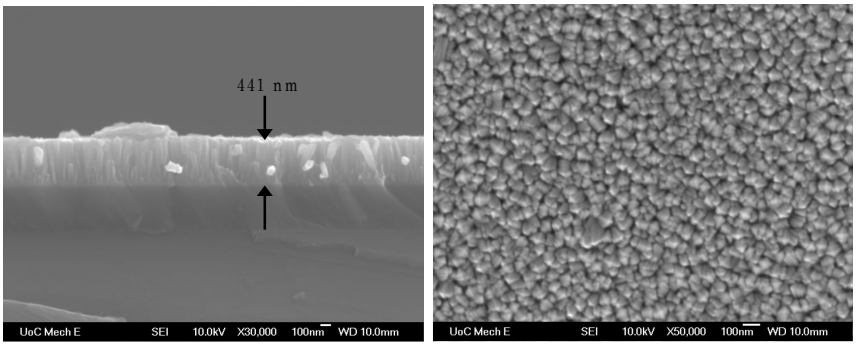

(a) Relaxation Time: 0 sec; No. of Pulses: 168

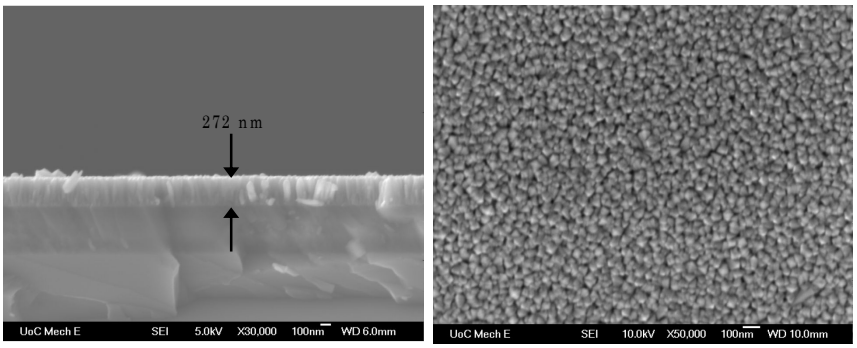

(b) Relaxation Time: 2.5 sec; No. of Pulses: 94

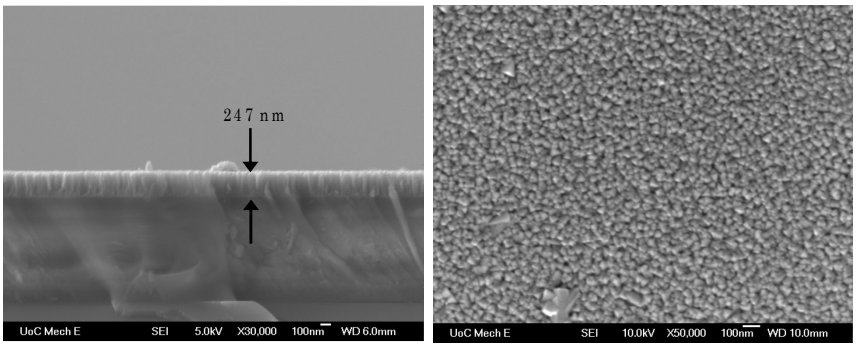

(c) Relaxation Time: 5 sec; No. of Pulses: 115

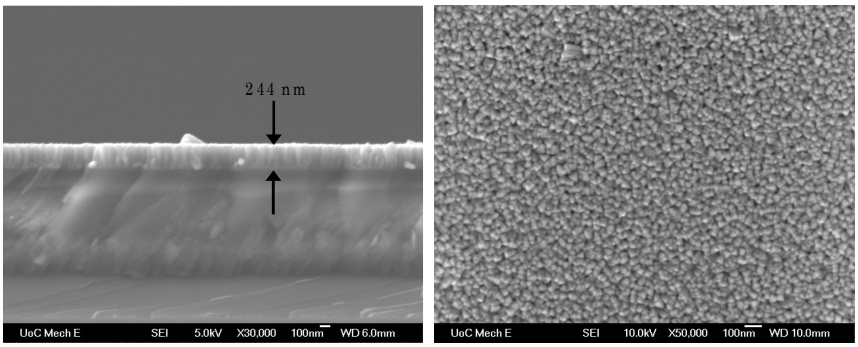

(d) Relaxation Time: 10 sec; No. of Pulses: 116

Figure 4-21: SEM images of cross-sections of a fracture surface at 30,000x magnification (left) and surface micrographs at 50,000x magnification (right) of deposited TiO_2 thin films on Si_3N_4 substrates at 500°C and various relaxation times with the number of pulses in the range of 94 to 168 pulses. The grain sizes tended to be independent on relaxation time.

(T = 500°C, P_{min} = 100 Pa, C_{mo} = 0.15 mol%, ν_L = 50 µl, t = 10-20 sec)

Figure 4-21 illustrates SEM images of cross-sections of fracture surfaces and surface morphology of deposited TiO_2 films on Si_3N_4 substrate at the deposition temperature of 500°C with various relaxation times. Surface morphology at the relaxation time of 0 sec was different from the surface morphology at other relaxation times. The number of pulses and the thickness of the deposited films might affect the surface morphology of the films. The relaxation time has no obvious effects on surface microstructure and morphology at other relaxation times. The relaxation time had slight effects on the growth rate of the deposited TiO2 thin films on Si_3N_4 substrates as described in Section 4.2.5.

There was some particle contamination that was non-crystalline on the film surface with both varied base pressures and relaxation times. Those particles could come from handling after deposition because the experiments were carried out in normal laboratory conditions. The substrate preparation and lithography were carried out in an ambient 10k laboratory.

4.4.3. Surface Morphology and Microstructure of Deposited TiO_2 at Various Precursor Concentrations and Injection Volumes

The influences of precursor concentration and precursor injection on surface morphology and microstructure of as-deposited TiO_2 were examined on Si_3N_4 substrates with 300 and 500 nm structures and aspect ratios of 1:1 and 1:2. The deposition temperatures were held at 400 and 500°C because conformality was

expected to be poor at the deposition temperature of 600°C. The precursor concentrations were 0.15, 0.25 and 0.50 mol%. The injection volumes were in the range of 50 to 250 µl. The base pressure and relaxation time were kept constant at 100 Pa and 0 sec, respectively. The deposited TiO_2 thin films had thicknesses of 90 to 250 nm with the number of pulses ranging from 58 to 382 pulses. There was an attempt to maintain the thicknesses at approximately 200 nm; however, thinner films occurred because the precursor ran out.

Figure 4-22 illustrates surface morphology and crystal microstructure using SEM on the fracture surfaces of the deposited TiO_2 on Si_3N_4 with 300 nm patterns size and an aspect ratio of 1:2 at the deposition of 500°C with various injection volumes. The deposited films showed crystalline columnar structure. There was no evident effect of the injection volume on the microstructure of the deposited thin films. There was a growth pattern on the surface at the top of the trench at the precursor injection volume of 50 and 100 µl. This might be due to impurities on the surface of the Si_3N_4 substrate that assisted the flower-like growth structure, as the base pressure and relaxation time that affected the exposure did not show any similar crystal structure.

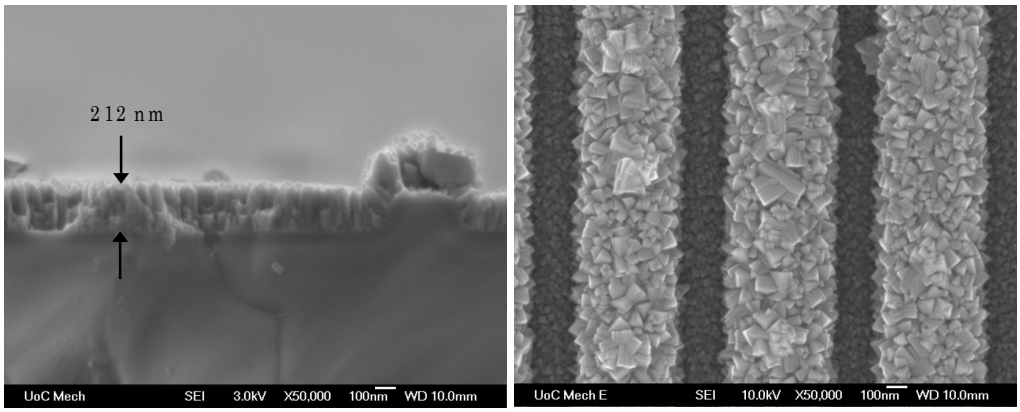

(a) Injection Volume: 50 µl; No. of Pulses: 269

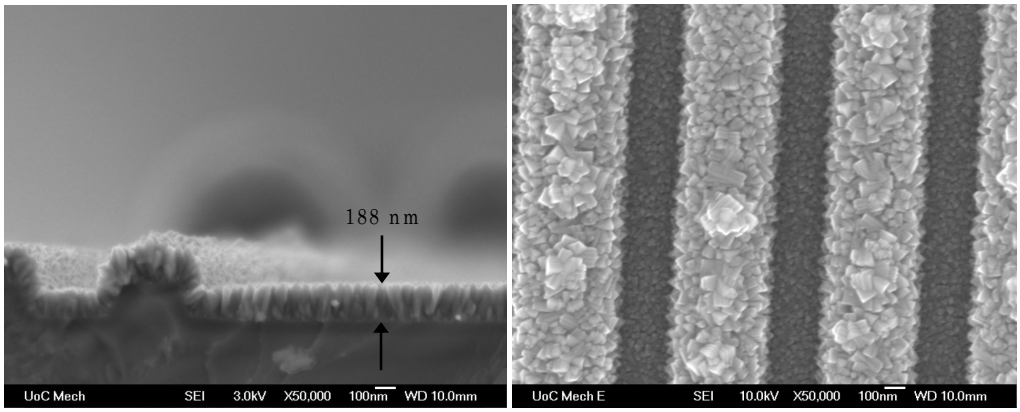

(b) Injection Volume: 100 µl; No. of Pulses: 109

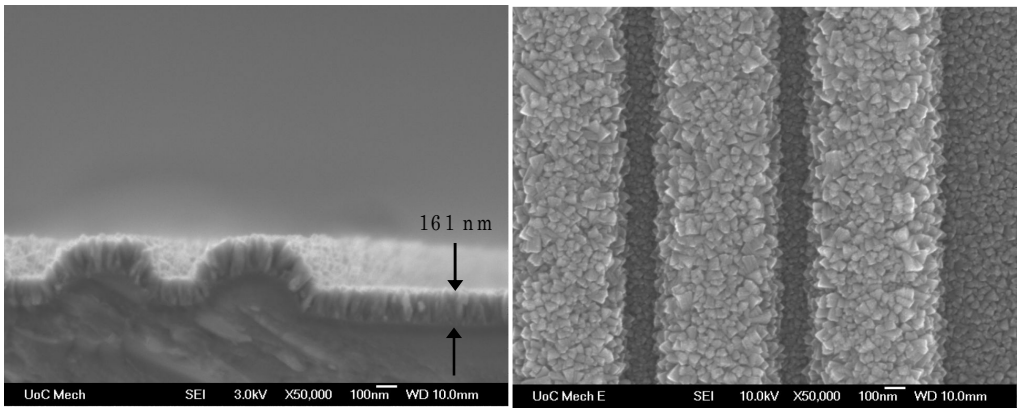

(c) Injection Volume: 250 µl; No. of Pulses: 58

Figure 4-22: SEM images of surface micrographs at structured surfaces showing a flower-like microstructure (right) and cross-sections of a fracture surface (left) at 50,000x magnification of deposited TiO_2 thin films on Si_3N_4 substrates with features at 500°C and various injection volumes. The features were 300 nm with a 1:2 aspect ratio.

(T = 500°C, P_{min} = 100 Pa, C_{mo} = 0.15 mol%, ν_L = 50-250 µl, t = 10 sec)

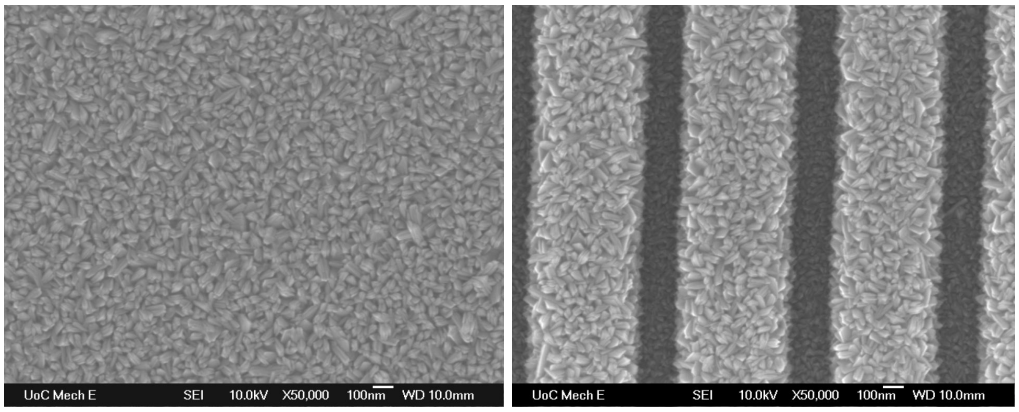

(a) Precursor Concentration: 0.15 mol%; Aspect Ratio: 1:2

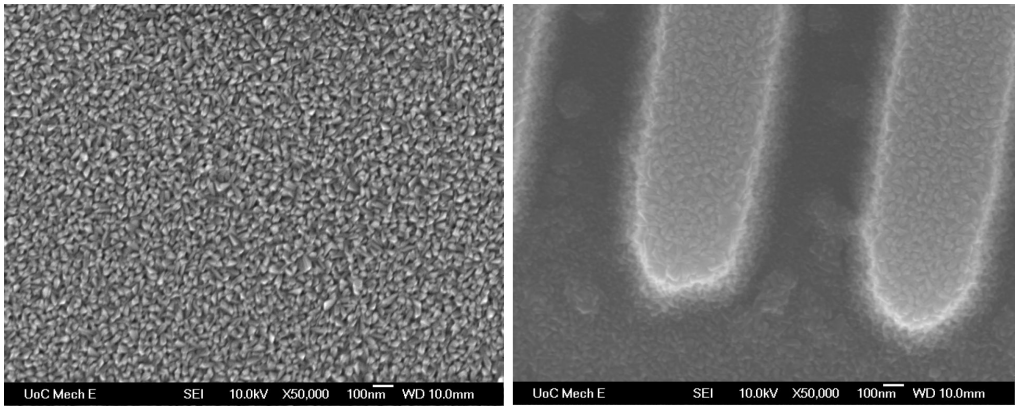

(b) Precursor Concentration: 0.25 mol%; Aspect Ratio: 1:1

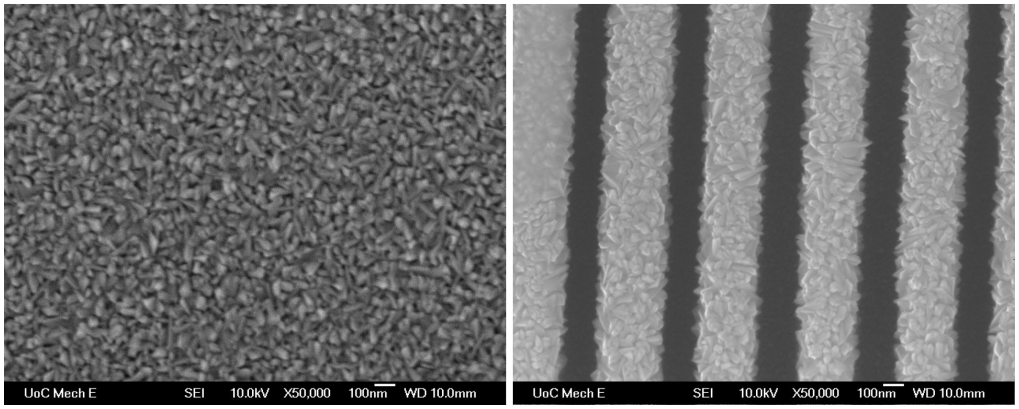

(c) Precursor Concentration: 0.50 mol%; Aspect Ratio: 1:1

Figure 4-23: SEM images of surface micrographs on the flat area (left) and patterned area (right) at 50,000x magnification of deposited TiO_2 thin films on Si_3N_4 substrates with features at 400°C and various precursor concentrations. The feature sizes were 300 nm at the precursor concentration of 0.50 mol%. The feature size was 500 nm at the precursor concentration of 0.15 and 0.25 mol%. The aspect ratios were as stated.

(T = 400°C, P_{min} = 100 Pa, C_{mo} = 0.15-0.50 mol%, v_L = 50 µl, t = 10 sec)

Figure 4-23 shows the surface structure of deposited TiO_2 on a flat and patterned area on the feature sizes of 300 and 500 nm with aspect ratios of 1:1 and 1:2 at the deposition of 400°C with different precursor concentrations. The precursor concentration had minor influences on the surface microstructure. As shown in Section 4.1, peak pressure, which influences nucleation and film growth (Ramirez et al., 2008), was not affected by the precursor concentration in this study.

The results of these investigations show that the base pressure, precursor concentration, injection volume and relaxation time tended not to affect the surface morphology and microstructures of the deposited TiO_2 at the same deposition temperature. This could imply that the pulse exposure does not obviously affect the surface morphology and microstructures. The deposition temperature played the most important role in the surface morphology and microstructures of the deposited TiO_2 thin films in this study.

4.5. Phase of Deposited TiO_2 Thin Film

Phase analysis of the thin film is necessary as it influences the film quality as well as its applications. The phase of as-deposited TiO_2 thin films will be discussed in this section.

4.5.1. Composition of Deposited TiO_2 by Energy Dispersive X-ray Spectroscopy

According to the qualitative analysis of the composition of deposited films using energy dispersive X-ray spectroscopy (EDS), the main composition of the deposited films is Ti, O and Si as expected.

Figure 4-24 illustrates a composition analysis from EDS. The TiO_2 film was 340 nm thick, and the estimated ratio of Ti and O from the composition percentage calculated by EDS was 1:2. The composition of the substrate, Si, was found because the deposited TiO_2 film was thin. It should be noted that the carbon peak was integrated with O and Ti peaks. In certain cases when the crystal structures were similar to TiO_2, it was assumed the carbon peak did not exist in the deposited film.

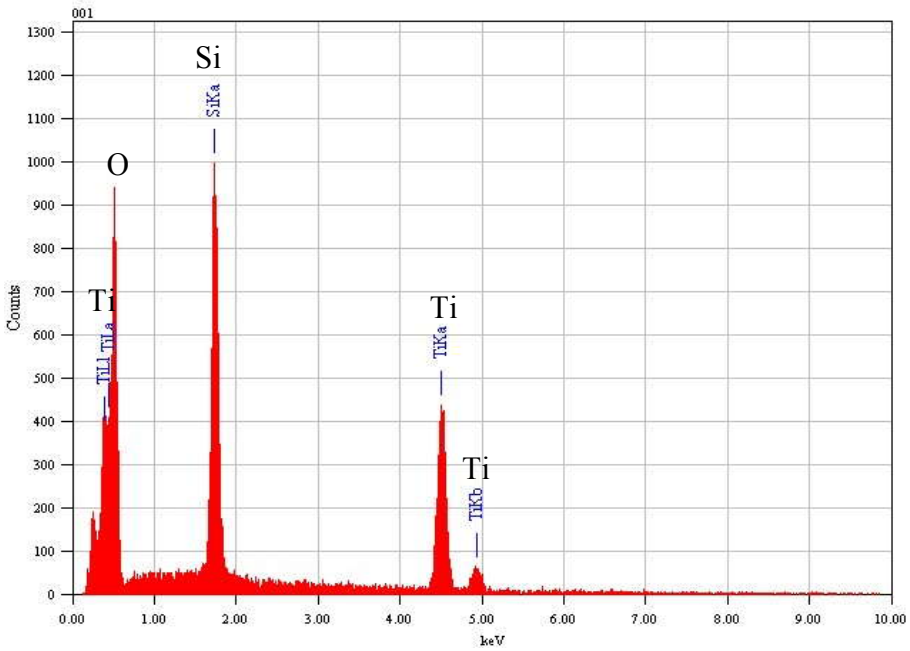

Figure 4-24: An example of the EDS analysis of the composition of deposited films from TTIP by PP-MOCVD.

(T = 500°C, P_{min} = 100 Pa, C_{mo} = 0.50 mol%, ν_L = 100 µl, t = 10 sec)

4.5.2. Phase of Deposited TiO_2 by Raman Spectroscopy

Raman spectroscopy was applied to analyse the phase of as-deposited TiO_2 thin films as a function of the deposition temperature. The TiO_2 films were deposited on micro-scale structures of Si_3N_4 substrates at deposition temperatures between 400 and 600°C. The base pressure, precursor concentration, precursor injection volume and relaxation time were kept constant at 100 Pa, 0.50 mol%, 100 µl and 0 sec, respectively.

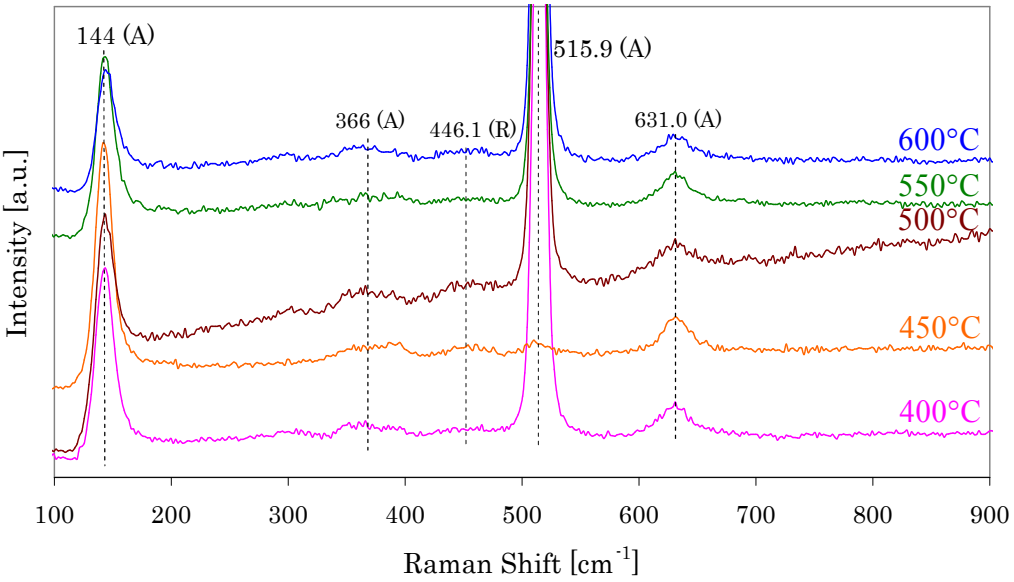

Figure 4-25: The Raman analysis of deposited TiO_2 films as a function of temperature showing mainly anatase phase. (A) represents anatase phase and (R) means rutile phase.

(T = 400-600°C, P_{min} = 100 Pa, C_{mo} = 0.50 mol%, v_L = 100 µl, t = 10 sec)

Figure 4-25 shows the analysis from Raman spectroscopy of as-deposited TiO_2 films at various deposition temperatures. The intensity of the Raman signals is not included. The Raman is meant to be used for phase comparison in this case, and the Raman spectra showed a mixture of anatase and rutile with major anatase phase peaks and a very weak rutile peak. The deposition temperature in the range studied had no effect on the phase of deposited TiO_2.

In general, rutile is more thermodynamically stable than anatase; hence it is commonly found at a high deposition temperature and low precursor concentration. The growth rate is not limited by surface reaction but by diffusion mass transport in those conditions. The anatase phase is normally found at a low deposition temperature and high precursor concentration or when the growth rate is limited by surface kinetics (Duminica et al., 2007). The deposition temperature in this study was low and showed surface kinetics limited at the deposition temperature of 400°C, hence the anatase phase was shown.

The thickness of the deposited films also influences the phase of the TiO_2 films. Anatase is usually observed when the film is less than 10 micron (Seifried et al., 2000). In the present study, the deposited TiO_2 films were in the range of 100 to 300 nm except for certain films that had a thickness of 2.5 to 3.5 microns. The thicknesses of deposited films were less than 10 microns, and therefore the phase of deposited TiO_2 in this case was mainly anatase.

4.5.3. Phase of Deposited TiO_2 by X-ray Diffraction

Two of the as-deposited TiO_2 thin films from Raman spectroscopy analysis were chosen for X-ray diffraction (XRD) analysis. As mentioned before, the deposited TiO_2 thin films were made on micro-scale patterns of Si_3N_4 substrates at deposition temperatures between 400 and 600°C under the base pressure of 100 Pa. The precursor concentration, injection volume and relaxation time were 0.50 mol%, 100 μl and 0 sec, respectively. The as-deposited TiO_2 films had thicknesses of 237 nm at the deposition temperature

of 400°C and 192 nm at the deposition temperature of 600°C. The phase analysis from XRD agreed with Raman that the as-deposited TiO_2 was anatase.

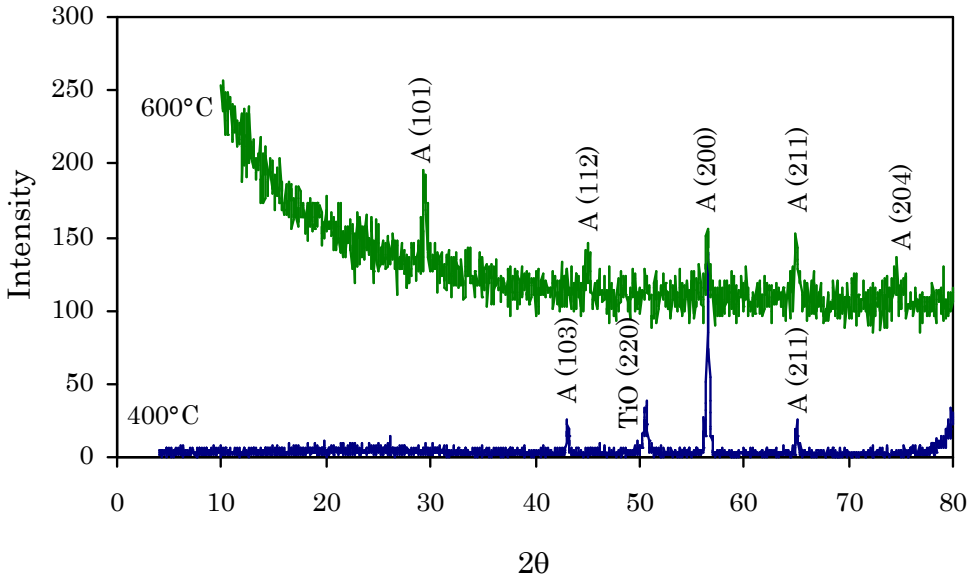

Figure 4-26: The XRD analysis of deposited TiO_2 thin films showing an anatase phase at the deposition temperature of 400 and 600°C. (A) represents anatase phase.

(T = 400, 600°C, P_{min} = 100 Pa, C_{mo} = 0.50 mol%, v_L = 100 µl, t = 10 sec)

Figure 4-26 shows the XRD analysis of as-deposited TiO_2 films at the deposition temperature of 400 and 600°C. As illustrated in Figure 4-26, certain peaks of anatase TiO_2 at the deposition temperature of 400°C were missing and one unmatched peak appeared. The missing peaks could possibly be because of the alignment of the anatase TiO_2. The unmatched peak might be titanium oxide (TiO) (220) that occurred from the decomposition mechanism of TTIP at a low temperature. Additional study needs to be carried out to explain if the unmatched peak is TiO and how it is formed. The difference in the thickness of the deposited films caused the difference in X-ray intensity.

The influence of precursor injection volume and relaxation time on the phase of TiO_2 was studied using as-deposited TiO_2 on Si_3N_4 substrates. The injection

volumes were 50 and 250 μl at the relaxation time of 0 sec. The relaxation time was varied at 5 and 10 sec with a constant injection volume of 100 μl. The deposition temperature, base pressure and precursor concentration were kept constant at 400°C, 100 Pa and 0.15 mol%, respectively.

Figure 4-27 illustrates the XRD analysis of as-deposited TiO_2 on Si_3N_4 substrate at a precursor injection volume of 50 and 250 μl. The films had thicknesses of 180 and 187 nm for injection volumes of 50 and 250 μl, respectively. The intensities of the peaks of both injection volumes were very close. The graph does not show the real intensity in order to separate the two data for phase comparison.

Figure 4-28 shows the phase of as-deposited TiO_2 on Si_3N_4 at the relaxation times of 5 and 10 sec. The deposited film at the relaxation time of 5 sec has higher intensity than the relaxation time of 10 sec because of the difference in film thicknesses. The thickness of the film deposited at the relaxation time of 5 sec was 281 nm while it was 197 nm at the relaxation time of 10 sec. The (112) peak was missing for the relaxation time of 10 sec. This could be because of the lower peak intensity for the deposition at the relaxation time of 10 sec than for the relaxation time of 5 sec.

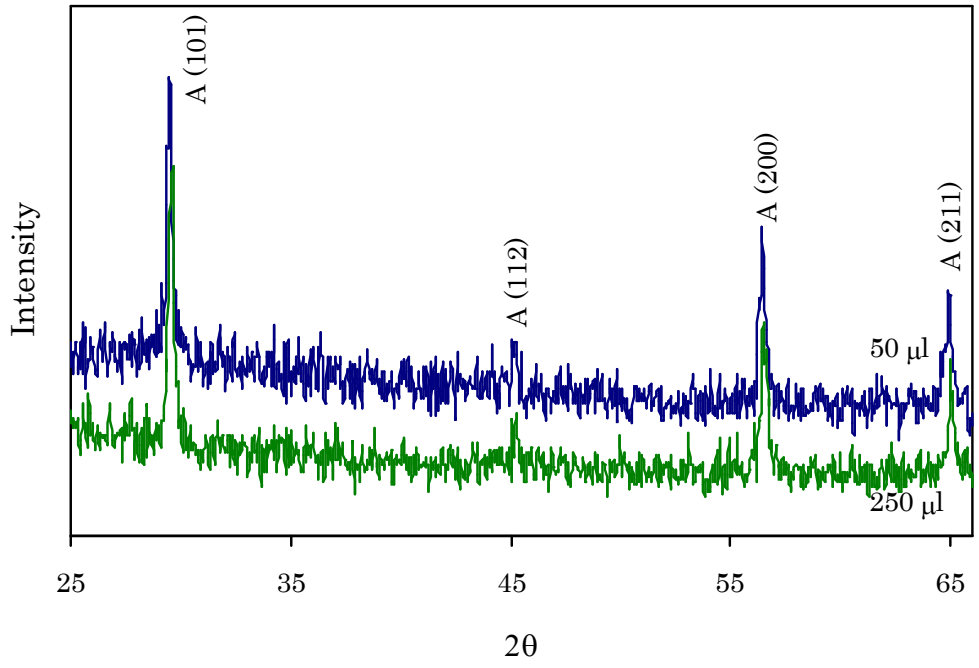

Figure 4-27: The XRD analysis of deposited anatase TiO_2 thin films at 50 and 250 µl injection volume. (A) represents anatase phase.

(T = 400°C, P_{min} = 100 Pa, C_{mo} = 0.15 mol%, ν_L = 50, 250 µl, t = 10 sec)

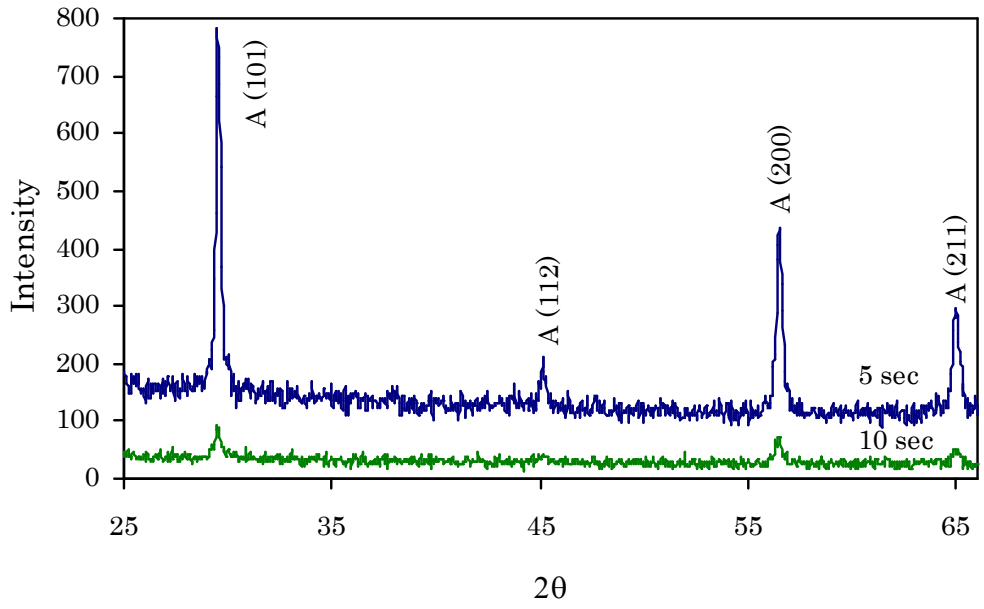

Figure 4-28: The XRD analysis of deposited anatase TiO_2 thin films 5 and 10 sec relaxation time. (A) represents anatase phase.

(T = 400°C, P_{min} = 100 Pa, C_{mo} = 0.15 mol%, ν_L = 50 µl, t = 15, 20 sec)

The as-deposited TiO_2 films were shown to be anatase phase for both the varied precursor injection volume and relaxation time. The injection volume and relaxation time had no noticeable effect on the phase of the deposited TiO_2 at the deposition conditions in the range studied. The width of the peaks from XRD was similar. This implied the similarity of, for example, crystallographic orientation, impurities and crystal size.

Because the deposited films were less than 10 μm, the deposited films were anatase. The injection volume and relaxation time affected the peak pressure as discussed in Section 4.2. Peak pressure influences nucleation and growth, and there might be phase or crystallographic orientation change when the film becomes thicker than in this study.

4.6. Grain Size and Surface Roughness of Deposited TiO_2 Thin Film

The planar Si_3N_4 substrates were used for grain size and surface roughness analysis. The influences of deposition temperature, base pressure and relaxation time were investigated. Figure 4-29 illustrates an example of an AFM image that was used to calculate the roughness and grain size of the deposited TiO_2. The film was deposited at 500°C, base pressure of 100 Pa and pulsing time of 12.5 sec.

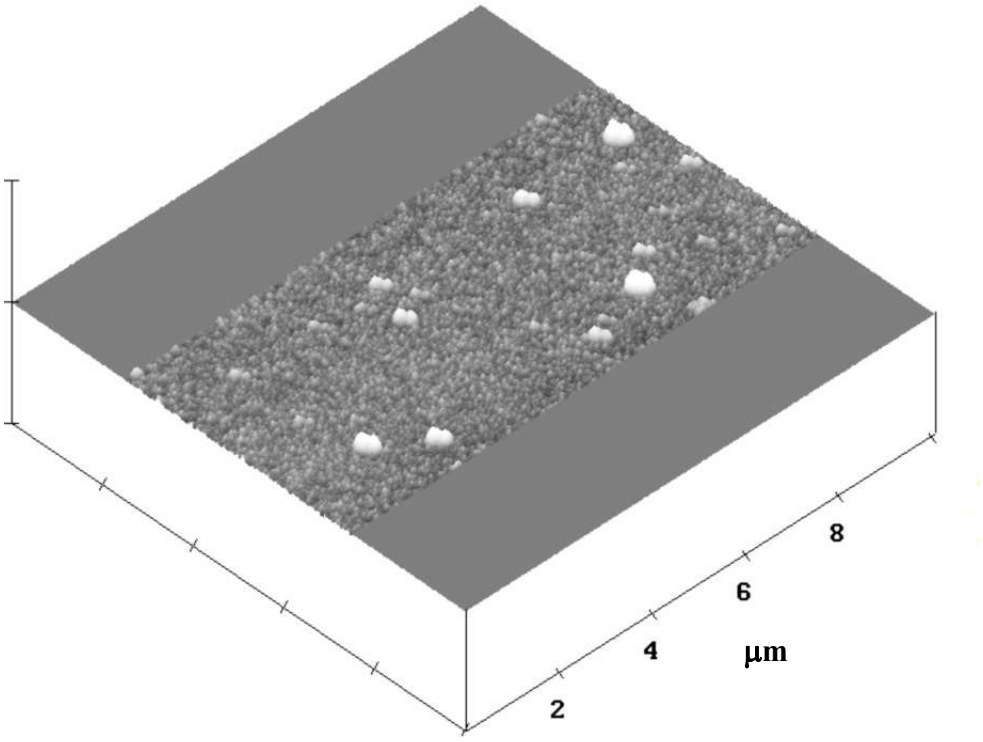

Figure 4-29: An example of a deposited TiO_2 3-D image from AFM applied to calculate the surface roughness and grain size.

(T = 500°C, P_{min} = 100 Pa, C_{mo} = 0.15 mol%, v_L = 50 µl, t = 12.5 sec)

4.6.1. Influence of Temperature on Roughness and Grain Size

The influence of temperature on surface roughness and grain size was investigated on non-structured Si_3N_4 substrates. The deposition temperature was varied between 400 and 500°C. The base pressure, precursor concentration, injection volume and relaxation time were maintained at 100 Pa, 0.15 mol%, 50 µl and 0 sec. The roughness was in the range of 3.8 to 6.4 nm with 1.3 nm standard deviation. The grain size was between 80 and 105 nm with the standard deviation of 15 nm. The grain size of the deposited TiO_2

films according to XRD using the Scherer equation was 22±6 nm at the deposition temperature of 400°C and 40±5 nm for the deposition temperature of 600°C.

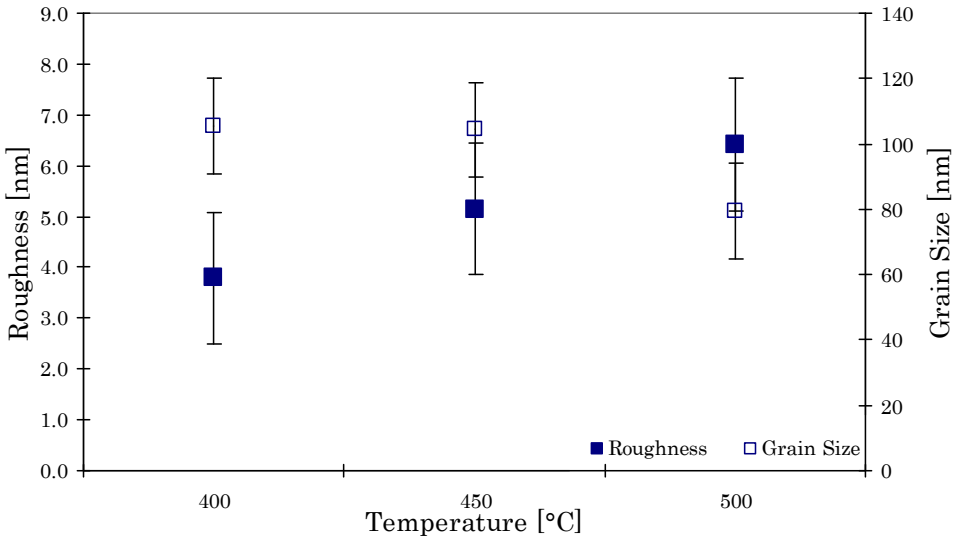

Figure 4-30: The roughness increased while the grain size decreased as the deposition temperature increased.

(T = 400-500°C, P_{min} = 100 Pa, C_{mo} = 0.15 mol%, ν_L = 50 µl, t = 10 sec)

Figure 4-30 illustrates the roughness and grain size of deposited TiO_2 at the deposition temperature of 400 to 500°C. The grain size decreased as the temperature increased. The grain size of the TiO_2 at higher deposition temperature was smaller than at lower deposition temperature. This was observable in Figure 4-19 with the precursor concentration of 0.50 mol% and 100 µl injection volume. The variation in grain size with temperature agreed with the study of Krumdieck et al. where the grain size at higher deposition temperatures should be smaller, as fully dense films are formed because of the faster growth rate (Krumdieck and Raj, 2001b).

The grain size calculated from the Scherer equation using the data from XRD was different from AFM. It was larger at the deposition temperature of 400°C than at 600°C. This might be because of the variation in calculation due to the different intensity, hence the FWHM value. According to Figure 4-26, it appears that the X-ray diffraction peaks at the deposition temperature of 400°C were sharper than at 600°C. A larger grain size is expected when the peaks from XRD are sharper.

As can be seen in Figure 4-30, the roughness increased as the deposition temperature increased. Deposited films tended to be smoother as the grain size increased.

4.6.2. Influence of Base Pressure on Roughness and Grain Size

The influence of base pressure on surface roughness and grain size was investigated on planar Si_3N_4 substrates. The base pressure was varied between 50 and 200 Pa and the deposition temperatures were at 400 to 500°C. The precursor concentration, injection volume and relaxation time were kept constant at 0.15 mol%, 50 μl and 0 sec. The roughness was in the range of 2.5 to 6.4 nm with the average standard deviation of 1.3 nm. The grain size was between 60 and 330 nm with the standard deviation of 15 to 110 nm.

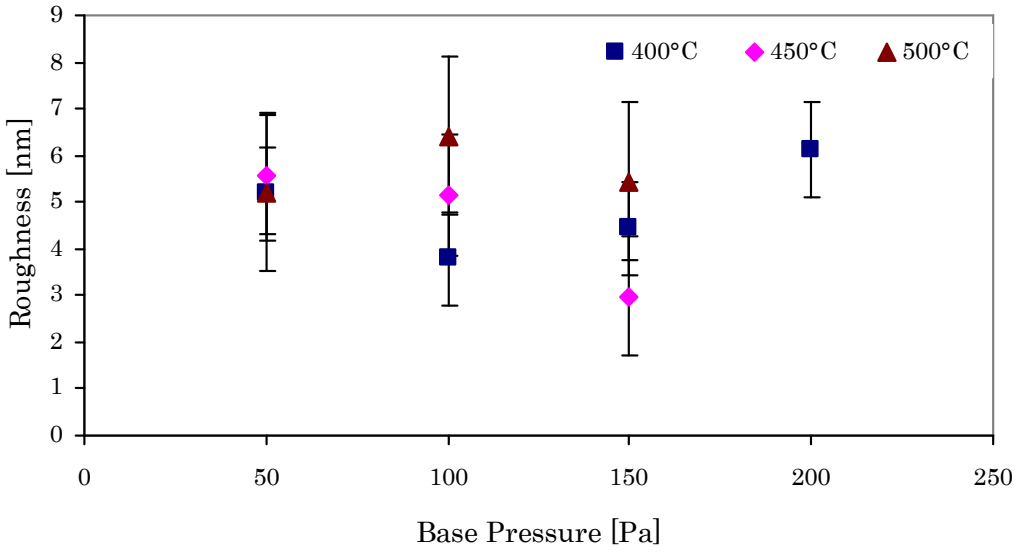

Figure 4-31: Base pressure showed minor influences on surface roughness of the as-deposited TiO_2 thin films on Si_3N_4 substrates.

(T = 400-500°C, P_{min} = 50-200 Pa, C_{mo} = 0.15 mol%, ν_L = 50 µl, t = 10 sec)

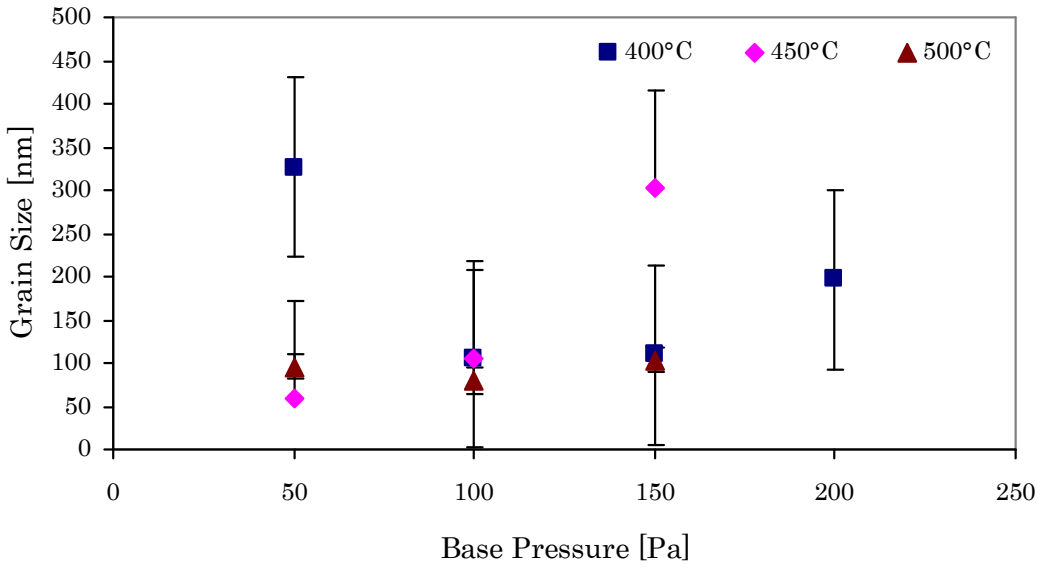

Figure 4-32: Base pressure showed minor influences on grain size of the as-deposited TiO_2 thin films on Si_3N_4 substrates.

(T = 400-500°C, P_{min} = 50-200 Pa, C_{mo} = 0.15 mol%, ν_L = 50 µl, t = 10 sec)

Figure 4-31 shows the roughness and grain size at the deposition temperature of 400 to 500°C over the range of base pressures. The grain size and roughness were fairly constant as the base pressure increased with high standard deviation at the deposition temperature of 500°C. The high standard deviation was attributed to the large crystals on the deposited film surface. The grain size was independent of base pressure between 100 and 200 Pa, and the roughness was not affected by base pressure at the deposition temperature of 400°C. The grain size increased and the roughness decreased as the base pressure increased at the deposition temperature of 450°C. Certain data points were omitted for the same reasons as discussed in the previous sections.

The changing of base pressure alone did not show any obvious effect on growth rate at the deposition temperatures of 400 to 500°C. It has been reported that the growth rate influences surface morphology and crystal orientation (Chen et al., 2004). Because the base pressure has minor effects on growth rate and surface morphology, the grain size and roughness varied slightly with the base pressure at the deposition temperatures of 400 and 500°C. The grain size according to SEM images in Figure 4-20 showed no noticeable difference as the base pressure increased.

The effect of base pressure on grain size and roughness at the deposition temperature of 450°C requires further investigation as the base pressure has no effect on growth rate and surface morphology in PP-MOCVD.

4.6.3. Influence of Relaxation Time on Roughness and Grain Size

The influence of relaxation time on surface roughness and grain size was investigated on non-structured Si_3N_4 substrates. Relaxation time was varied between 0 and 10 sec. Deposition temperatures were at 400 to 500°C. The base pressure, precursor concentration and injection volume were maintained at 100 Pa, 0.15 mol% and 50 µl. Roughness was in the range of 3.8 to 6.4 nm with 0.4 to 1.3 nm standard deviation. Grain size was between 50 and 125 nm with the standard deviation of 10 to 25 nm. The grain size calculated using the Scherer equation was 26±5 nm for the relaxation time of 5 sec and 30±8 nm for the relaxation time of 10 sec.

Figure 4-33 shows the surface roughness and grain size at deposition temperatures of 400 to 500°C with the pulsing time in the range of 10 to 20 sec. Considering the grain size and surface roughness as a function of relaxation time, grain size and roughness were independent of relaxation time. The calculated grain sizes from the Scherer equation were slightly different. As discussed in Section 4.6.1, the intensity of the X-ray diffraction at the relaxation time of 5 sec was higher than the relaxation time of 10 sec.

According to Figure 4-21, it appeared that the grain size slightly decreased as the relaxation time increased. This might be because of the difference in the deposited film thicknesses, which caused the slight variation in SEM images at the same magnification.

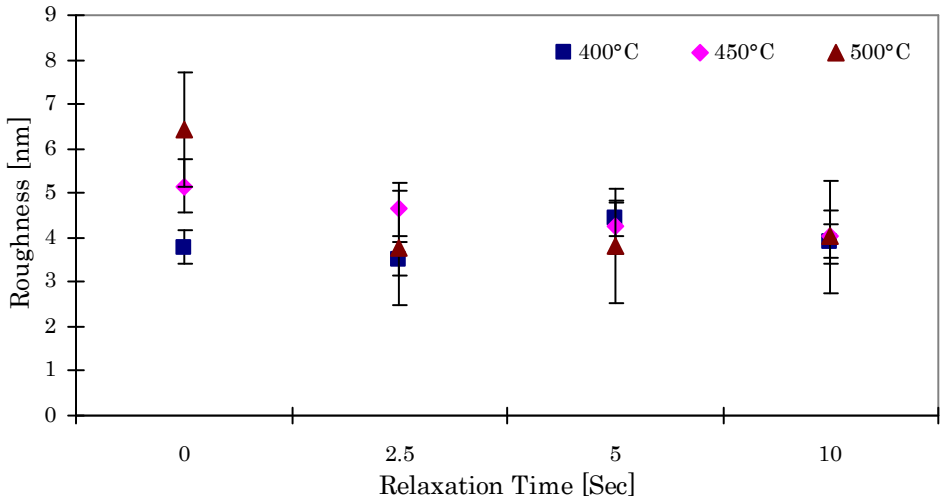

Figure 4-33: The surface roughness of deposited TiO_2 films was independent of relaxation time.

(T = 400°C, P_{min} = 100 Pa, C_{mo} = 0.15 mol%, v_L = 50 µl, t = 10 sec)

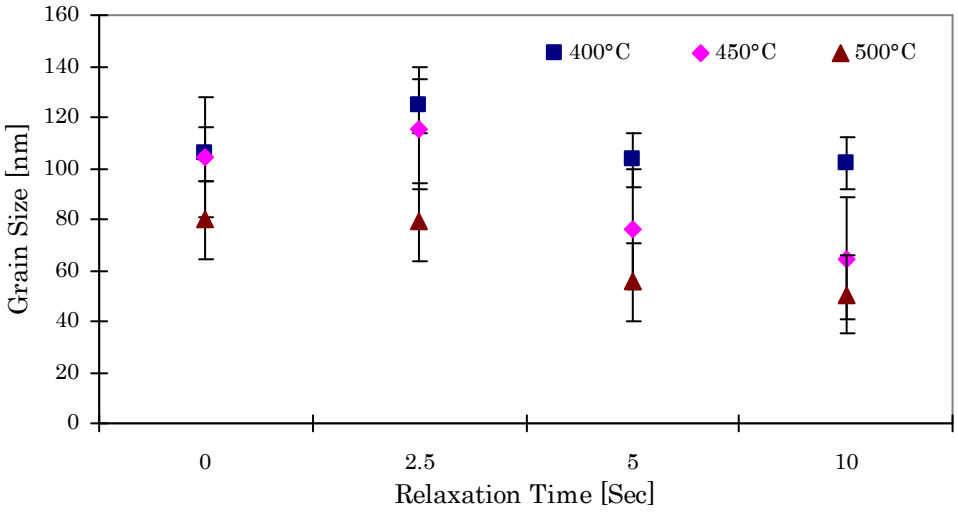

Figure 4-34: The grain size of deposited TiO_2 films was independent of relaxation time.

(T = 400°C, P_{min} = 100 Pa, C_{mo} = 0.15 mol%, v_L = 50 µl, t = 10 sec)

Pulse exposure variation when precursor concentration and injection volume are constant has a minor effect on roughness and grain size. The calculated grain sizes using the Scherer equation of deposited TiO_2 films at the injection volumes of 50 and 250 µl were the same at 15±3 nm. This indicated that surface kinetics was the rate limiting step at a deposition temperature of 400°C

because the precursor supply rate has less effect on the surface morphology of deposited films.

4.7. Optical Properties of Deposited TiO_2 Thin Film

The optical properties especially UV-Visible transmission are important for many applications as UV light must be able to pass through the mould and resist. The resist is normally exposed to UV light. The energy band gap and refractive index are studied in this section for anatase TiO_2 deposited at the deposition temperatures of 400 and 500°C, base pressure of 100 Pa, precursor concentration of 0.15 mol%, injection volume between 50 to 250 μl and relaxation time of 0 sec.

Figure 4-35 illustrates an example of the transmission of deposited TiO_2 on quartz at the deposition temperature of 500°C, base pressure of 100 Pa, precursor concentration of 0.15 mol%, 100 μl injection volume and pulsing time of 10 s. The transmission in the range of UV-Visible of as-deposited TiO_2 was over 55% for the film thickness in the range of 160 to 250 nm. Using the envelope method for the UV-VIS spectra of a deposited TiO_2 film as written as Equations (3-4) and (3-5), the refractive index for the anatase phase was found to be 2.2.

Figure 4-36 shows an example of the plot between $(\alpha(h\nu))^2$ and $h\nu$ to find the energy band gap according to Equation (3-6). The band gap of 3.7 eV was found.

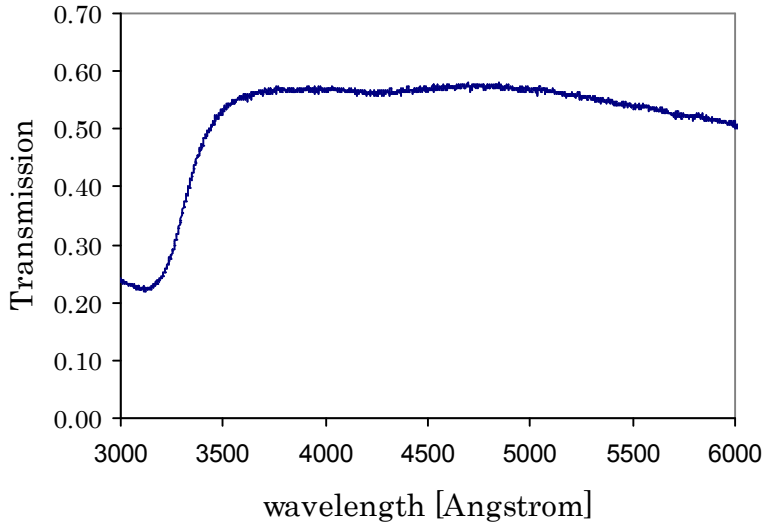

Figure 4-35: The transmission of a deposited TiO_2 thin film.
(T = 500°C, P_{min} = 100 Pa, C_{mo} = 0.15 mol%, ν_L = 100 µl, t = 10 sec)

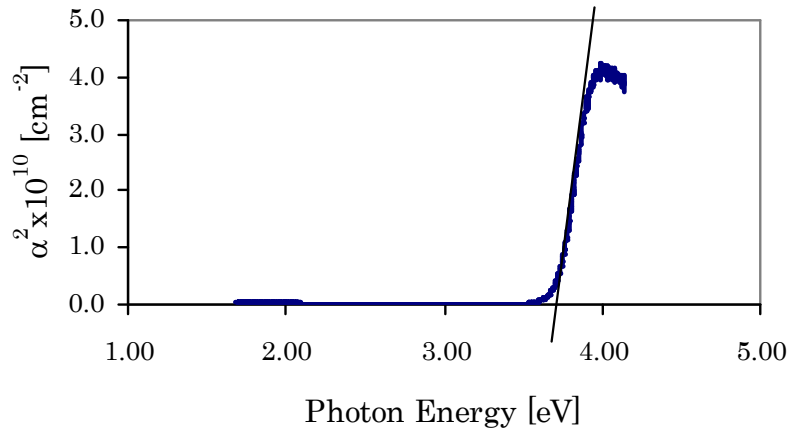

Figure 4-36: An example of the plot between the square of absorption coefficient $(\alpha(h\nu))^2$ and photon energy ($h\nu$) for energy band gap estimation.
(T = 500°C, P_{min} = 100 Pa, C_{mo} = 0.15 mol%, ν_L = 100 µl, t = 10 sec)

The thicknesses used to calculate the refractive index and energy band gap were from Si_3N_4 as it was not possible to measure the thicknesses from quartz at this point. Figure 4-37 shows an SEM image of deposited TiO_2 on quartz. The surface morphology appears to be similar to the deposited TiO_2 on Si_3N_4 as illustrated in Figure 4-22 (b) under the same deposition conditions.

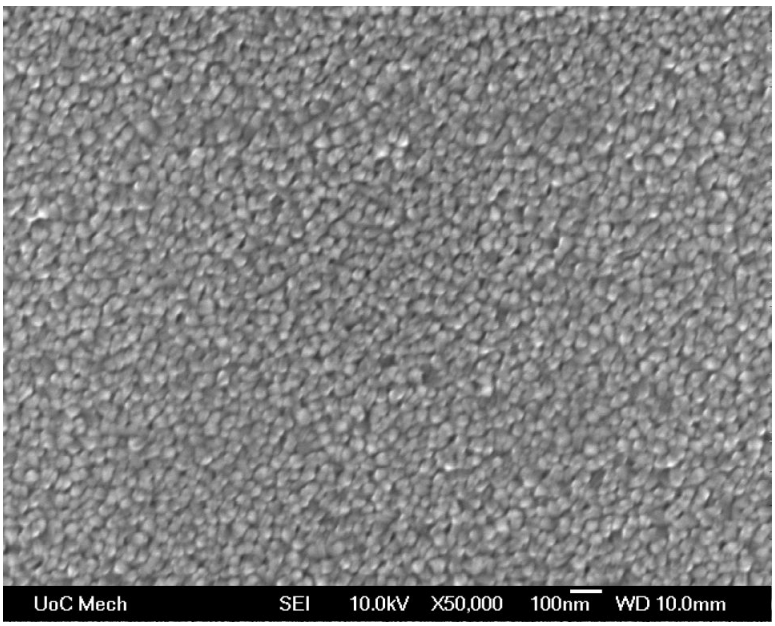

Figure 4-37: SEM images at 50,000x magnification of as-deposited TiO_2 on quartz that was used for UV-VIS transmission and band gap analysis.

Table 4-2 shows the energy band gap obtained from the plot as shown in Figure 4-36 at various as-deposited TiO_2 film thicknesses. The deposited TiO_2 on Si_3N_4 has the thickness in the range of 159 to 252 nm with the energy band gap, according to the transmission of deposition of TiO_2 on quartz, between 3.65 to 3.71 eV.

Table 4-2: The energy band gap at various deposited TiO_2 film thicknesses.

Deposited TiO_2 Thickness [nm]	Energy Band Gap [eV]
159	3.65
160	3.71
180	3.68
187	3.70
252	3.66

The refractive index of the anatase phase TiO_2 of 2.2 in this study compares well with the reference values from Sankapal et al. and Clark et al., which is 2.54 (Clark et al., 1975; Sankapal et al., 2005). The energy band gap from this study, 3.65 to 3.71 eV, was up to approximately 0.4 eV higher compared with the reference value from Sankapal et al. and Kitazawa et al. of 3.2 eV for the anatase phase (Kitazawa et al., 2006; Sankapal et al., 2005). Nevertheless, the energy band gap of the anatase from Bernardi et al. and Park et al. was found to be in the range of 3.6 to 3.8 eV (Bernardi et al., 2001; Park and Kim, 2005). This was in agreement with the energy band gap found in this study. The deviation of the refractive index and energy band gap might be due to the difference in microstructure of the deposited films, thicknesses and the quality of the substrates, which affected the refractive index and transmission used to calculate the refractive index and energy band gap.

4.8. Measurement Accuracy

Certain errors have been described in this study because they could explain the results as well as being used to improve on them and minimise the errors. There was no maximum requirement in this study but there was an attempt to minimise all possible experimental errors.

4.8.1. Temperature

A high degree of variation in temperature and pressure was observed during the first five pulses because of temperature and pressure fluctuation. The error in temperature measurement could result from the thermocouple, digital

thermocouple reading, variation of the heat source from the controlling unit, location of the thermocouple and the temperature difference between the thermocouple reading and the substrate. Two type K thermocouples were used in this study and have temperature accuracy between ±3.0 and ±4.5°C in the deposition temperature range. The uncertainty from the reading of the digital thermocouple was 0.01°C.

The thermocouple was not placed on the substrate itself but on the susceptor as shown in Figure 2-10. In general, there exists thermal contact resistance between two materials, in this case the substrate and the susceptor. Thermal contact resistance comes from the surface roughness and gaps, and these gaps affect the heat transfer. The reactor in this study was under vacuum; therefore the heat transferred from the heater to the substrate was by conduction and radiation.

The pressure inside the reactor was not steady and caused the temperature to fluctuate because of flash evaporation of the precursor. The temperatures measured during maximum pressure and minimum pressure were approximately 5°C different. Furthermore, the temperature was controlled manually using a power box, and the response from the power supply to the heater and temperature depended on the person carrying out the experiment.

4.8.2. Pressure

The operating pressure was measured using the Pirani pressure gauge connected to the reactor via a 5 mm tube of 10 cm length. The pressure was

controlled manually using an air bleed. The pressure gauge error from the manufacturer was 2% and this yielded the pressure error of 3 to 8 Pa in the range of pressure studied. The pressure fluctuation due to manual control was in the range of 10 Pa. The uncertainty of pressure reading from the MKS pressure reading was 0.1, which is normally 10 Pa in the pressure of hundreds of Pa.

4.8.3. Precursor concentration

The error of precursor concentration could come from the syringe used during precursor preparation. The syringe for the precursor was 2 ml with graduation units of 0.1 ml. The syringe for the solvent was 50 ml, which has an accuracy of 2 ml. The precursor concentration error was estimated using the error propagation method. This method was applied for the precursor concentration calculated for Equation (3-1). When the concentration of the precursor was in the range of 0.15 to 0.50 mol%, the precursor concentration error was approximately 8%.

4.8.4. Injection volume

Sample loops used were from VICI. The ID accuracy was ± 0.005" for both 1/16" and 1/8" OD. The injection volume error was approximately ± 0.5 µl.

4.8.5. Thickness measurement

Film thickness was measured using a scanning electron microscope (SEM) at random locations. The thicknesses were measured using the annotation of an

image processing tool of the Orion control system software in the SEM, and the average film thickness was calculated using at least 3 sample points. The error of the thickness measurement was found to be less than 7%.

CHAPTER 5

WETTABILITY ANALYSIS

The hydrophobic property of deposited TiO_2 thin films on 3-D patterned substrates was investigated. This chapter presents the wettability analysis measured by the water contact angle of the deposited TiO_2 films on micro- and nano-scale features on Si_3N_4 substrates.

5.1. Wettability Test

The wettability property of deposited TiO_2 was examined using films deposited on micro- and nano-scale patterned Si_3N_4 substrates. Wettability was analysed through contact angle measurement. Each value of the contact angle was an average of three to four measurements on different areas of the same sample surface. A high contact angle means low wettability or hydrophobic surface. The as-deposited TiO_2 films were stored under atmospheric pressure in a desiccator. The aging of the samples was approximately 2 years for the study of contact angle with deposition temperatures and 5 months for the study of contact angle with pulse exposures. The films were deposited at the deposition temperature of 400 and 600°C under the base pressure of 100 Pa and pulsing time of 10 sec. Precursor concentrations were 0.15, 0.25 and 0.50 mol% and the injection volumes were 50, 100 and 250 µl. These resulted in pulse exposure of 32 to 214. The deionised water contact angle of Si_3N_4 substrate was found to be 74.7±1.4°. The water contact angles of Si_3N_4 substrate according to other studies vary from 24 to 42° (Dixit et al., 2007; Saadaoui et al., 2007).

Figure 5-1 illustrates the water contact angle and surface morphology of as-deposited TiO_2 for various deposition temperatures. The maximum contact angle of 107.0±13.8° was found at the deposition temperature of 600°C. The contact angle tended to increase as the deposition temperature increased. The contact angle of TiO_2 tended to be related to surface morphology as can be seen from Figure 4-19. The contact angle increased as the grain size decreased with an increase in the deposition temperature.

Figure 5-2 and Figure 5-3 show the water contact angle and surface morphology of as-deposited TiO_2 with various pulse exposures at the deposition temperature of 400 and 500°C, respectively. The maximum contact angle was 105.2±4.0° at the medium pulse exposure of 53. The minimum contact angle, which was lower than Si_3N_4 substrate, was 61.4±6.8°.

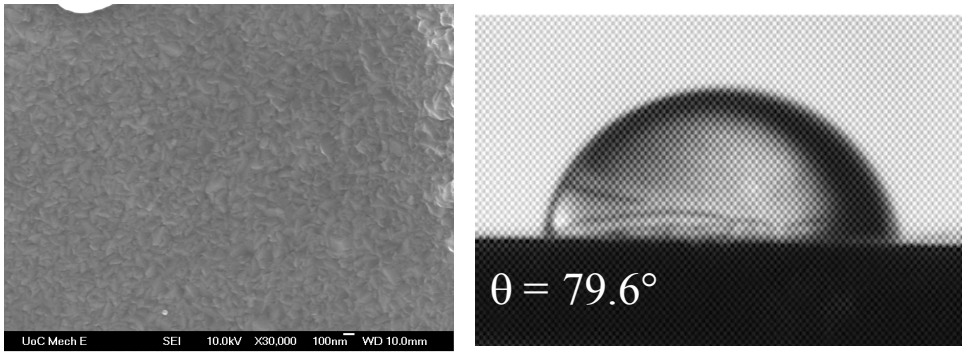

(a) 400°C

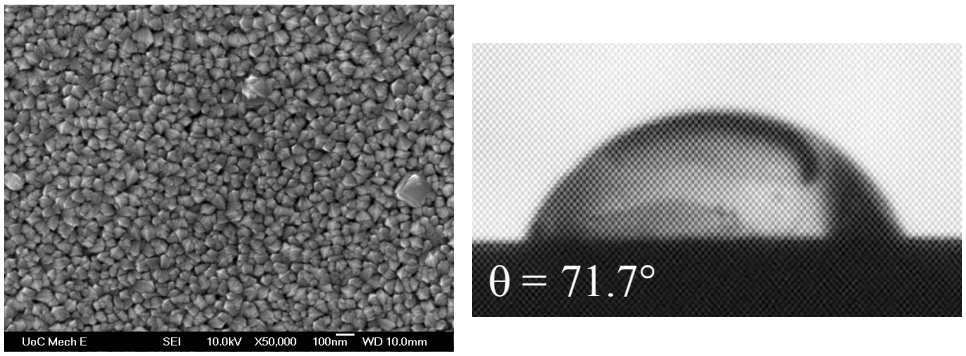

(b) 500°C

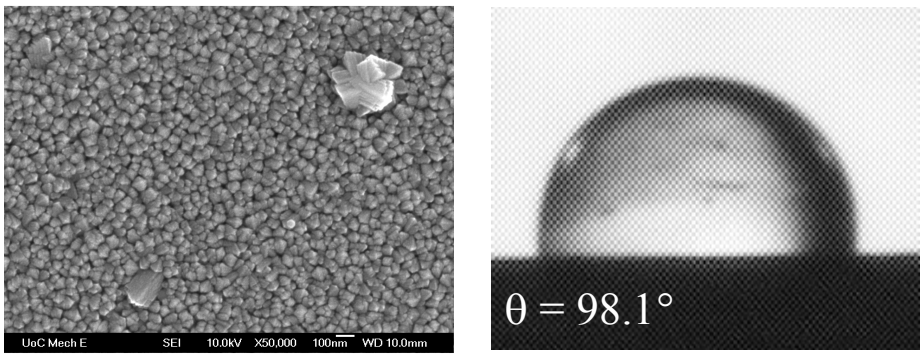

(c) 550°C

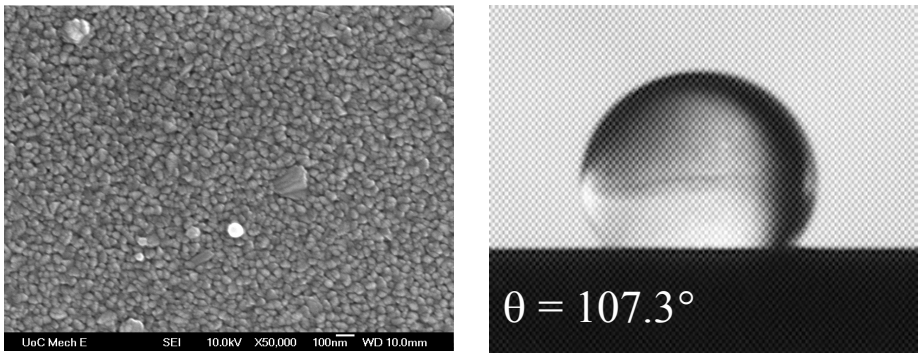

(d) 600°C

Figure 5-1: SEM images of surface morphology at 50,000x magnification and images of contact angle of deposited TiO_2 at various deposition temperatures (a) 400°C (b) 500°C (c) 550°C and (d) 600°C. (T=400-600°C, P_{min}=100 Pa, C_{mo}=0.50 mol%,v_L=100µl, t=10 sec)

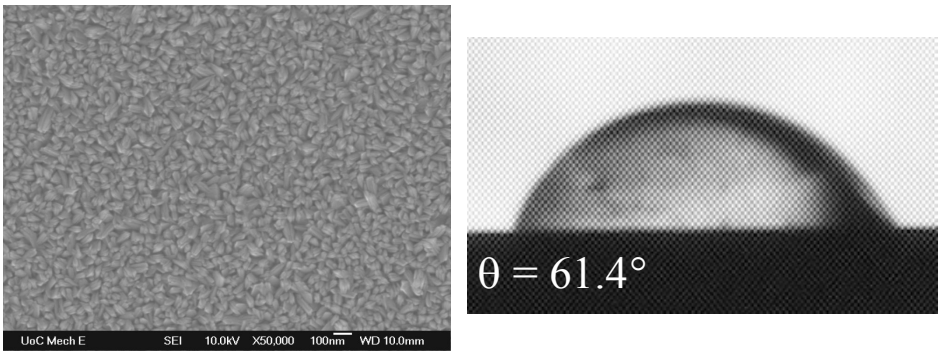

(a) Pulse Exposure: 32

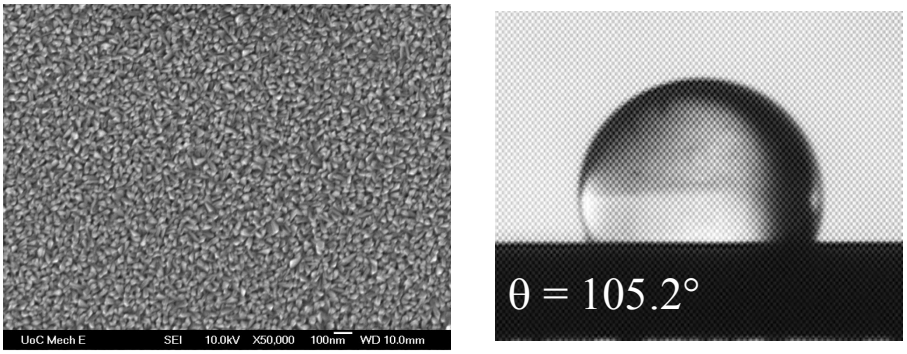

(b) Pulse Exposure: 53

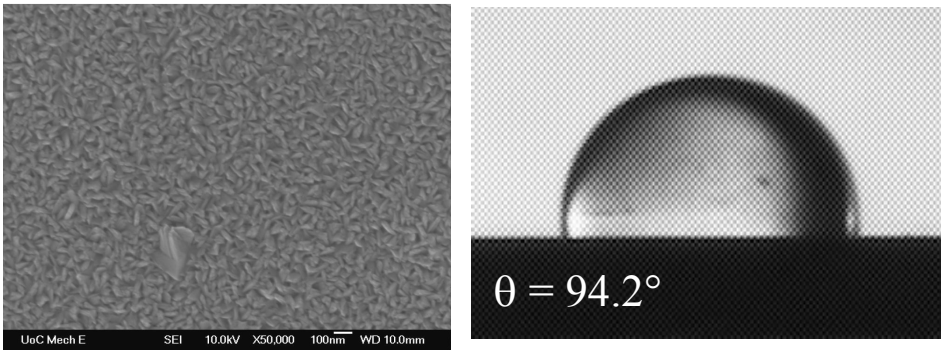

(c) Pulse Exposure: 160

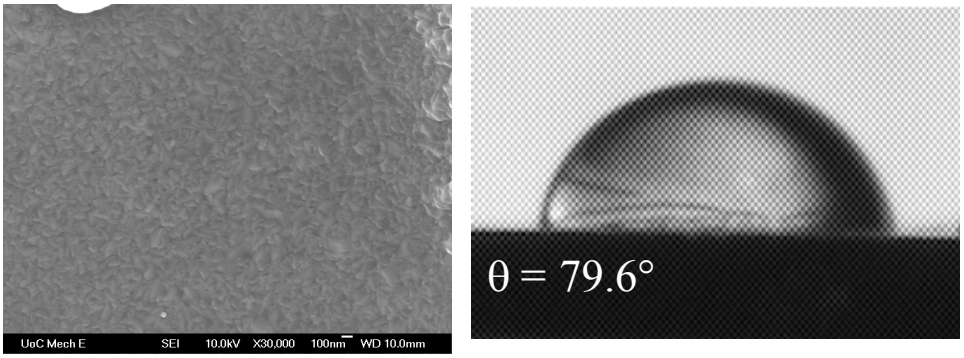

(d) Pulse Exposure: 214

Figure 5-2: SEM images of surface morphology at 50,000x magnification and images of contact angle of deposited TiO_2 at 400°C and various pulse exposures (a) 32 (b) 53 (c) 160 and (d) 214. (T=400°C, P_{min}=100 Pa, C_{mo}=0.15-0.50 mol%,v_L=50-250μl, t=10 sec)

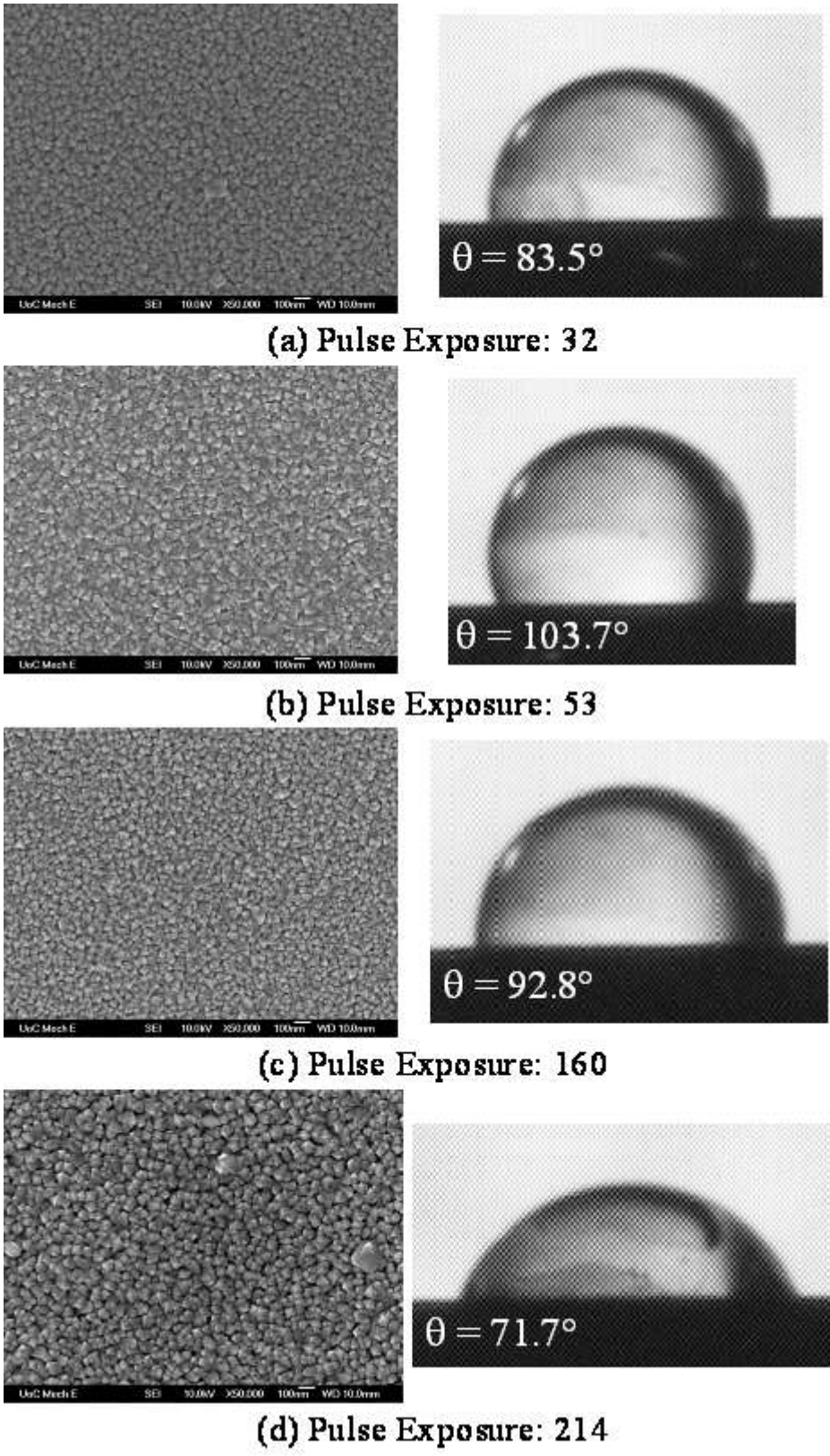

Figure 5-3: SEM images of surface morphology at 50,000x magnification and images of contact angle of deposited TiO_2 at 500°C and various pulse exposures (a) 32 (b) 53 (c) 160 and (d) 214. (T=500°C, P_{min}=100 Pa, C_{mo}=0.15-0.50 mol%,v_L=50-250μl, t=10 sec)

There was no specific pattern of water contact angle variation with pulse exposure. The water contact angle was higher at smaller grain size than at larger grain size. It has been reported that the surface roughness will have less effect on the wettability of the films when the roughness is less than a critical value. In the case of TiO_2, the critical value of the surface roughness is 5 nm (Wu et al., 2006). The contact angle was at the maximum at a pulse exposure of 53 before decreasing as the pulse exposure increased. The pulse exposure and deposition temperature influence the nucleation and growth of the deposited films, which affect the properties and porosity of the deposited films. Wettability generally depends on the chemical composition, crystal structure and surface morphology that affect the surface energy of the films (Duminica et al., 2007; Wu et al., 2006). The surface energy is the unbalanced force between atoms inside and at the surface boundary of the water and the film. It relates to the surface energy of the film, water, interfacial energy of the water and film interface, contact angle and surface roughness of the film. The composition and crystallographic orientation of the films also influence the surface energy. High surface energy results in low contact angle (Wu et al., 2006).

CHAPTER 6

CONCLUSION

This study aims to examine the possibility of applying pulsed-pressure metalorganic chemical vapour deposition (PP-MOCVD) to conformal coating and to investigate the influence of PP-MOCVD processing parameters for the deposition of thin titania or titanium dioxide (TiO_2) on 3-D featured and non-featured substrates. Five processing parameters were investigated for thin TiO_2 film deposition on the flat silicon (Si), silicon nitride (Si_3N_4) and quartz and patterned Si and Si_3N_4 substrates. The deposition conditions studied were temperatures in the range of 400 to 600°C; base pressures from 50 to 200 Pa; injection volumes of 50, 100 and 250 μl; precursor concentrations of 0.15, 0.25 and 0.50 mol%; and relaxation times of 0 to 10 sec. Base pressure, precursor concentration and precursor injection volume gave a pulse exposure between 16 and 214. Three processing parameters: deposition temperature, injection volume and precursor concentration were chosen for the conformality study. The parameters selected for the conformality study were limited to three because the base pressure and relaxation time were found to have minor effects on growth rate and surface morphology.

All of the as-deposited TiO_2 thin films were crystalline with columnar microstructure. They were anatase with thicknesses in the range of 90 to 300 nm and a growth rate of 2 to 80 $nm \cdot min^{-1}$. These films were deposited on substrates with feature sizes which varied from 100 nm to 10 μm with the

aspect ratios of 1:1, 1:2 or 2:1. The as-deposited TiO_2 had a refractive index for the anatase phase of 2.24 with an energy band gap of 3.7 eV.

The growth rate increased with the deposition temperature and reached the maximum of 450°C before decreasing as the deposition temperature increased. The activation energy (E_a) was found to be 80 kJ·mol^{-1}. The reactor base pressure and pulsing time had minor influences on growth rate. The base pressure did not affect the dynamics of the mass transport to the substrate surface for PP-MOCVD. The growth rate increased as the precursor concentration and precursor injection volume increased because of the increase in precursor molecules.

The reactor base pressure and relaxation time had no obvious effects on the grain size and surface roughness of the deposited TiO_2 thin films at the deposition temperatures of 400 to 500°C. Roughness was in the range of 2.5 to 6.4 nm with maximum standard deviation of 1.7 nm. The grain size was between 50 and 330 nm with the highest standard deviation of 120 nm. The high standard deviation was attributed to the large crystals on the deposited film surface. The grain size varied inversely with the deposition temperature, and this agreed with the results in the literature findings that the grain size at higher deposition temperatures should be smaller as fully dense films are formed because of the faster growth rate. Surface roughness varied inversely with grain size. The films tended to be smoother with larger grain size.

Conformality varied from poor at 0.45 to good at 0.95. The maximum conformal step coverage of 0.95 was achieved at the deposition temperature of

400°C, base pressure of 100 Pa, 100 μl injection volume, 0.50 mol% precursor concentration and pulsing time of 10 sec with 20 $nm \cdot min^{-1}$ in growth rate. Using PP-MOCVD, a high conformality of over 0.80 was expected when the film was deposited under low deposition temperature and low precursor concentration. Conformality decreased as the deposition temperature increased. The surface kinetics was the rate limiting step at low deposition temperature and is a favourable rate limiting step for good conformal coating. The injection volume of the liquid precursor had a minor effect at the deposition temperatures of 400 and 500°C. Conformality varied inversely with the precursor concentration. At high precursor concentration and low deposition temperature, the surface kinetics was expected to be the rate limiting step. Conformality also depends on the sticking coefficient and free energy between precursor molecules and the substrate surface. Precursor molecules tended to adsorb and react on the top of the trench and at the edge of the trench mouth as the precursor concentration increased in this study. According to the results from this study, the deposition temperature and precursor concentration were the processing parameters that affected the conformality of deposited TiO_2 thin film by PP-MOCVD.

The contact angle of the deposited films varied from 61.4 to 107°. The best contact angle was obtained at the deposition of TiO_2 on micro-scale structure at a deposition temperature of 600°C with conformality of 0.82. The contact angle was inversely dependent on the deposition temperature when the grain size became smaller. The contact angle tended to increase as the pulse exposure increased to the maximum, and decrease as the pulse exposure

increased at the deposition temperatures of 400 and 500°C. The highest contact angle was at the pulse exposure of 53. Surface morphology affected the wettability. The grain size at the pulse exposure 53 was the smallest at the deposition temperature of 400°C. The as-deposited TiO_2 thin films were hydrophobic depending on surface morphology, surface roughness and grain size.

CHAPTER 7

FUTURE WORK

This chapter gives a summary of the possibility of using the results from this study for future research. The conformality of TiO_2 thin films on 3-D structures by PP-MOCVD can be applied to many applications and other materials. The outline of the chapter on future work is listed below.

7.1. Investigation of Other Processing Parameters on Conformality

7.2. Imprint Test

7.3. Deposition of TiO_2 for Solar Application

7.4. Deposition of Other Materials Using PP-MOCVD

7.1. Investigation of Other Processing Parameters on Conformality

Because of the limitation of patterned substrates, conformality was investigated using three processing parameters: deposition temperature, precursor concentration and liquid precursor injection volume. Other processing parameters of PP-MOCVD that might influence the conformality include reactor base pressure, pulsing time, the distance between the nozzle and the substrate, feature size and substrate material. Further conformality could be carried out as the base pressure and pulsing time influenced the peak pressure, hence the total molecular flux of the molecules to the substrate surface. The distance between the nozzle and the substrate and feature size could affect the

pulse exposure. It is interesting to study the conformality over a range of substrate materials depending on the applications, as it is known that substrate materials influence the nucleation and growth of the films. Further investigations provide information and optimisation on conformality that is influenced by various processing parameters for a wide range of applications.

7.2. Imprint Test

The deposited TiO_2 on Si_3N_4 and Si with micro- and nano-scale structures are to be employed to test the anti-sticking properties of the TiO_2 coated moulds. UV nanoimprint lithography can be applied. Other principal properties for UV nanoimprint lithography moulds include UV transparency, hardness and reproducibility of patterns, which should be tested.

7.3. Phase of TiO_2 analysis

It is interesting to study the phase change of deposited TiO_2 on Si_3N_4 with the deposition temperature at a thickness of more than 10 μm. According to this study, only an anatase phase was found as the deposited films were less than 3μm thick. The rutile phase of deposited TiO_2 on nickel with a thickness of 45±1 μm using PP-MOCVD was found at deposition temperatures above 450°C by Krumdieck et al. (Krumdieck and Raj, 2001b). It should be noted that the phase transformation from anatase to rutile was at temperatures over 700°C (Seifried et al., 2000; Wetchakun and Phanichphant, 2008; Yoo et al., 2007).

7.4. Deposition of TiO_2 for Solar Application

TiO_2 has been studied for dye-sensitised and thin film solar cell production (Jiu et al., 2005). It has high transmission in a UV-visible light region and can be used as anti-reflection coating. PP-MOCVD has shown the capability to deposit conformal thin anatase TiO_2 film coating on 3-D structures. This could be applied for TiO_2 deposition on 3-D solar modules to increase the efficiency of the photovoltaic or solar panel and conductive plate coating for the anode in a dye-sensitised solar cell (Duta, 2006; Valdees et al., 2007).

7.5. Deposition of Other Materials Using PP-MOCVD

The PP-MOCVD method can be applied to deposit conformal films from liquid or gaseous precursors that have a high enough vapour pressure, for example, yttrium barium copper oxide (YBCO) and hydroxyapatite.

YBCO is known as a superconductor material. The problems that are usually found with the deposited YBCO films include the composition, homogeneity of phase and composition and microstructure of the films. PP-MOCVD has shown capability in the deposition of conformal thin films on featured substrates. The deposition of hydroxyapatite on 3-D implants for biomedical purposes could be achieved by processing parameters and precursor chemistry optimisation.

REFERENCES

Akiyama, Y., Imaishi, N., Shin, Y.-S., and Jung, S.-C., Macro- and micro-scale simulation of growth rate and composition in MOCVD of yttria-stabilized zirconia, *Journal of Crystal Growth*, **241** (2002) 352-362.

Al-Mohssen, H. A., and Hadjiconstantinou, N. G., Arbitrary-pressure chemical vapor deposition modeling using direct simulation Monte Carlo with nonlinear surface chemistry, *Journal of Computational Physics*, **198** (2004) 617-627.

Alkaisi, M. M., Blaikie, R. J., and McNab, S. J., Low temperature nanoimprint lithography using silicon nitride molds, *Microelectronic Engineering*, **57-58** (2001) 367-373.

Aratani, M., Oikawa, T., Ozeki, T., and Funakubo, H., Epitaxial-grade polycrystalline $Pb(Zr,Ti)O_3$ film deposited at low tempertaure by pulsed-metalorganic chemical vapor deposition, *Applied Physics Letters*, **79** (2001) 1000-1002.

Babelon, P., Dequiedt, A. S., Mostefa-Sba, H., Bourgeois, S., Sibillot, P., and Sacilotti, M., SEM and XPS studies of titanium dioxide thin films grown by MOCVD, *Thin Solid Films*, **322** (1998) 63-67.

Barbato, A., Fiorucci, A., Rondanini, M., and Cavallotti, C., Multiscale investigation of the influence of surface morphology on thin film CVD, *Surface & Coatings Technology*, **201** (2007) 8884-8887.

Battiston, G. A., Gerbasi, R., Porchia, M., and Rizzo, L., TiO_2 Coating by Atmospheric Pressure MOCVD in a Conveyor Belt Furnace for Industrial Applications, *Chemical Vapor Deposition*, **5** (1999) 73-77.

Bernardi, M. I. B., Lee, E. J. H., Lisboa-Filho, P. N., Leite, E. R., Longo, E., and Varela, J. A., TiO_2 thin film growth using the MOCVD method, *Materials Research*, **4** (2001) 223-236.

Bessergenev, V. G., Khmelinskii, I. V., Pereira, R. J. F., Krisuk, V. V., Turgambaeva, A. E., and Igumenov, I. K., Preparation of TiO_2 films by CVD method and its electrical, structural and optical properties, *Vacuum*, **64** (2002) 275-279.

Bloor, D., Brook, R. J., Flemings, M. C., Mahajan, S., and Cahn, R. W., *The Encyclopedia of advanced of materials*, Oxford: Pergamon, Cambridge (1994).

Brevet, A., Peterle, P. M., Imhoff, L., Marco de Lucas, M. C., and Bourgeois, S. , Initial stages of TiO_2 thin films MOCVD growth studied by in situ surface analyses, *Journal of Crystal Growth*, **275** (2005) e1263-e1268.

Byun, C., Jang, J. W., Kim, I. T., Hong, K. S., and Lee , B.-W., Anatase-to-rutile transition of titania thin films prepared by MOCVD , *Materials Research Bulletin*, **32** (1997) 431-440.

Caglar, M., Caglar, Y., and Ilican, S. , The determination of the thickness and optical constants of the ZnO crystalline thin film by using envelope method, *Journal of optoelectronics and advanced materials*, **8** (2006) 1410-1413.

Cave, H. M., Krumdieck, S. P., and Jermy, M. C. , Development of a model for high precursor conversion efficiency pulsed-pressure chemical vapor deposition (PP-CVD) processing, *Chemical Engineering Journal*, **135** (2008) 120-128.

Chang, H. L. M., You, H., Gao, Y., Guo, J., Foster, C. M., Chiarello, R. P., Zhang, T. J., and Lam, D. J., Structural properties of epitaxial TiO_2 films grown on sapphire ($11\bar{2}0$) by MOCVD, *Journal of Materials Research*, **7** (1992) 2495-2506.

Chen, G., Luo, G., Yang, X., Sun, Y., and Wang, J. , Anatase-TiO_2 nano-particle preparation with a micro-mixing technique and its photocatalytic performance, *Materials Science and Engineering A*, **380** (2004) 320-325.

Chen, Y., and Dionysiou, D. D., Correlation of structural properties and film thickness to photocatalytic activity of thick TiO_2 films coated on stainless steel, *Applied Catalysis B: Environmental*, **69** (2006) 24-33.

Chen, Z.-X., and Derking, A., TiO_2 thin films by chemical vapour deposition: Control of the deposition process and film characterisation, *Journal of Materials Chemistry*, **3** (1993) 1137-1140.

Chou, S. Y., and Krauss, P. R., Imprint lithography with sub-10 nm feature size and high thruoghput, *Microelectronic Engineering*, **35** (1997) 237-240.

Choy, K. L., Chemical vapour deposition of coatings, *Progress in Materials Science*, **48** (2003) 57-170.

Clark, R. J. H., Bradley, D. C., and Thornton, P. , *The chemistry of titanium, zirconium and hafnium*, Pergamon Press, New York, USA (1975).

Condorelli, G. G., Malandrino, G., and Fragalae, I. L., Engineering of molecular architectures of β−diketonate precursors toward new advanced materials, *Coordination Chemistry Reviews*, **251** (2007) 1931-1950.

Dauksher, W. J., Le, N. V., Ainley, E. S., Nordquist, K. J., Gehoski, K. A., Young, S. R., Baker, J. H., Convey, D., and Mangat, P. S., Nano-imprint lithography: Templates, imprinting and wafer pattern transfer, *Microelectronic Engineering*, **83** (2006) 929-932.

Diebold, U., The Surface Science of Titanium Dioxide, *Surface Science Reports*, **48** (2003) 53-229.

Dislich, H., and Hinz, P., History and principles of the sol-gel process, and some new multicomponent oxide coatings, *Journal of Non-Crystalline Solids*, **48** (1982) 11-16.

Dixit, P., Chen, X., Miao, J., Divakaran, S., Preisser, R., Study of surface treatment processes for improvement in the wettability of silicon-based materials used in high aspect ratio through-via copper electroplating, *Applied Surface Science*, **253** (2007) 8637-8646.

Duminica, F.-D., Maury, F., and Hausbrand, R., Growth of TiO_2 Thin Films by AP-MOCVD on Stainless Steel Substrates for Photocatalytic Applications, *Surface and Coatings Technology*, **201** (2007) 9304-9308.

Duta, A., TiO_2 thin layers with controlled morphology for ETA (extremely thin absorber) solar cells, *Thin Solid Films*, **511-512** (2006) 195-198.

Elers, K.-E., Blomberg, T., Peussa, M., Aitchison, B., Haukka, S., and Marcus, S., Film Uniformity in Atomic Layer Deposition, *Chemical Vapor Deposition*, **12** (2006) 13-24.

Fictorie, C. P., Evans, J. F., and Gladfelter, W. L., Kinetic and mechanistic study of the chemical vapor deposition of titanium dioxide thin films using tetrakis-(isopropoxo)-titanium (IV), *Journal of Vacuum Science and Technology A*, **12** (1994) 1108-1113.

Fox, M., *Optical Properties of Solids*, Oxford University Press, New York (2001).

Frohn, A., and Roth, N., *Dynamics of droplets*, Springer, Berlin; New York (2000).

Funakubo, H., Nagai, A., Asano, G., Koo, J.-M., Shin, S.-M., and Park, Y., Effect of source materials on film thickness and compositional uniformity of MOCVD-P(Zr, Ti)O3 films, *Surface & Coatings Technology*, **201** (2007) 9279-9284.

Funakubo, H., Tokita, K., Oikawa, T., Aratani, M., and Saito, K. , Comparison of crystal structure and electrical properties of tetragonal and rhombohedral $Pb(Zr,Ti)O_3$ films prepared at low temperature by pulsed-metalorganic chemical vapor deposition, *Journal of Applied Physics*, **92** (2002) 5448-5452.

Gilmer, G. H., Huang, H., and Roland, C. , Thin film deposition: fundamentals and modeling, *Computational Materials Science*, **12** (1998) 354-380.

Glocker, D. A., and Shah, S. I. , *Handbook of thin film process technology*, Philadelphia: Institute of Physics Publishing, Bristol, UK (1995).

Götzberger, A., Hebling, C., and Schock, H.-W., Photovoltaic materials, history, status and outlook, *Materials Science and Engineering R*, **40** (2003) 1-46.

Guemues, C., Ozkendir, O. M., Kavak, H., and Ufuktepe, Y. , Structural and optical properties of zinc oxide thin films prepared by spray pyrolysis method, *Journal of optoelectronics and advanced materials*, **8** (2006) 299-303.

Hartshorn, R., Stockwell, S., Lebedev, M., and Krumdieck, S. , Precursor system for bio-integration ceramics and deposition onto tantala scaffold bone interface surfaces, *Surface & Coating Technology*, **201** (2007) 9413-9416.

Hausmann, D. M., Rouffignac, P. d., Smith, A., Gordon, R., and Monsma, D. , Highly conformal atomic layer deposition of tantalum oxide using alkylamide precursors, *Thin Solid Films*, **443** (2003) 1-4.

Heikkilä, M., Puukilainen, E., Ritala, M., and Leskelä, M. , Effect of thickness of ALD grown TiO_2 films on photoelectrocatalysis, *Journal of Photochemistry and Photobiology A: Chemistry*, **204** (2009) 200-208.

Hitchman, M. L., and Alexandrov, S. E. , New approaches to titania and silica CVD, *The Electrochemical Society Interface*, **10** (2001) 40-45.

Holongak Jr., N., Kolbas, R. M., Dupuis, R. D., and Dapkus, P. D. , Room-temperature continuous operation of photopumped MO-CVD $Al_xGa_{1-x}As$-GaAs-$Al_xGa_{1-x}As$, *Applied Physics Letters*, **33** (1978) 73-75.

Hong, L.-C., Hsu, C.-C., and Tsai, D.-S., Uniformity of deposited film thickness on a uneven surface by direct simulation Monte Carlo, *Materials Chemistry and Physics*, **48** (1997) 82-89.

IslamRaja, M. M., Cappelli, M. A., McVittie, J. P., and Saraswat, K. C. , A 3-dimensional model for low-pressure chemical-vapor-deposition step coverage in trenches and circular vias, *Journal of Applied Physics*, **70** (1991) 7137-7140.

Jiu, J., Wang, F., Sakamoto, M., Takao, J., and Adachi, M. , Performance of dye-sensitized solar cell based on nanocrystals TiO_2 film prepared with mixed template method, *Solar Energy Materials & Solar Cells*, **87** (2005) 77-86.

Joegi, I., Paers, M., Aarik, J., Aidla, A., Laan, M., Sundqvist, J., Oberbeck, L., Heitmann, J., and Kukli, K., Conformity and structure of titanium oxide films grown by atomic layer deposition on silicon substrates, *Thin Solid Films*, **516** (2008) 4855-4862.

Jones, A. C., and Hitchman, M. L., *Chemical Vapour Deposition: Precursors, Processes and Applications*, The Royal Society of Chemistry, Cambridge, UK (2009).

Jung, S.-C., Kim, S.-J., Imaishi, N., and Cho, Y.-I., Effect of TiO_2 thin film thickness and specific surface area by low-pressure metal-organic chemical vapor deposition on photocatalytic activities, *Applied Catalysis B: Environmental*, **55** (2005) 253-257.

Kaliwoh, N., Zhang, J.-Y., and Boyd, I. W., Characterisation of TiO_2 deposited by photo-induced chemical vapour deposition, *Applied Surface Science*, **186** (2002) 241-245.

Kang, B.-C., Lee, S.-B., and Boo, J.-H., Growth of TiO_2 thin films on Si(100) substrates using single molecular precursors by metal organic chemical vapor deposition, *Surface and Coatings Technology*, **131** (2000) 88-92.

Kasu, M., and Kobayashi, N., Surface kinetics of metalorganic vapor-phase epitaxy: surface diffusion, nucleus formation, sticking at steps, *Journal of Crystal Growth*, **174** (1997) 513-521.

Kim, J., Hong, H., Oh, K., and Lee, C. , Properties including step coverage of TiN thin films prepared by atomic layer deposition, *Applied Surface Science*, **210** (2003) 231-239.

Kitazawa, S.-i., Choi, Y., Yamamoto, S., and Yamaki, T. , Rutile and anatase mixed crystal TiO_2 thin films prepared by pulsed laser deposition, *Thin Solid Films*, **515** (2006) 1901-1904.

Konijin, M., Alkaisi, M. M., and Blaikie, R. J., Nanoimprint lithography of sub-100 nm 3D structures, *Microelectronic Engineering*, **78-79** (2005) 653-658.

Korgel, B., and Hicks, R. F., A diffusion model for selective-area epitaxy by metalorganic chemical vapor deposition, *Journal of Crystal Growth*, **151** (1995) 204-212.

Krishna, S., *Handbook of Thin-Film Deposition Processes and Techniques: Principles, Methods, Equipment and Applications*, 2/Ed. Noyes Publications, New York, USA (2002).

Kristinsdottir, A., *Production of a gas tight ionic yttria stablized zirconia thin films for solid oxide fuel cells using pulsed-chemical vapor deposition*, Master Degree Thesis, University of Canterbury, Christchurch, New Zealand (2007).

Krumdieck, S., *Experimental Characterization and Modeling for the Growth Rate of Oxide Coatings from Liquid Solutions of Metalorganic Precursors by Ultrasonic Pulsed Injection in a Cold Wall Low Pressure Reactor*, Doctor of Philosophy Degree Thesis, University of Colorado at Boulder (1999).

Krumdieck, S., Kinetic model of low pressure film deposition from single precursor vapor in a well-mixed, cold-wall reactor, *Acta Materialia*, **49** (2001) 583-588.

Krumdieck, S., Baluti, S. I., Marcus, L., and Peled, A. , Design investigation for three-dimensional uniformity of the mass transport field, *Journal of the Electrochemical Society*, **2005-9** (2005) 13-20.

Krumdieck, S., and Raj, R., Conversion efficiency of alkoxide precursor to oxide films grown by an ultrasonic-assisted, pulsed liquid injection, metalorganic chemical vapor deposition (Pulsed-CVD) process, *Journal of the American Ceramic Society*, **82** (1999) 1605-1607.

Krumdieck, S., and Raj, R., Experimental characterization and modeling of pulsed MOCVD with ultrasonic atomization of liquid precursor, *Chemical Vapor Deposition*, **7** (2001a) 85-90.

Krumdieck, S., and Raj, R., Growth rate and morphology for ceramic films by pulsed-MOCVD, *Surface and Coatings Technology*, **141** (2001b) 7-14.

Krumdieck, S., Sbaizero, O., Bullert, A., and Raj, R. , Solid Yttria-Stabilized Zirconia films by pulsed chemical vapor deposition from metal-organic precursors, *Journal of the American Ceramic Society*, **85** (2002) 2873-2875.

Krumdieck, S., Sbaizero, O., Bullert, A., and Raj, R. , YSZ layers by pulsed-MOCVD on solid oxide fuel cell electrodes, *Surface and Coatings Technology*, **167** (2003) 226-233.

Krumdieck, S., Sbaizero, O., and Raj, R., Unique precursor delivery and control afforded by low-pressure pulsed-CVD process with ultrasonic atomization, *Journal de Physique IV France*, **11** (2001) Pr3-1161-1168.

Krumdieck, S. P., Cave, H. M., Baluti, S., Jermy, M. C., and Peled, A. , Expansion transport regime in pulsed-pressure chemical vapor deposition, *Chemical Engineering Science*, **62** (2007a) 6121-6128.

Krumdieck, S. P., Kristinsdottir, A., Ramirez, L., and Lebedev, M., and Long, N., Growth rate, microstructure and conformality as a function of vapor exposure for zirconia thin films by pulsed-pressure MOCVD, *Surface and Coatings Technology*, **201** (2007b) 8908-8913.

Lee, M.-K., Hung, Y.-M., and Huang, J.-J., Properties of TiO_2 thin films on InP substrate prepared by metalorganic chemical vapor deposition, *Japanese Journal of Applied Physics*, **40** (2001) 6543-6546.

Leiby, M. W., *Chemical vapor deposition by pulsed ultrasonic direct injection of liquid precursors produces versatile method for creation of thin film circuits and devices*, Sono-Tek Corporation, New York, USA (2006).

Leistner, T., Lehmbacher, K., Härter, P., Schmidt, C., Bauer, A. J., Frey, L., and Ryssel, H., MOCVD of titanium dioxide on the basis of new precursors, *Journal of Non-Crystalline Solids*, **303** (2002) 64-68.

Leng, Y., *Materials Characterization Introduction to Microscopic and Spectroscopic Methods*, John Wiley & Sons (Asia) Pte Ltd (2008).

Lin, H.-M., Keng, C.-H., and Tung, C.-Y., Gas-Sensing Properties of Nanocrystalline TiO_2, *NanoStructured Materials*, **9** (1997) 747-750.

Liu, F.-M., and Wang, T.-M., Surface and optical properties of nanocrystalline anatase titania films grown by radio frequency reactive magnetron sputtering, *Applied Surface Science*, **195** (2002) 284-290.

Ma, H. L., Yang, J. Y., Dai, Y., Zhang, Y. B., Lu, B., and Ma, G. H. , Raman study of phase transformation of TiO_2 rutile single crystal irradiated by infrared femtosecond laser, *Applied Surface Science*, **253** (2007) 7497-7500.

Manasevit, H. M., The use of metalorganics in the preparation of semiconductor materials: Growth on insulating substrates, *Journal of Crystal Growth*, **13/14** (1972) 306-314.

Manasevit, H. M., Recollections and reflections of MO-CVD, *Journal of Crystal Growth*, **55** (1981) 1-9.

Manasevit, H. M., and Simptons, W. I., The Use of Metal-Organics in the Preparation of Semiconductor Materials, *Journal of Electrochemistry Society*, **116** (1969) 1725-1731.

Mohamed, K., Alkaisi, M. M., and Smaill, J., Resist Deformation at Low Temperature in Nanoimprint Lithography, *Current Applied Physics*, **6** (2006) 486-490.

Monteiro, O. R., and Liu, H., Necleation and growth of CVD diamond films on patterned substrates, *Diamond and Related Materials*, **12** (2003) 1357-1361.

Morosanu, C. E., *Thin Films by Chemical Vapor Deposition*, Elsevier, Amsterdam (1990).

Musice, S., Gotice, M., Ivanda, M., Popovice, S., Turkovice, A., Trojko, R., Sekulice, A., and Furice, K., Chemical and microstructural properties of TiO_2 synthesized by sol-gel procedure, *Materials Science and Engineering B*, **47** (1997) 33-40.

Nakamura, T., Novel pulse pressure CVD for void free STI trench TEOS fill, *IEEE* (2001) 117-120.

Nami, Z., Misman, O., Erbil, A., and May, G. S., Computer simulation study of the MOCVD growth of titanium dioxide films, *Journal of Crystal Growth*, **171** (1997a) 154-165.

Nami, Z., Misman, O., Erbil, A., and May, G. S., Effect of growth parameters on TiO_2 thin films deposited using MOCVD, *Journal of Crystal Growth*, **179** (1997b) 522-538.

Neyts, E., Bogaerts, A., Meyer, M. D., and Gils, S. V., Macroscale computer simulations to investigation the chemical vapor deposition of thin metal-oxide films, *Surface & Coatings Technology*, **201** (2007) 8838-8841.

O'Regan, B., and Grätzel, M., A Low Cost High Efficiency Solar Cell, *Nature*, **353** (1991) 737.

Ogawa, H., Higuchi, T., Nakamura, A., Tokita, S., Miyazaki, D., Hattori, T., and Tsukamoto, T., Growth of TiO_2 thin film by reactive RF magnetron sputtering using oxygen radical, *Journal of Alloys and Compounds*, **449** (2008) 375-378.

Ohring, M., *Materials Science of Thin Film: Deposition and Structure*, Academic Press, San Diego, USA (2002).

Palma, A., and Alavi, A., An ab initio study of titanium tetra-iso-propoxide (TTIP) adsorption mechanism on a Si(100) surface, *Computational Materials Science*, **33** (2005) 244-249.

Park, Y. R., and Kim, K. J., Structural and optical properties of rutile and anatase TiO_2 thin films: Effects of Co doping, *Thin Solid Films*, **484** (2005) 34-38.

Pierson, H. O., *Handbook of CVD: Principles, Technology, and Applications*, 2/Ed. Noyes Publications, New York, USA (2006).

Porto, S. P. S., Fleury, P. A., and Damen, T. C., Raman Spectra of TiO_2, MgF_2, ZnF_2, FeF_2, and MnF_2, *Physical Review*, **154** (1967) 522-526.

Powell, C. F., *Chemical Vapor Deposition*, Jr./Ed. John Wiley & Sons, New York (1966).

Powell, C. F., Oxley, J. H., and Blocher, J. M. J., Vapor deposition, *Journal of the Electrochemical Society*, **113** (1966) 226c-269c.

Ramirez, L., Mecartney, M. L., and Krumdieck, S., Nanocrystalline ZrO_2 thin films on silicon fabricated by pulsed-pressure metalorganic chemical vapor deposition (PP-MOCVD), *Journal of Materials Research*, **23** (2008) 2202-2211.

Richards, B. S., Lambertz, A., and Sproul, A. B., Determination of the optical properties of non-uniformly thick non-hydrogenated sputtered silicon thin films on glass, *Thin Solid Films*, **460** (2004) 247-255.

Roth, A., *Vacuum technology*, 3rd/Ed., Amsterdam, North-Holland (1990).

Saadaoui, M., Wien, W., van Zeijl, H., van den Bogaard, A., Sarro, P. M., Improvement of wettability of silicon nitride in PECVD environment for copper electrodeposition in HAR vias, *SAFE & Prorisc 2004 Conference*, Veldhoven, The Netherlands (2007).

Sankapal, B. R., Lux-Steiner, M. C., and Ennaoui, A., Synthesis and characterization of anatase-TiO_2 thin films, *Applied Surface Science*, **239** (2005) 165-170.

Schumacher, M., Lindner, J., Baumann, P. K., Schienle, F., Solayappan, N., Joshi, V., Araujo, C. A., and McMillan, L. D., MOCVD for complex multicomponent thin films-a leading edge technology for next generation devices, *Materials Science in Semiconductor Processing*, **5** (2003) 85-91.

Seifried, S., Winterer, M., and Hahn, H., Nanocrystalline titania films and particles by chemical vapor synthesis, *Chemical Vapor Deposition*, **6** (2000) 239-244.

Sherwood, E. M., and Blocher, J. M., Vapor deposition: The first hundred years, *Journal of Metals*, **17** (1965) 594-599.

Singh, J., Multilayer *Ceramic/Metallic Coating by Ion Beam-Assisted, Electron Beam Physical Vapor (EB-PVD) Deposition*, The Applied Research Laboratory, Penn State University (1997).

Siriwongrungson, V., Alkaisi, M. M., and Krumdieck, S. P. , Step coverage of thin titania films on patterned silicon substrate by pulsed-pressure MOCVD, *Surface and Coatings Technology*, **201** (2007) 8944-8949.

Smith, D. L., *Thin Film Deposition: Principles and Practice*, McGraw-Hill, New York (1995).

Stamate, M., and Lazar, G., Application of Titanium Dioxide Photocatalysis to Create Self-Cleaning Materials, *Romanian Technical Sciences Academy*, **3** (2007) 280-285.

Taga, Y., Recent progress of nanotechnologies of thin films for industrial applications, *Materials Science and Engineering C*, **15** (2001) 231-235.

Tuan, A., Yoon, M., Medvedev, V., Ono, Y., Ma, Y., and Rogers Jr., J. W. , Interface control in the chemical vapor deposition of titanium dioxide on silicon (100), *Thin Solid Films*, **377-378** (2000) 766-771.

Valdees, M., Frontini, M. A., Vaezquez, M., and Goossens, A. , Low-cost 3D nanocomposite solar cells obtained by electrodeposition of $CuInSe_2$, *Applied Surface Science*, **254** (2007) 303-307.

Versteeg, V. A., Avedisian, C. T., and Raj, R., *Method and Apparatus for CVD using Liquid Delivery System with Ultrasonic Nozzle*, Sono-Tek Corp., USA (1995).

Werbowy, A., Olszyna, A., Zdunek, K., Sokolowska, A., Szmidt, J., and Barcz, A. , Peculiarities of thin film deposition by means of reactive impulse plasma assisted chemical vapor deposition (RIPACVD) method, *Thin Solid Films*, **459** (2004) 160-164.

Wetchakun, N., and Phanichphant, S., Effect of temperature on the degree of anatase-rutile transformation in titanium dioxide nanoparticles synthesized by the modified sol-gel method, *Current Applied Physics*, **8** (2008) 343-346.

Wiest, F., Capodieci, V., Blank, O., Gutsche, M., Schulze, J., Eisele, I., Matusche, J., and Schmidt, U. I., Conformal aluminum oxide coating of high aspect ratio structures using metalorganic chemical vapor deposition, *Thin Solid Films*, **496** (2006) 240-246.

Wöhler, F., and Uslar, L., Ueber metallisches Wolfram und Molybdaene, *Justus Liebigs Annalen der Chemie*, **94** (1855) 255-256.

Yoo, D., Kim, I., Kim, S., Hahn, C. H., Lee, C., and Cho, S., Effects of annealing temperature and method on structural and optical properties of TiO_2 films

prepared by RF magnetron sputtering at room temperature, *Applied Surface Science*, **253** (2007) 3888-3892.

Yun, J.-H., and Rhee, S.-W., Experimental and theoretical study of step coverage in metal-organic chemical vapor deposition of tantalum oxide thin films, *Thin Solid Films*, **292** (1997) 324-329.

Zhang, J., Li, M., Feng, Z., Chen, J., and Li, C. , UV Raman Spectroscopic Study on TiO_2. I. Phase Transformation at the Surface and in the Bulk, *Journal of Physical Chemistry B,* **110** (2006) 927-935.

Zheng, Y., Mokhtari, S., Ferdinand, A., Eakin, J., and Bartholomew, L. , Optimization of SiO_2 film conformality in TEOS/O_3 APCVD, *Thin Solid Films*, **290-291** (1996) 422-426.